08773

1.0

2.8 2.5

3.2

3.6 2.2

1.1 2.0

1.8

1.25 1.4 1.6

MICROCOPY RESOLUTION TEST CHART

LEVEL

REPORT ONR-CR213-162-1F

OFFICE OF

USN ONR

NAVAL RESEARCH

STABILITY AND CONTROL ANALYSIS
OF V/STOL TYPE B AIRCRAFT

Paul W. Berry
John R. Broussard
Sol Gully

THE ANALYTIC SCIENCES CORPORATION
Six Jacob Way
Reading, Massachusetts 01867

PREPARED FOR THE

OFFICE OF NAVAL RESEARCH ■ 800 N. QUINCY ST. ■ ARLINGTON ■ VA ■ 22217

80 8 6 015

CHANGE OF ADDRESS

Organizations receiving reports on the initial distri-
bution list should confirm correct address. This
list is located at the end of the report. Any change
of address or distribution should be conveyed to the
Office of Naval Research, Code 211, Arlington, VA
22217.

DISPOSITION

When this report is no longer needed, it may be trans-
mitted to other organizations. Do not return it to
the originator or the monitoring office.

DISCLAIMER

The findings and conclusions contained in this report
are not to be construed as an official Department of
Defense or Military Department position unless so
designated by other official documents.

REPRODUCTION

Reproduction in whole or in part is permitted for
any purpose of the United States Government.

UNCLASSIFIED

(19) REPORT DOCUMENTATION PAGE		READ INSTRUCTIONS BEFORE COMPLETING FORM
1. REPORT NUMBER (18) ONR-CR213-162-1F	2. GOVT ACCESSION NO. AD-A087 734	3. RECIPIENT'S CATALOG NUMBER
4. TITLE (and Subtitle) Stability and Control Analysis of V/STOL Type B Aircraft.		5. TYPE OF REPORT & PERIOD COVERED Technical 1 Oct 77 – 30 Sep 78
		6. PERFORMING ORG. REPORT NUMBER TR-1259-1
7. AUTHOR(s) John R. Broussard, Paul W. Berry, and Sol W. Gully		8. CONTRACT OR GRANT NUMBER(s) N00014-77-C-0775
9. PERFORMING ORGANIZATION NAME AND ADDRESS The Analytic Sciences Corporation Six Jacob Way Reading, Massachusetts 01867		10. PROGRAM ELEMENT, PROJECT, TASK AREA & WORK UNIT NUMBERS
11. CONTROLLING OFFICE NAME AND ADDRESS Office of Naval Research Technology Projects Division, Code 211 Arlington, Virginia 22217		12. REPORT DATE 31 March 1979
		13. NUMBER OF PAGES 184
14. MONITORING AGENCY NAME & ADDRESS(if different from Controlling Office)		15. SECURITY CLASS. (of this report) Unclassified
		15a. DECLASSIFICATION DOWNGRADING SCHEDULE

16. DISTRIBUTION STATEMENT (of this Report)

Approved for public release; distribution unlimited.

17. DISTRIBUTION STATEMENT (of the abstract entered in Block 20, if different from Report)

18. SUPPLEMENTARY NOTES

19. KEY WORDS (Continue on reverse side if necessary and identify by block number)

Aircraft Stability and Control, Atmospheric Flight Mechanics, Modern Control Theory, Vertical Takeoff Aircraft, Short Takeoff Aircraft, Thrust Vector Control, Digital Flight Control Systems, Feedforward Control Theory, Proportional Integral Control.

20. ABSTRACT (Continue on reverse side if necessary and identify by block number)

This report applies the tools of modern multivariable control systems analysis to an aircraft representative of a Type B V/STOL aircraft. Specifically, the AV-8A Harrier is analyzed in the low-speed, transition and hover flight regimes. New techniques for digital command augmentation system design, especially suited to precise control of a V/STOL aircraft,

DD FORM 1473 EDITION OF 1 NOV 65 IS OBSOLETE

UNCLASSIFIED

29. ABSTRACT (Continued)

are developed and applied at representative flight conditions.
The stability results indicate that a prime determinant of
longitudinal stability in the transition and nozzle-borne
flight regimes is nozzle angle; this result has an effect on
the choice of trajectories to minimize aircraft stability
problems. The lateral-directional stability is primarily a
function of forward speed and angle of attack, with the worst
case being high angle of attack, low-speed flight. To some
extent, flight conditions which minimize lateral-directional
stability problems accentuate longitudinal difficulties. A
second major section of this report develops the theory of
command-generator tracking (CGT), a very powerful control
system design method. Since the CGT allows independent solu-
tions to the stability augmentation and command augmentation
problems, the designer is free to employ the most efficient
techniques of solution to these two problems. The application
of CGT design techniques to various V/STOL flight condition
regimes includes the investigation of different vehicle com-
mand inputs. For air combat maneuvers, a normal acceleration-
roll rate command input is desirable, while a velocity command
vector is investigated in transition and thrust-borne flight.
Near hover, a position-command (4-D) system is appropriate, and
an attitude-command system is compared to the above systems.
Not only do these examples illustrate the flexibility of the
CGT design approach, each controller provides insights into
the stability and control characteristics of a V/STOL Type B
aircraft.

PREFACE

Accession For

NTIS GRA&I
DDC TAB
Unannounced
Justification

By
Distribution/
Availability Codes
Avail and/or
Dist   Special

A

iii

TABLE OF CONTENTS

LIST OF FIGURES

LIST OF FIGURES (Continued)

LIST OF FIGURES (Continued)

LIST OF TABLES

1.   INTRODUCTION

1.1   BACKGROUND

Future missions of the U.S. Navy will involve increased use of vertical/short-takeoff-and-landing (V/STOL) aircraft in a variety of roles. It is important that these new aircraft be designed for maximum performance, reliability, and safety. High-performance V/STOL aircraft, such as the V/STOL B concept now receiving study, have special problems; they must not only hover and transition to forward flight, but fly in the air combat environment as well. Thus, the relatively efficient and well-understood mechanisms currently used to produce lift at hover (low-disc-loading rotors) can not be used in V/STOL B aircraft, as they are inappropriate for flight at high Mach number. Instead, the V/STOL B aircraft is likely to rely on high-momentum jet thrust for hover. This introduces the probability of severe stability and control problems in low-speed flight, including "suck-down" and "fountain-flow" phenomenon in ground effect.

The need to provide lift via jet thrust in hover introduces the possibility of a "fringe benefit" in high-speed flight; vectored thrust can be used to enhance maneuverability in air combat. Flight tests and simulation of the AV-8A Harrier indicate that inflight thrust vectoring can provide substantial gains for air-to-air combat and also may be effective for air-to-ground weapon delivery (Refs. 1 and 2). The advantages accrue not only because the thrust vector can be redirected, but also because the high-performance V/STOL aircraft has reaction control effectors for hovering control;

1

therefore, the aircraft retains angular controllability throughout its flight envelope.

Command and stability augmentation take on added significance for the V/STOL B aircraft, for it is truly a control-configured vehicle (CCV). <u>Without command/stability augmentation, the V/STOL B aircraft will almost certainly have unacceptable handling qualities at one or more flight conditions, and it is likely that maneuvering will compound these difficulties (Ref. 3).</u>

Recognizing the need for applying the most modern techniques to V/STOL B stability-and-control analysis, this study extends the high-angle-of-attack techniques developed under prior ONR contracts (Refs. 4 and 5) to the V/STOL problem, using the AV-8A Harrier aircraft (Fig. 1) as a basis for study. These methods use modern control theory and state-space
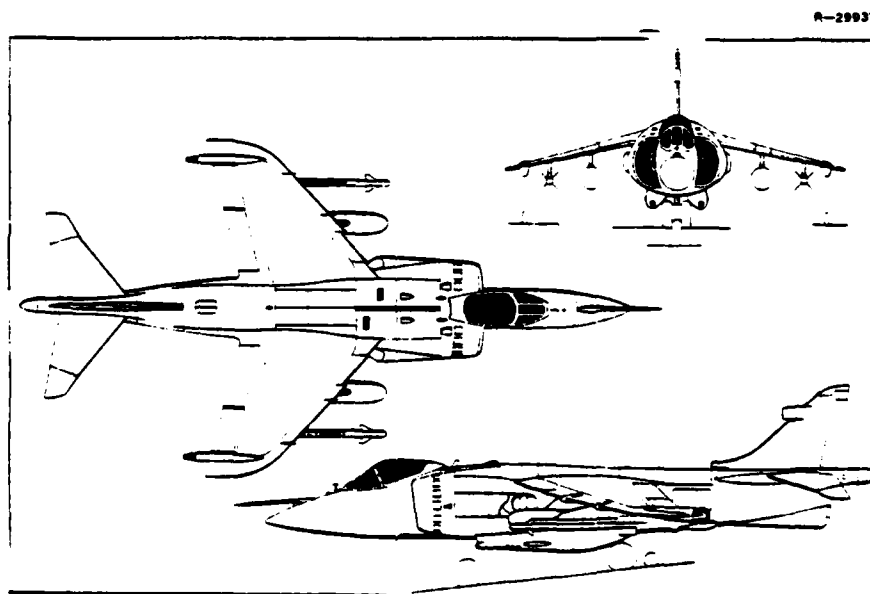
Figure 1   AV-8A Harrier: Baseline Aircraft for
            Stability-and-Control Investigation

analysis, both of which are well-suited to the complex nature of V/STOL flight, and they have been carried to a high level of refinement in our earlier work. The AV-8A is chosen as a baseline aircraft because representative data for that aircraft is readily available (Ref. 6). The word "representative" should be emphasized; our proposed goal is a better understanding of generic V/STOL B stability-and-control characteristics rather than a detailed study of a particular aircraft.

1.2   REPORT OUTLINE

This report is organized according to the following outline: Chapter 2 addresses the open-loop stability of the AV-8A's linear, time-invariant model representation and the trim conditions that occur in flight. Chapter 3 presents the design and simulation results for the command generator tracker-proportional integral (CGT-PI) controller. Conclusions and recommendations are presented in Chapter 4. Feedforward CGT theory is developed in Appendix A. Pilot command models and the eigenvalue/eigenvector based "ideal" aircraft model are shown in Appendix B. The form of the reference aircraft mathematical model is listed in Appendix C. A list of symbols and abbreviations is given in Appendix D.

2. STABILITY AND CONTROL ANALYSIS IN LOW-SPEED, TRANSITION, AND CONVENTIONAL FLIGHT

2.1 OVERVIEW

The extensive range of flight conditions of the AV-8A Harrier presents a challenge to the aircraft control system designer and to the aircraft pilot. At low speed, thrust and gravity forces are paramount, and the vehicle dynamically resembles an inverted pendulum. Aerodynamic forces become important through the transition, accompanied by drastic changes in the flow field around the aircraft as the nozzles are swiveled backwards. At the same time, the control system transitions from reaction control jets to conventional aerodynamic control surfaces. Appendix C contains a complete description of the data used to model the AV-8A, and an analysis of its control system. Note that all results presented in this chapter are for the "bare airframe" (i.e., with the stability augmentation system switched off).

Section 2 of this chapter examines the complete range of flight conditions from low-speed through transition to conventional flight, and details the effect of these velocity changes on vehicle stability. The implications of these changes on vehicle lateral control are also discussed, as are the changes in vehicle stability due to ground effect. Section 3 details the manner in which variations in angle of attack and longitudinal acceleration affect vehicle stability at an intermediate velocity, while Section 4 discusses the vehicle stability characteristics to be expected during a ski-jump launch. Section 5 summarizes the results of this

4

chapter, and presents figures which give the relationship between the most important variables and their effect on AV-8A stability.

2.2 FLIGHT CONDITIONS AND VELOCITY-DEPENDENT STABILITY EFFECTS IN THE TERMINAL AREA

2.2.1 Trim Flight Conditions

The flight conditions examined in this section span the range of velocities from 190 kt (98 m/s) to 10 kt (5 m/s); included are conventional wing-borne flight conditions, transition flight conditions and low-speed thrust-borne flight conditions. Figure 2 illustrates the angles of attack (α) involved in these flight conditions. For conventional flight ($\theta_j=0$, i.e., nozzles fully aft), α increases with decreasing speed.
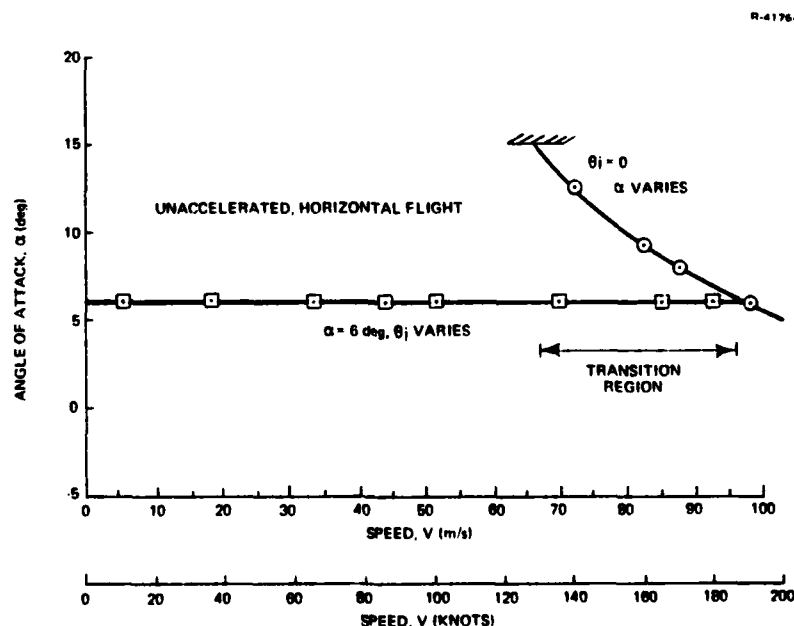
Figure 2   Angle of Attack

5

If 15 deg α is the upper limit, then 128 kt (66 m/s) is the
lower speed limit in conventional flight for this vehicle
weight. (High-lift devices are not modeled.) The Harrier can
fly at angles of attack below the conventional curve by lower-
ing the nozzles to make up for lost wing lift. If a constant
α of 6 deg is assumed, this trade-off can be effected at any
speed below 190 kt (98 m/s). Figure 3 presents this in terms
of the portions of vehicle weight supported by aerodynamic
lift and propulsive lift. The thrust-produced vertical com-
ponent of the supporting force is directly proportional to
throttle and nozzle deflection angle. In general, the thrust
force also includes ram drag forces, although these do not
contribute to the vertical component of thrust force in hori-
zontal flight. The wing-borne lift is proportional to dynamic
pressure, and takes into account the lift decrement caused by
the thrust-induced flow field changes. Figure 3 also shows
zero nozzle-angle curves; conceptually there are a series of
curves with varying wing-borne/thrust-borne ratios in the
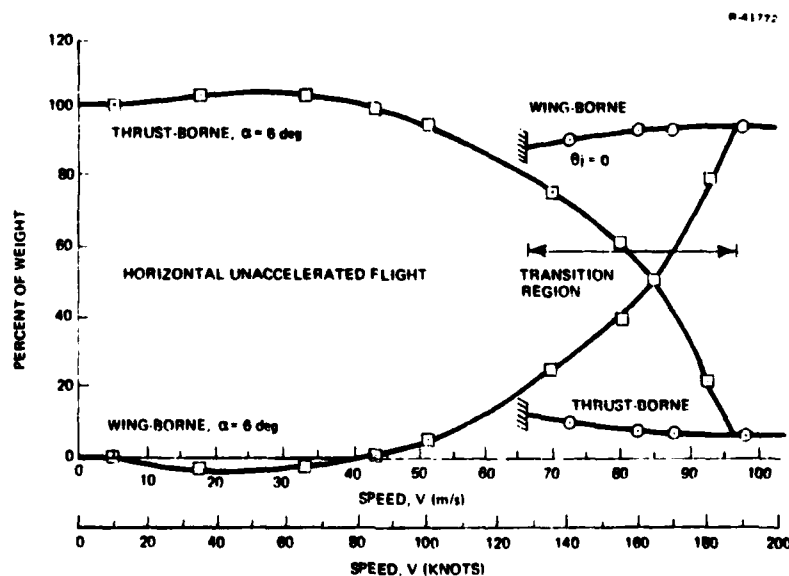
Figure 3   Wing Lift/Thrust Lift Trade-Off

6

transition speed regime. These curves represent different combinations of α and θ_j.

The variation in nozzle angle with velocity at the nominal angle of attack is shown in Fig. 4. This follows the general shape of the thrust-borne-weight curve in the previous figure. At low speeds, the thrust vector angle with respect to vertical, which is the sum of the nozzle angle relative to its datum (θ_j), the nozzle datum relative to the body (1.5 deg) and the body pitch angle (θ), approaches 90 degrees.

The engine speed (and hence thrust) necessary to trim at these flight conditions is given in Fig. 5. The steady-state relationship typical of thrust-borne flight (increased engine speed is necessary at lower flight speeds) is apparent in this figure. The engine speeds needed for fully wing-borne flight are also given in the higher flight speed range, and the difference is indicative of the relative efficiency of wing-borne flight.
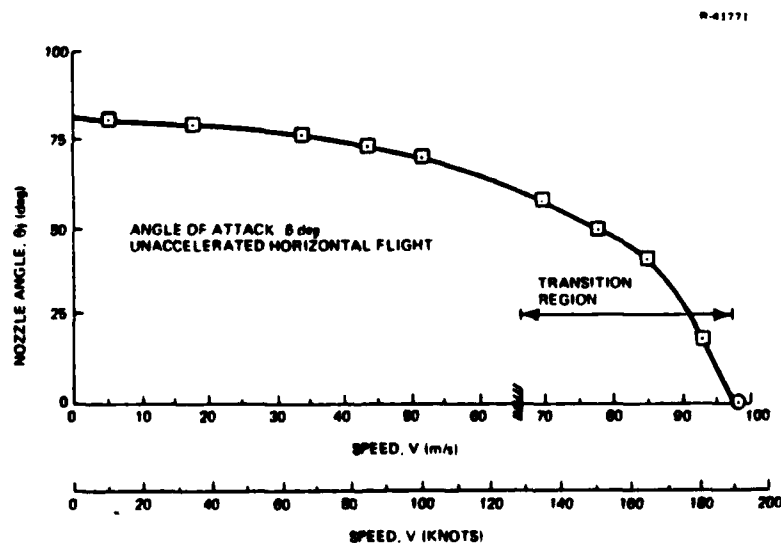
Figure 4   Nozzle Angle Versus Velocity
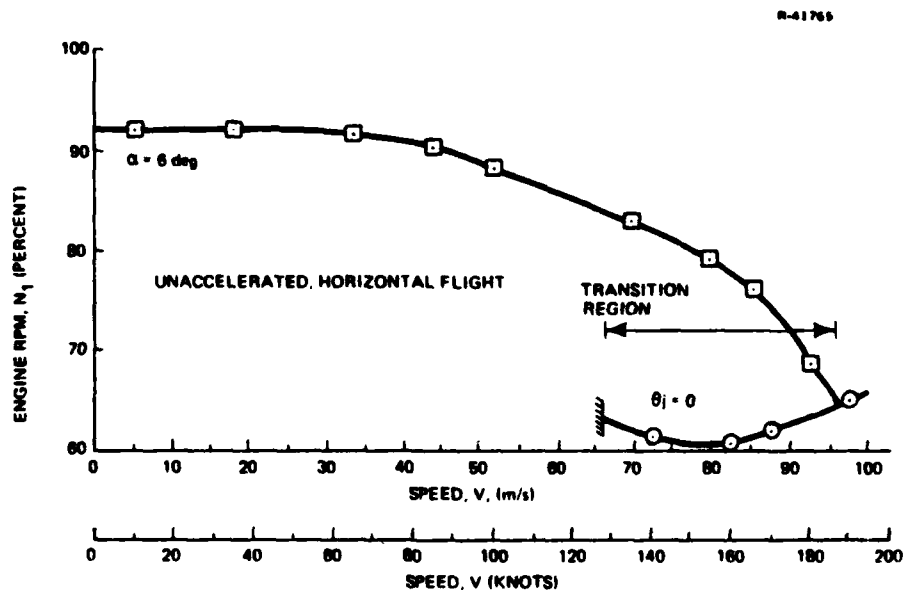
Figure 5   Engine RPM at Various Speeds

The stabilator deflections in the velocity range from
10 kt (5 m/s) to 190 kt (98 m/s) are given in Fig. 6, illus-
trating the mild changes in pitch trim that occur between the
various velocities with nozzles down. Also of note is the
large change in stabilator position between the "nozzles up"
position and the "thrust borne" flight condition. The aero
data tables show that this shift is due to the large change in
stabilator deflection for zero pitch moment caused by the flow
field changes as the nozzles are lowered. For example, at 5
deg angle of attack, zero aerodynamic pitch moment coefficient
occurs at -6.95 deg stabilator and zero nozzle angle, but at
45 deg nozzle angle, zero aerodynamic pitch moment coefficient
occurs at 6.05 deg stabilator. This indicates that as the
nozzles are dropped to 45 deg a significant nose up pitch
moment will arise. This requires the pilot's attention in
order to transition smoothly from wing-borne to nozzle-borne
flight.

R-41770
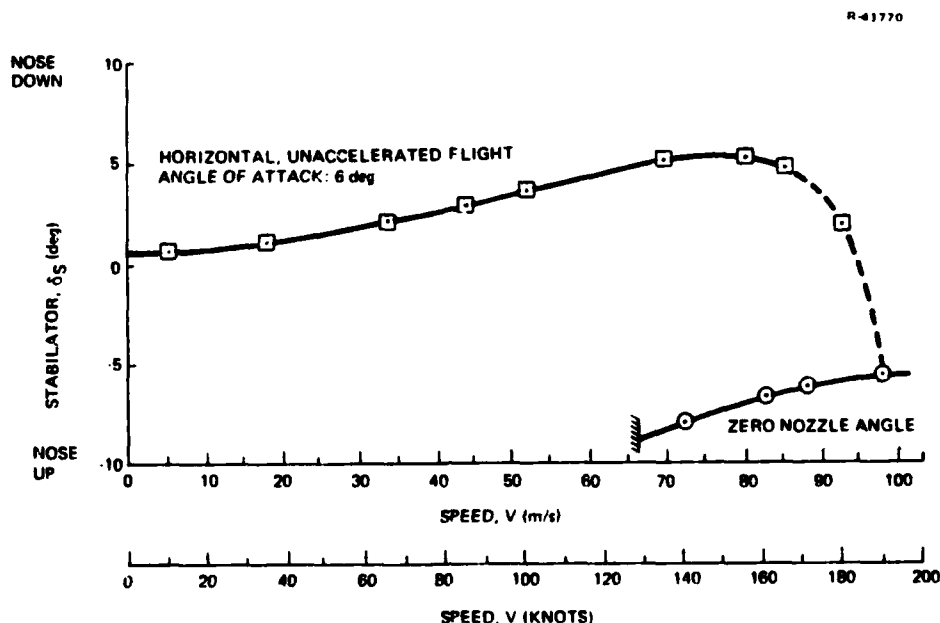
Figure 6   Stabilator Deflection Versus Velocity

The pitch jets (which thrust downwards from either the nose or tail of the aircraft) also are important, and Fig. 7 details the operation of these jets. For purposes of trim calculation, the jets are connected to the stabilator in the same manner as in the actual aircraft for the sas-off case. The only exception is for nozzle angle less than 20 deg, where the trim results presented here assume that the pitch jets are completely off. In actuality, they are phased in as the nozzles transition from zero to twenty degrees. For this reason, the trim control results in this region are represented by dashed lines.

The range of flight conditions described here is examined in the following section as to the vehicle stability and control characteristics.

R-41769
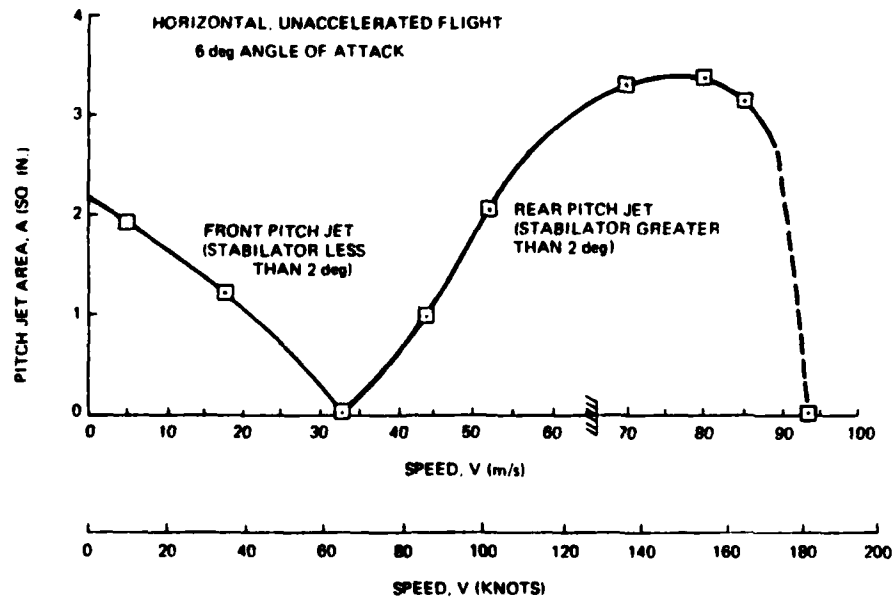
Figure 7   Pitch Jet Opening Versus Velocity

2.2.2 Velocity-Dependent Stability Variations

The variations in longitudinal and lateral-directional
stability over the range of flight conditions from 10 to 190
kt (5 to 98 m/s) are discussed in this section. All trim
conditions represent symmetric flight; hence, the longitudinal
linear dynamics are uncoupled from the lateral-directional
linear dynamics. For nozzles completely rearward (θ_j=0 deg),
Fig. 8 shows that the longitudinal modes consist of a fast,
well-dampled short period mode and a slow, poorly-damped
phugoid mode. Both of these are typical of conventional
aircraft.

For nozzles downwards, the longitudinal modes are
completely different. At very low speed (10 kt, 5 m/s),
the four longitudinal eigenvalues consist of an unstable

10

LONGITUDINAL MODES FROM HOVER
TO 190 KT (98 m/s) (ALL SPEEDS IN KT)

IMAGINARY PART, $j\omega$ (sec^{-1})

140

190 — SHORT PERIOD ($\theta_i = 0$)

PHUGOID ($\theta_i = 0$ deg)

180 — SHORT PERIOD ($\alpha = 6$ deg)

THIRD MODE ($\alpha = 6$ deg)

REAL PART, σ (sec^{-1})

140 / 190 — 155

STABLE ANGLE OF ATTACK MODE

STABLE PITCH-SPEED MODE ($\alpha = 6$ deg)

165 ($\alpha = 6$ deg) — 10 — 100 10

180 — 165

160

SPEED-AOA MODE ($\alpha = 6$ deg) — 160

SPEED DIVERGENCE ($\alpha = 6$ deg)
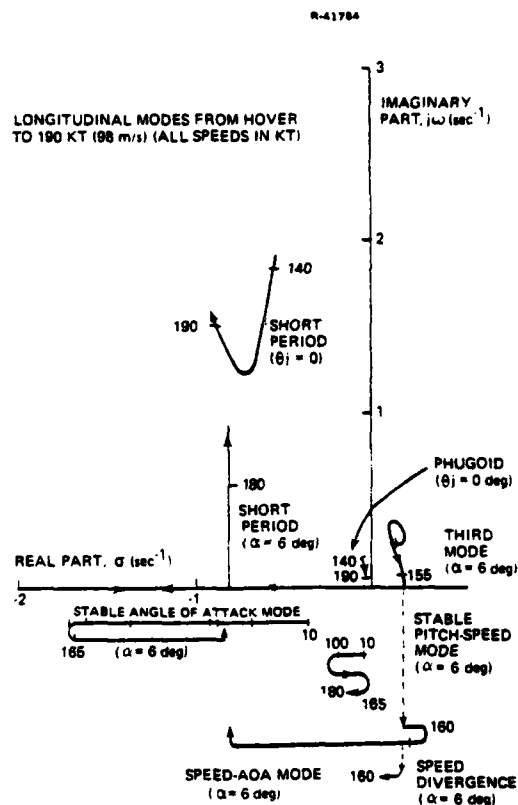
Figure 8   Longitudinal Modes from Hover to 190 kt

oscillatory pair, the <u>third mode</u> (so-called because it is
inherently different from the short-period and phugoid os-
cillations), and two stable real roots. The slow real root
exhibits primarily pitch-speed characteristics, while the
faster one involves angle of attack variation. This mode
becomes much faster as the aerodynamic forces grow with in-
creasing speed.

The unstable third mode is caused by a static pitch
instability in much the same way as a cg too far aft can
cause difficulty for a conventional aircraft. The problem
with this aircraft is caused by both aerodynamic and engine

11

effects. The aerodynamic pitch moment due to angle of attack $(C_{m\alpha})$ is small at low speeds and depends on nozzle angle so that stabilizing aerodynamic moments are not really provided until the nozzle angle is reduced below 30 deg. The engine further destabilizes the longitudinal dynamics because of the ram drag effect. This is a drag force caused by the engine inlet air flow, and it depends on airspeed and engine rpm. Because this drag force is applied ahead of the cg, it produces a nose-up moment which grows with increasing angle of attack. The net effect of the aerodynamic and engine-induced effects is that the vehicle is statically unstable below about 170 kt (87 m/s).

The shapes of these modes are shown in Fig. 9 for both 135 kt (69 m/s) and 180 kt (93 m/s). At 135 kt (69 m/s), the unstable third mode will cause difficulty. As can be seen, this mode is much different from a conventional short period mode. The amount of velocity and pitch angle variation is much larger, and the phasing between pitch rate and angle of attack (essentially the same as body z-axis velocity) is much different. At 180 kt (93 m/s), the aircraft is statically stable, as evidenced by the presence of a conventional short period mode. The short period is formed from the angle of attack convergence and a root resulting from the decomposition of the third mode at about 158 kt (31 m/s). This decomposition also produces a very slow speed divergence mode, and the stable pitch-speed mode remains much the same.

The lateral modes of motion, shown in Fig. 10, display conventional Dutch roll, roll and spiral modes for nozzles fully aft ($\theta_j=0$), with a poorly damped Dutch roll mode worthy of note. Near hover (10 kt, 5 m/s), the aircraft exhibits two slow oscillations, one stable and one unstable. The Dutch roll mode, which is unstable until about 120 kt (62 m/s),

Figure 9   Longitudinal Modes at 135 kt (69 m/s)
            and 180 kt (93 m/s)
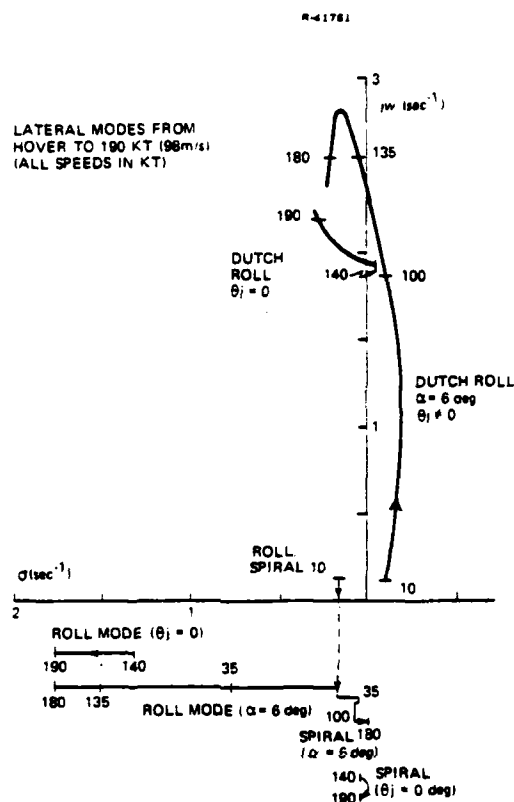
Figure 10   Lateral Modes from Hover to 190 kt (98 m/s)

increases in frequency with increasing V while only slight
forward speed increase (to 35 kt, 18 m/s) splits the roll/
spiral oscillation into conventional roll and spiral modes.
In the transition speed range, only relatively small changes
in mode speed occur as the transition from wing-borne to
nozzle-borne flight is made. There are some significant
changes in mode shape, however, as evidenced by Fig. 11. The
lateral mode shapes at 160 kt for both nozzle-borne flight
(θ_j=45.2 deg) and wing-borne flight (θ_j=0.0 deg) are shown.
The value of $C_{n\beta}$ (yaw moment derivative with respect to side-
slip) is about half as large at this wing-borne flight condi-
tion than for the thrust-borne case; hence, the lateral modes
are slower and exhibit significantly larger amounts of sideslip
relative to the angular rates. In general, the transition

14

LATERAL MODE SHAPES AT 160 KT (82 m/s)

α= 6 deg, θj = 45.2 deg

DUTCH ROLL   ROLL   SPIRAL

Δr Δp Δv $\Delta \phi$

$-0.136 \pm j\ 2.823$ -1.684 -0.019

α= 9.12 deg, θj = 0 deg

DUTCH ROLL

Δp $\Delta \phi$ Δv Δr

$-0.110\ \ j\ 1.996$ -1.458 0.0125
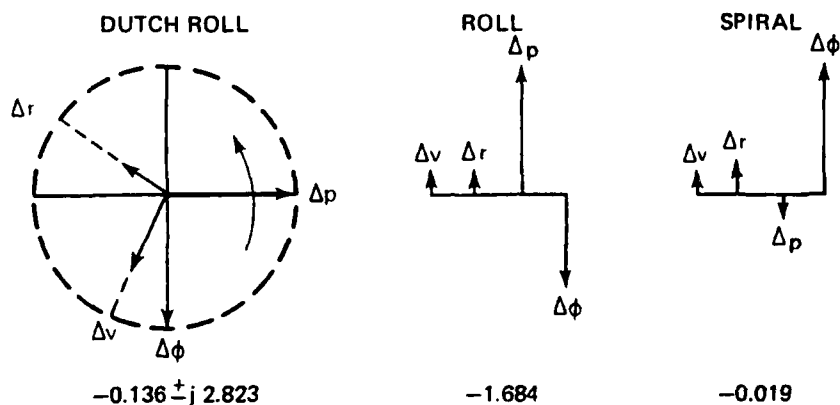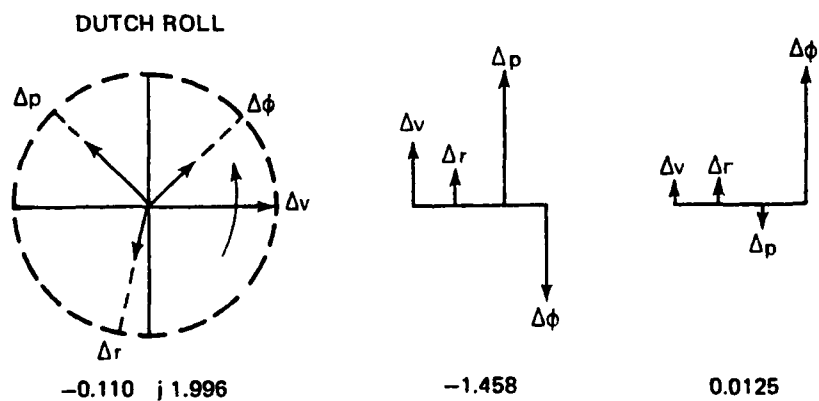
Figure 11   Lateral Mode Shapes at 160 kt (82 m/s),
α=6 deg, θ_j=45.2 deg

regime lateral modes are similar to those of a conventional
aircraft, and hence should not present a major piloting problem.

15

2.2.3 Sideslip Stability Boundaries

The Harrier exhibits large positive dihedral effect in the transition flight regime (Ref. 8), and this results in a limit to allowable sideslip excursions. This occurs because the roll moment induced by sideslip ($L_\beta \cdot \Delta\beta$) can be larger than the available roll control power ($L_{\delta rj} \cdot \delta_{rj} + L_{\delta a} \cdot \delta_a$). Little difficulty is exhibitied at low velocities because the aerodynamic roll moment is small, and no difficulty occurs in conventional flight because the dihedral effect is smaller in wing-borne flight and the ailerons are more effective. For example, Table 1 gives values for L_β in both wing-borne and thrust-borne flight. Hence, the region of concern is the transition region. This region is examined here by the use of the static roll moment equation

$$I_x \dot{p} = 0 = L_\beta \Delta\beta + L_{\delta rj}\delta_{rj} + L_{\delta a}\delta_a \tag{1}$$

The amount sideslip that can be balanced by a given amount of control can be calculated by Eq. 2

$$\Delta\beta = -\frac{L_{\delta rj}}{L_\beta}\delta_{rj} - \frac{L_{\delta a}}{L_\beta}\delta_a \tag{2}$$

TABLE 1

DIHEDRAL EFFECT AT 160 kt (82 m/s)

FLIGHT CONDITION	EFFECTIVE DIHEDRAL, L_β
Wing-Borne $\alpha=9.12$ deg $\theta_j=0.0$ deg	-461 lb$_f$-ft/deg, -625 N·m/deg
Thrust-Borne $\alpha=6$ deg $\theta_j=45.2$ deg	-1560 lb$_f$-ft/deg, -2115 N·m/deg

Hence, the maximum allowable sideslip can be calculated from
Eq. 2 by inserting the maximum control deflection in the
equation. Figure 12 shows the results of this calculation for
the roll reaction jets and the aileron separately, and for
their sum. These calculations are performed at 6 deg α; the
roll control deficiency is larger at higher angles of attack.
For example at 100 kt (51 m/s), the maximum sideslip is re-
duced 2 deg, or 13%, by increasing the angle of attack to 12
deg. Also shown in Fig. 12 is the sideslip demonstration
envelope required by Section 3.3.11 of Ref. 15. The area
between the demonstration envelope and the sideslip limited by
total roll control application is a region where an uncon-
trollable roll is predicted by this linear analysis. A further
comment is prompted by Section 3.3.11.3.1 of Ref. 15 which re-
quires that for Level 1 handling qualities no more than 50% of
the available roll control power be used to counter "sideslip
angles which might be experienced in service employment".
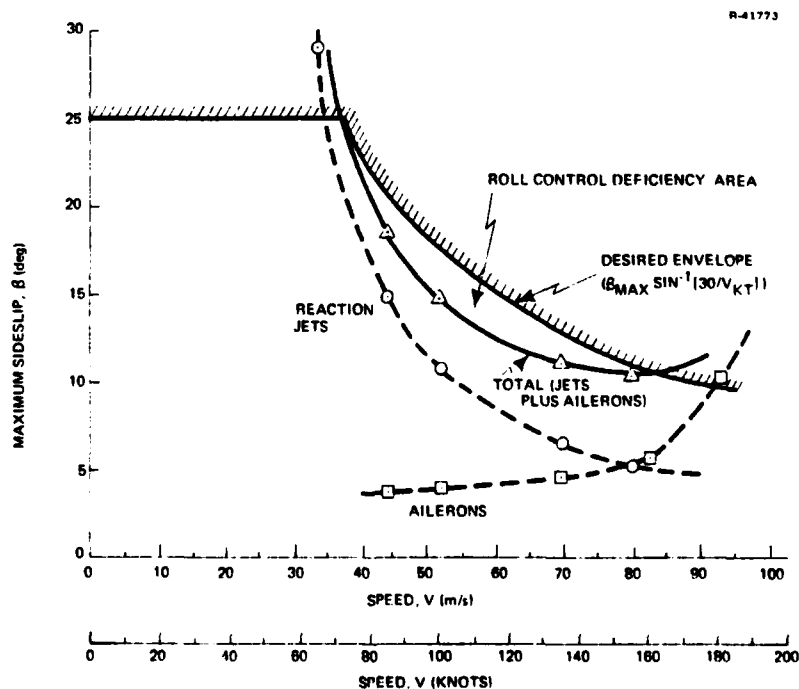
Figure 12   Sideslip Boundary Due to Roll Control Limit

17

This restriction would greatly expand the speed range where the maximum controllable sideslip fell below the flight test demonstration limit.

This problem is one that has been recognized previously, as stated in Ref. 8, and is being corrected in the YAV-8B Harrier by increasing the roll reaction jet effectiveness. The YAV-8B control system, described in Ref. 16, includes larger roll reaction jet thrust and a longer moment arm, as shown in Table 2. Also given is the total roll moment due to full reaction jet thrust. As can be seen, this value is 72% larger for the YAV-8B.

TABLE 2

ROLL REACTION JET PARAMETERS-AV-8A VS YAV-8B

	AV-8A	YAV-8B
Roll Jet "Up" Thrust	612. lb_f, 2722 N	750. lb_f, 3336 N
Roll Jet "Down" Thrust	237.5 lb_f, 1056 N	350. lb_f, 1557 N
Jet Moment Arm	11.08 ft, 3.377 m	14.75 ft, 4.496 m
Total Roll Moment	9412.5 lb_f-ft, 12760. N·m	16225. lb_f-ft, 22000. N·m

Applying a factor of 1.72 to the reaction jet curve in Fig. 12 results in an approximation to the sideslip boundary expected of the YAV-8B. These results are shown in Fig. 13. The sideslip boundary for maximum deflection of both reaction jets and ailerons is well outside the desired demonstration boundary. At 50 percent total control power, the maximum allowable sideslip boundary, although lower than the demonstration boundary from 67 kt (34 m/s) to about 190 kt (98 m/s) may correspond to sideslip angles which might be expected in service employment. It should be noted that 50% aileron deflection does not occur at 50% reaction jet thrust in the
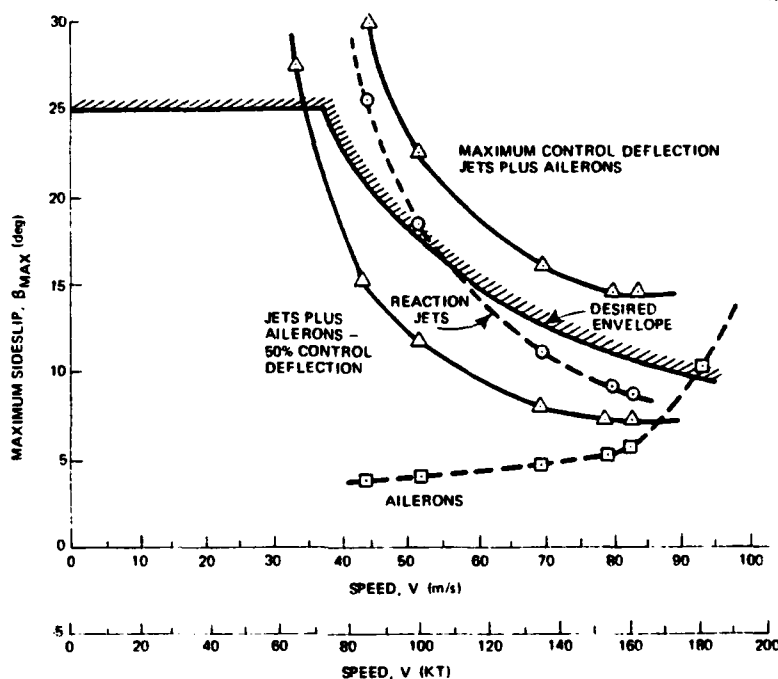
Figure 13   Approximate YAV-8B Sideslip Boundary

YAV-8B, but rather at about 63% raction jet thrust. This is
due to the reaction jet gearing, which results in full roll
reaction jet thrust at 80% lateral stick travel, rather than
100% as in the AV-8A. (See Appendix C.) Hence, the roll
control derivative (for less than 80% lateral stick) is about
2.15 times larger in the YAV-8B than in the AV-8A.

This analysis indicates that the AV-8B should be able
to demonstrate the entire range of sideslip desired by Ref. 15,
and may satisfy Level 1 restrictions on positive effective
dihedral.

2.2.4 Influences of Ground Effect on Stability

The model for ground effect that is used here, taken
from Ref. 17, is described in Appendix C. Vertical force,

pitch moment and roll moment are all affected as the aircraft descends from above 20 feet (3.1 m) to ground level. Figure 14 shows the aircraft mode shapes and speeds both out of ground effect (OGE) and in ground effect (IGE). As shown in Section 2.2.2, there is an unstable longitudinal third mode as well as an unstable Dutch roll mode at 10 kt (5 m/s) OGE. The modes exhibit periods of 25 and 80 sec respectively. The same flight speed in ground effect results in drastically different modes. The pitch effects stabilize the longitudinal oscillation, which takes on some aspects of a short period response, especially in the pitch rate-angle of attack phasing. The thrust loss due to ground effect results in the destabilization of the neutrally stable (zero-valued eigenvalue) altitude mode, and the altitude instability exhibits a time constant of 3.5 sec, which corresponds to a time-to-double of 2.4 sec. Relatively little pitching (0.03 deg pitch up per foot of lost altitude) and speed change (-0.05 fps per foot of lost altitude) occur as the aircraft drops. The rapid divergence of this mode and the difficulty of quickly and accurately controlling thrust suggest that steady flight in ground effect should not be attempted, and that ground effect altitudes should only be entered with the intention of landing.

The changes in lateral-directional mode shape and speed that occur due to ground effects are also very severe. The large destabilizing roll moment effect splits up both OGE lateral oscillations. Two slow yaw and sideslip modes are formed (one stable and one unstable) and two very fast roll modes appear. One is very stable (time-to-half-amplitude is 0.28 sec) while the other is equally unstable (time-to-double-amplitude is 0.29 sec). This very fast instability causes greatly increased pilot lateral control activity at low altitudes, as shown in Ref. 7, for example.

20

Figure 14   Aircraft Mode Changes Due to Ground Effect

21

The linear model of the V/STOL aircraft displays characteristics in ground effect which agree with the observed responses of the aircraft and provide information about the aircraft instabilities in ground effect. An examination of the effect of ground effect instabilities on control system design is described in Chapter 3.

2.3 STABILITY VARIATIONS DUE TO ANGLE OF ATTACK AND CHANGING VELOCITY

2.3.1 Accelerated Flight Conditions at Various Angles of Attack

An airspeed of 100 kt (51.4 m/s) is chosen for the examination of AV-8A stability variations with α and accleration along the flight path (hereafter referred to as the derivative of velocity - $\dot{V}$). At this airspeed, trim flight conditions are found at angles of attack from 0 to 16 deg. At lower α, the lack of wing lift must be made up by vertically-oriented thrust force, hence a nozzle angle to angle of attack relationship results as shown in Fig. 15. Quasi-static trim flight conditions (conditions where the aircraft is trimmed about a steady $\dot{V}$) are also shown in the figure. As can be seen, the nozzles are deflected rearward to accelerate and forward to decelerate. The general reduction in nozzle angle at higher angles of attack is due primarily to the increased body pitch angle. The actual nozzle angle with respect to the vertical changes only slightly as angle of attack is varied.

For a given α, increasing or decreasing velocity can be done essentially at constant engine throttle setting. Table 3 illustrates this observation. Indeed, at 16 deg α, these results indicate that slight increases in throttle

22
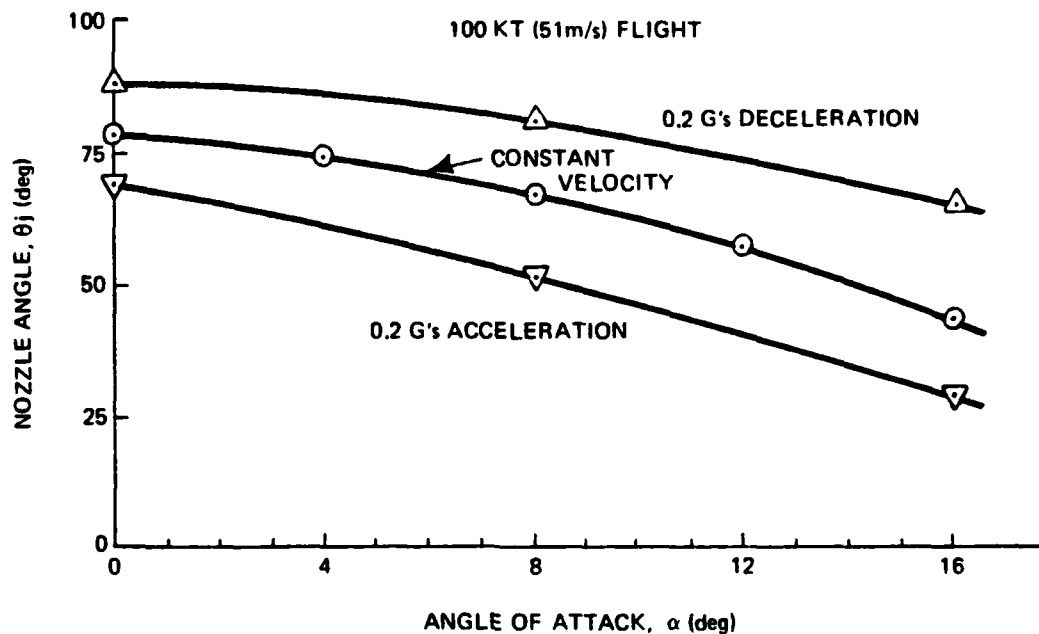
Figure 15   Nozzle Angle vs Angle of Attack

TABLE 3

TRIM ENGINE RPM (PERCENT) AS A FUNCTION OF
ANGLE OF ATTACK AND LONGITUDINAL ACCELERATION
(at 100 kt - 51 m/s)

ACCELERATION ANGLE OF ATTACK	-0.2 g's	0.0 g's	0.2 g's
0 deg	94.3	94.1	94.9
4 deg	-	90.6	-
8 deg	86.6	86.7	86.5
12 deg	-	81.0	-
16 deg	77.1	75.8	80.4

are necessary to achieve <u>either</u> a steady accleration or de-
celeration. Also noteworthy in Table 3 is the observation
that the high-α, high-drag flight conditions require less
throttle than lower drag angles of attack. This is due to the
increase in lift at higher α which reduces the amount of
thrust-borne weight.

The relationship between flight condition ($\dot{V}$, α, and
θ_j) and amount of wing-supported weight is shown in Fig. 16.
The increase in wing-supported weight with α is readily seen,
as is the resulting decrease in θ_j. (Since θ_j is measured
relative to the fuselage, most of this decrease is due to the
fuselage pitch increase.)
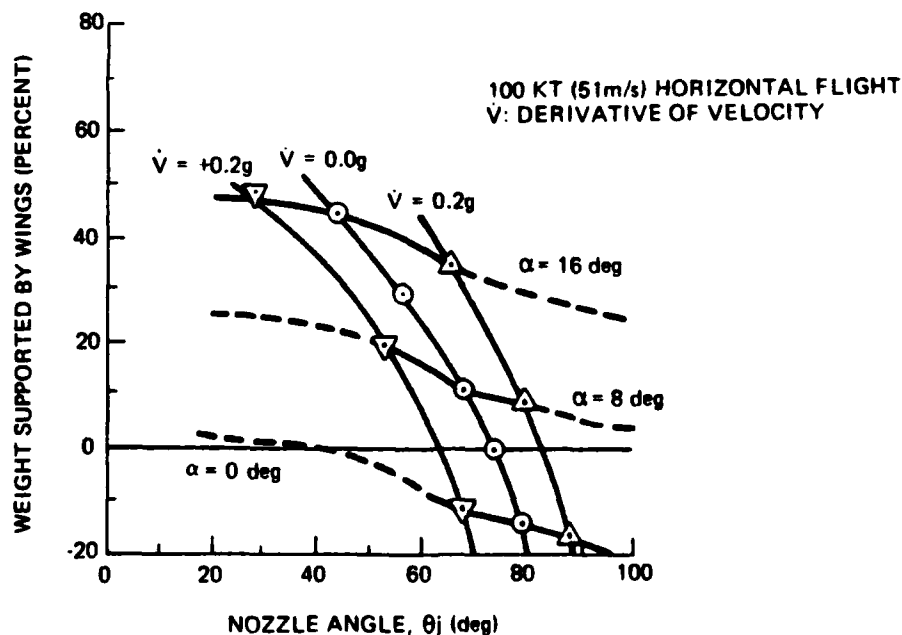
Figure 16   Wing Supported Weight Variation with Angle
              of Attack

Nozzle angle is an important variable in explaining
the variation in wing-supported lift due to acceleration along

the flight path, since the same curve seems to apply to all
angles of attack between 0 and 16 deg. Above about 65 deg
nozzle angle and below about 45 deg nozzle angle, moderate
increases in wing-supported weight accompany the reduction in
θ_j that cause the aircraft to accelerate. Between 65 and 45
deg nozzle angle, however, wing-supported weight rises drama-
tically a θ_j is reduced. This indicates a significant change
in the character of the flow field around the aircraft in this
region. These curves also explain the observation made con-
cerning Table 3: No additional thrust is needed to accelerate
because extra wing lift (at constant α) is available when the
nozzles are closer to their aft position. Efficiency of
flight (decreased thrust, increased wing lift) is increased by
an increase in α and a decrease in θ_j, especially in the 45 to
65 deg nozzle angle range.

2.3.2 Stability Variations with Angle of Attack

        The basic modes of motion of this vehicle include a
slow, unstable longitudinal oscillation--the third mode, and
two real longitudinal convergence modes, as well as Dutch
roll, roll and spiral modes. The loci of these modes as α
varies are shown in Fig. 17. The fast convergences, angle-of-
attack and roll modes, change somewhat with increasing trim α
while spiral retains its slow, stable character.

        Between 12 and 16 deg α, the longitudinal third mode
decomposes into two real roots. One is a fast, unstable di-
vergence in pitch and angle of attack, while the other almost
immediately combines with the slow pitch-speed mode to form a
conventional phugoid mode.

        Dutch roll mode is unstable throughout most of this
angle-of-attack range. The actual crossing of the imaginary

25
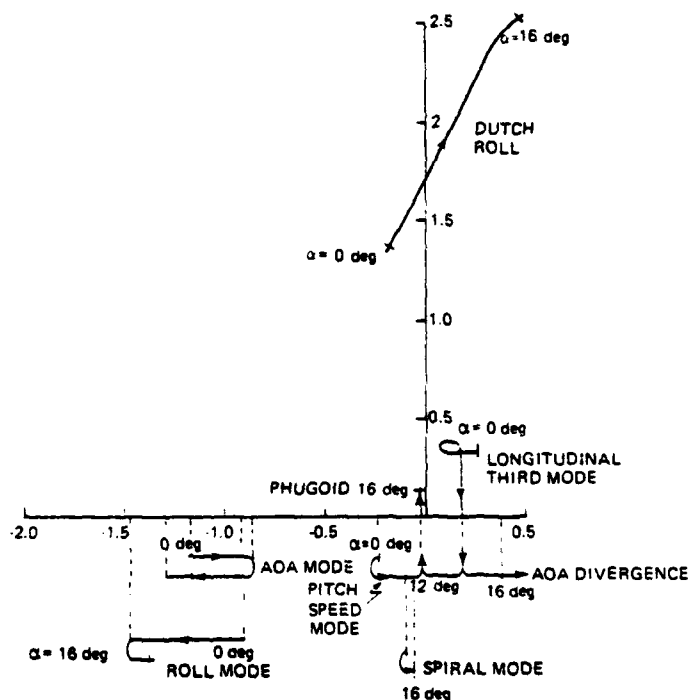
Figure 17   Variations in Aircraft Stability
               with Angle of Attack

axis occurs at about 4 deg α. Both frequency and speed of di-
vergence increase with α, making this mode the most trouble-
some to the pilot. At any angle of attack above 7 deg, the
Dutch roll amplitude doubles in less than 5 sec.

2.3.3 Stability Variations with Acceleration

Acceleration along the velocity vector ($\dot{V}$) is varied
from +0.2 g to -0.2 g and its effect on the stability of the
aircraft is described in this section. Figure 18 illustrates
these stability variations with acceleration at three different
angles of attack (0, 8, and 16 deg).
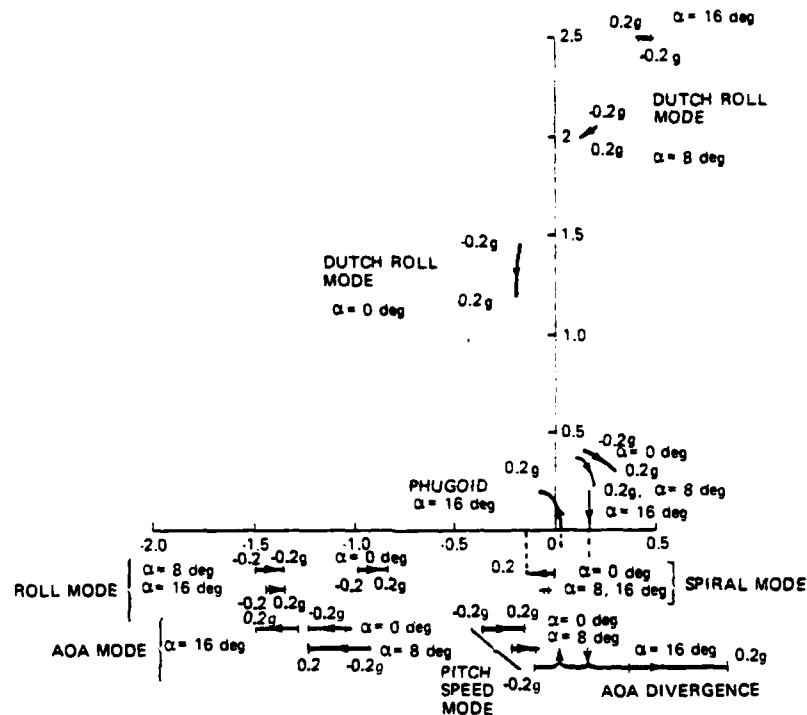
Figure 18   Stability Variations with Acceleration

Acceleration has an opposite effect on the two longitudinal real modes. The very stable angle-of-attack mode is made even more stable by acceleration, whereas the slow pitch-speed mode is made more stable by deceleration. A value of -0.2 g is sufficient to stabilize this mode even at 16 deg angle of attack. On the other hand, 0.2 g acceleration results in an interaction with the third mode which produces a conventional phugoid oscillation and a fast angle of attack divergence.

The unstable longitudinal third mode diverges faster under acceleration for 0 and 8 deg angle of attack. This is the opposite of the effect of acceleration on the pitch-speed

mode. At 16 deg angle of attack, it appears that any value of acceleration or deceleration will result in an instability. Deceleration causes an unstable third mode, with significant forward velocity oscillation, whereas during acceleration, a fast unstable angle-of-attack divergence appears. This change in appearance of the instability may cause control difficulties.

In the lateral-directional modes, the acceleration effect is much less. At higher angles of attack, acceleration has a minor stabilizing effect on the unstable Dutch roll mode, whereas the roll mode is slowed by acceleration. Except at low angles of attack, spiral is affected little by the different acceleration trim flight conditions. To summarize, acceleration has a secondary effect on the mode speeds relative to the primary determinant, angle of attack. The effect of acceleration varies from mode to mode, and often seems to take the form of damping interchange, where one mode is made more stable while another is made less stable.

2.4 STABILITY DURING A SKI-JUMP LAUNCH

2.4.1 Range of Flight Conditions Examined

The ski-jump launch of a fixed-wing V/STOL aircraft is characterized by an upward flight path angle (γ = 10 to 20 deg) and a downward flight path angular rate (i.e., the trajectory is semi-ballistic). The performance advantage lies in the lower launch airspeeds or higher launch gross weights that are achievable (Ref. 9). It is the goal of this section to examine the stability of flight conditions typical of ski-jump launches.

The airspeed at the end of the ski-jump is taken as 65 kt (33 m/s), which is in the lower range of useable values (Ref. 9 lists 65 to 80 kt - 33 to 41 m/s - airspeeds as likely). At this speed, little wing lift is gained by high α, so a basic angle of attack of 6 deg is chosen. Horizontal flight is examined first. Figure 19 details the engine throttle setting required to trim the aircraft for various values of $\dot{V}$ from 0.0 to 0.6 g, and for various values of normal acceleration. For this velocity, a flight path rate ($\dot{\gamma}$) of 5 deg/sec implies a 1.3 g pull up, zero $\dot{\gamma}$ is 1 g flight, while -5 deg/sec $\dot{\gamma}$ gives a 0.7 g normal specific force (i.e., -0.3 g downward acceleration). The important aspect of this plot is that vertical specific force can be traded for acceleration along the flight path ($\dot{V}$) with no change in throttle setting. For example, a 0.3 g decrease in vertical specific force allows a 0.68 g increase in acceleration along the flight path with no increase in throttle setting. After the Harrier leaves the ski-jump with a large upward velocity but downward acceleration, air speed increases rapidly. Eventually horizontal flight occurs as the Harrier reaches the proper velocity to begin transition to wing borne flight.

The specific force polygons shown in Fig. 20 illustrate this effect. On the left-hand side of the figure, constant velocity, 1-g flight occurs with a thrust specific force that is slightly larger than the vehicle weight. (At this velocity and angle of attack, the aerodynamic forces are very small, and include a slight _negative_ lift force.) Along a trajectory that exhibits increasing velocity ($\dot{V}$=0.6 g) and less than 1-g vertical net specific force ($V\dot{\gamma}$=-0.3 g), less thrust specific force (0.91 g) is needed even though the vehicle is increasing speed rapidly. This is primarily caused by the forward rotation of the thrust vector as the nozzles are rotated rearwards. There is also a beneficial, although
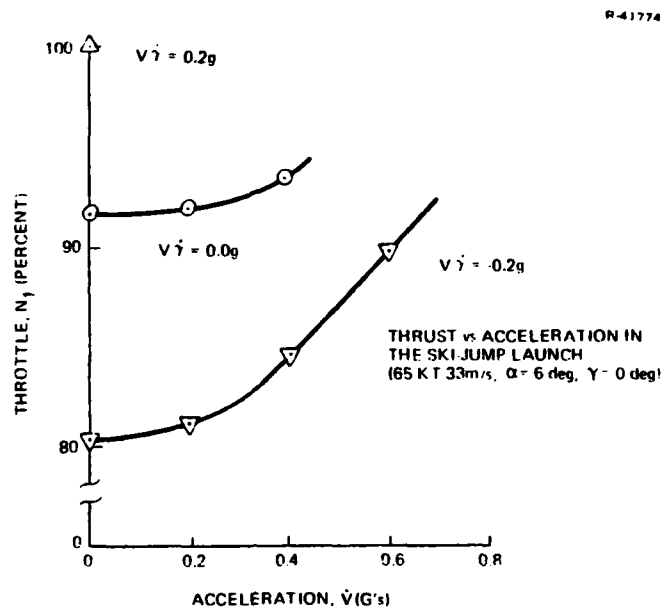
Figure 19   Thrust vs Acceleration in the Ski-Jump Launch
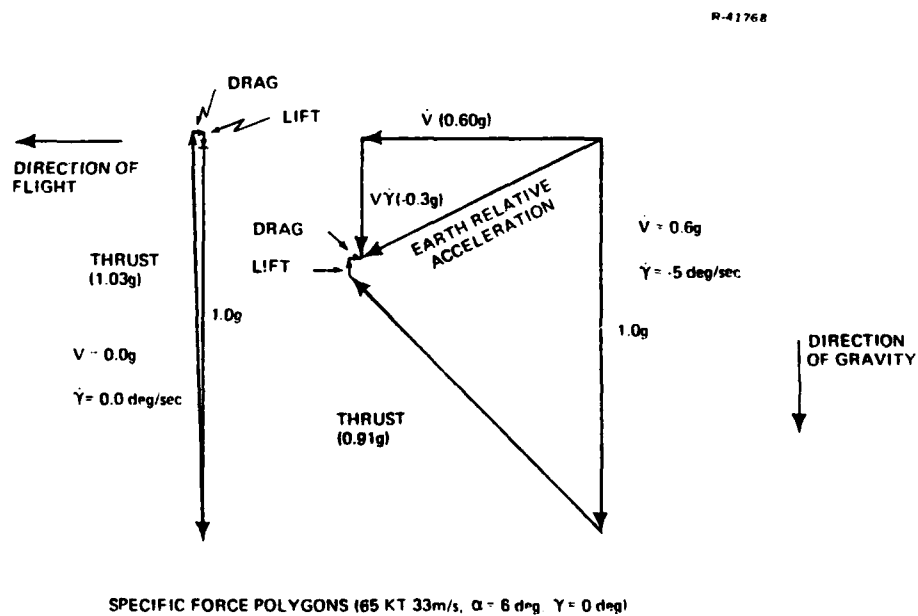
Figure 20   Specific Force Polygons

small, aerodynamic effect, since the flowfield, as modified by
the nozzles, produces positive lift.

To provide vertical clearance for this semi-ballistic
trajectory, the ski-jump launch ramp produces a large upward
initial flight path angle, γ. Increased aerodynamic lift,
caused by increased α may be beneficial also. Figure 21 il-
lustrates the throttle changes necessary to accommodate α and
γ variations. Increased γ requires increased thrust because
of the work necessary to raise the aircraft mass in the gravity
field to a higher potential energy. Higher α allows lower
thrust due to increased aerodynamic lift, and hence a reduced
amount of thrust-supported weight. The specific force polygons
(Fig. 22) illustrate these relationships. The increased lift
and drag at 12 deg α are apparent, as is the increase of thrust
necessary to trim about 12 deg γ. This is compensated, to some
extent, by the reduction in net vertical acceleration from
0.3 g downwards to 0.22 g downwards.

R-41767
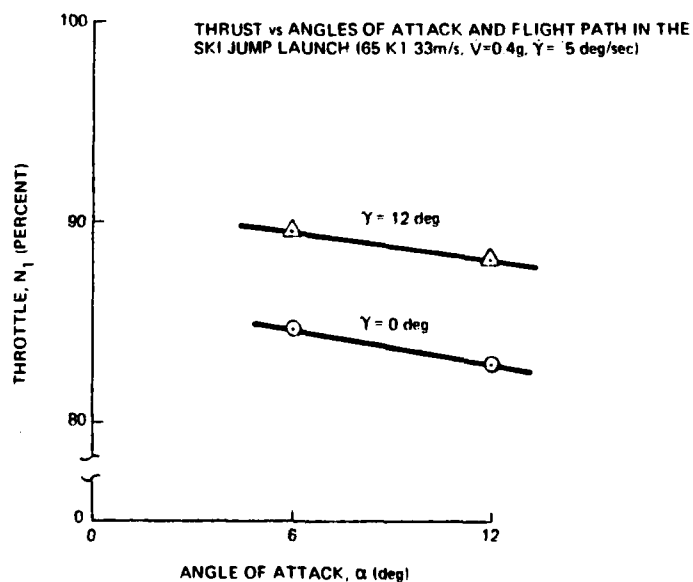
Figure 21   Thrust vs Angles of Attack and Flight Path in
             the Ski-Jump Launch

31

SPECIFIC FORCE POLYGONS (65 KT 33 m/s, $\dot{V}$ = 0.4g, $\dot{\gamma}$ = -5 deg/sec)
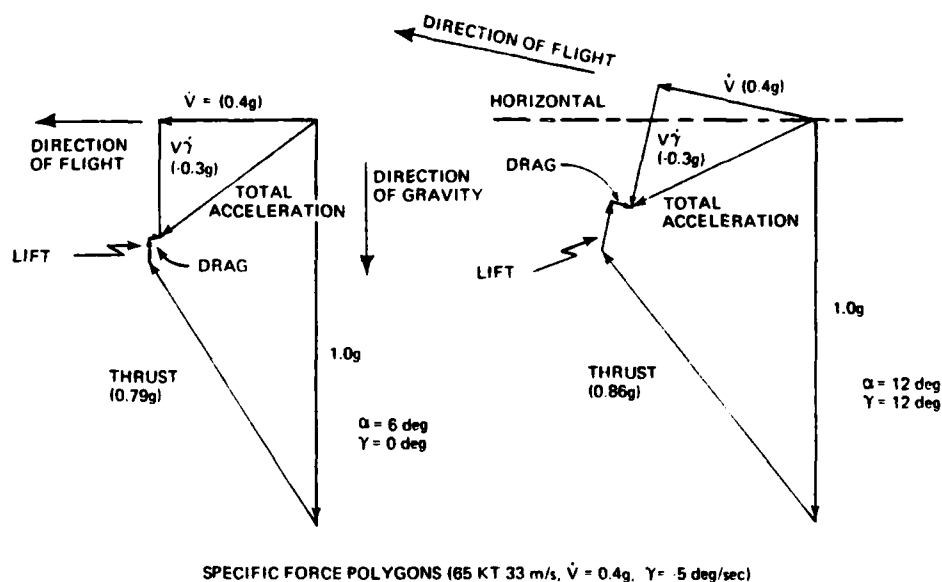
Figure 22   Specific Force Polygons

2.4.2 Stability Variations During the Ski-Jump Launch

The effects of horizontal and vertical acceleration
on AV-8A stability are examined at constant angles of attack
and flight path, α=6 deg, γ=0 deg. Figure 23 illustrates
these variations. The effects on lateral-directional modes
are not especially large, but longitudinal modes vary in a
pattern closely related to that observed in Section 2.3.
Acceleration causes the very stable angle of attack mode to
become even faster, whereas the pitch-speed mode slows and
becomes unstable. The unstable third mode is slowed by ac-
celeration and, for normal specific force of 0.7 g ($\dot{V}\gamma$=-0.3
g), the third mode decomposes into a fast angle of attack
divergence and another real which forms a conventional phu-
goid oscillation as it combines with the pitch-speed root.

Figure 23   Stability Variations Due to Acceleration During a
Ski-Jump Launch

The actual ski-jump launch involves a significant
positive flight path angle, γ, and may involve higher angle of
attack, α. Figure 24 examines the effects of these variables
on vehicle stability. Flight path angle has negligible effect
on the lateral directional modes and on the phugoid mode. Both
the unstable α divergence and the fast, stable, angle-of-attack
modes are faster at γ of 12 deg than in horizontal flight, but
the effect is not especially large. Angle of attack, as shown
in Section 2.3, does have a very significant effect on all
modes. Its effect on the α modes is similar to but larger
than that of flight path angle (on a normalized basis), and
higher α stabilizes the phugoid mode, as expected. Angle of
attack effects on roll and spiral modes are small, but Dutch
roll becomes significantly more unstable as α increases.

33
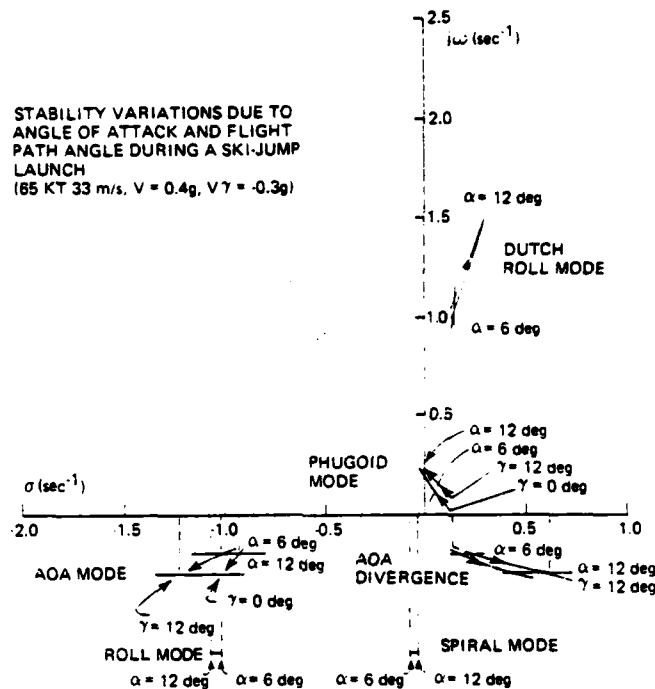
Figure 24   Stability Variations Due to Angle of Attack
             and Flight Path Angle During a Ski-Jump
             Launch

Since angle of attack increase buys relatively little
performance increase at this velocity, as compared to signi-
ficantly poorer Dutch roll and α divergence characteristics,
this analysis indicates that it would be desirable to delay
the α increase until a speed is reached where the performance
gain outweighs the stability difficulty.

2.5   CHAPTER SUMMARY

The range of AV-8A flight conditions from very low
speed through transition to conventional flight is examined in
this chapter. The effects on vehicle stability and control of

velocity, angle of attack, flight path angle and acceleration along and normal to the trajectory are detailed.

Longitudinal Stability depends primarily on nozzle angle, as shown in Fig. 25, which is a composite plot showing the trend of all results presented in this chapter. Aircraft velocity only has a significant effect on the fast, stable α mode. All other effects (angle of attack, flight path angle, and acceleration) primarily affect longitudinal stability because they require a change in nozzle angle for trim. Note that this figure illustrates the general trends with respect to nozzle angle; not all the mode damping values fall exactly on the arrows indicated. This chart suggests that those flight conditions which require nozzle angles less than 45 deg should be avoided.

R-41786
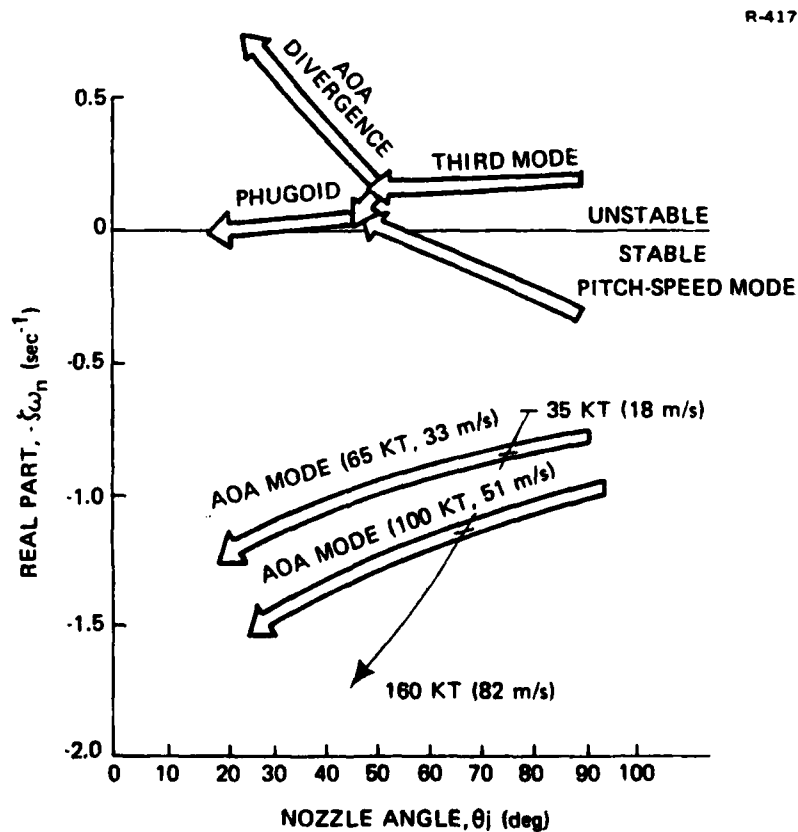
Figure 25   Longitudinal Mode Real Part vs Nozzle Angle

35

Lateral-directional mode stability depends primarily on velocity and angle of attack, with Dutch roll mode becoming unstable at higher angles of attack and lower velocity. Figure 26 illustrates these general trends. Other flight condition variables (nozzle angle, flight path angle, and acceleration) have only secondary effects on lateral-directional stability. This chart suggests that low-speed, high-α flight conditions be avoided. To some extent this suggestion is in conflict with the one given above, since avoidance of high-α flight conditions argues for an early transition to nozzle-borne flight as speed decreases, but this will result in a nozzle angle in the undesirable region.

R-41785
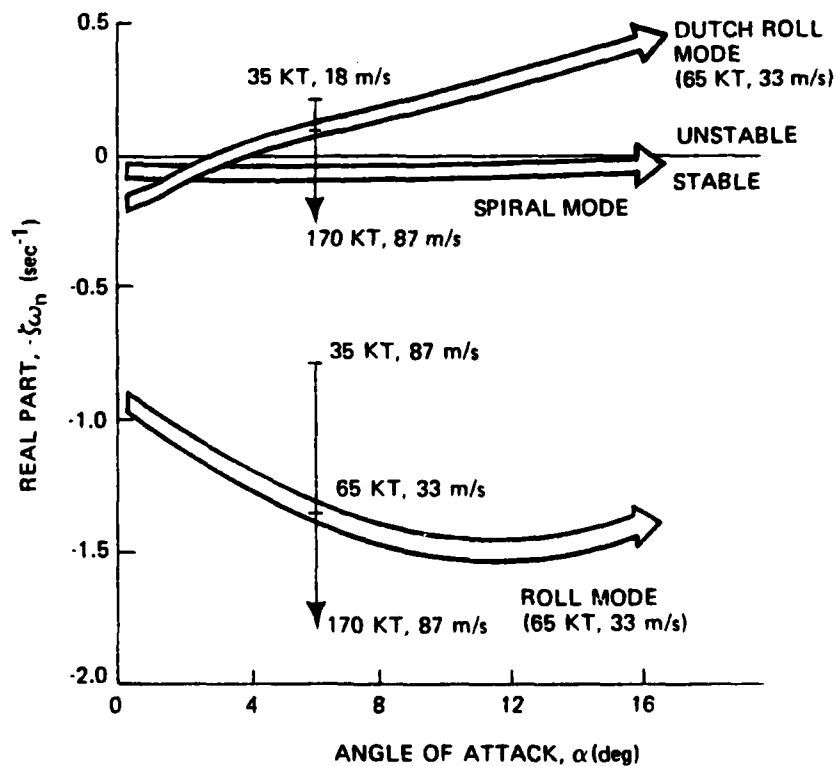
Figure 26   Lateral Mode Real Part vs Angle of Attack

3. DIGITAL COMMAND AUGMENTATION FOR THE AV-8A HARRIER

A flight control system, shown in Fig. 27, basically consists of feedback control from the aircraft state variables to improve stability and feedforward control from the pilot commands to achieve desired aircraft trajectories and some means of adapting this control system to changes in flight condition. Many state feedback and control gain adaptation design procedures have been successfully developed and analyzed (Refs. 18 to 21) but a feedforward control design procedure in both continuous and discrete-time has not been fully developed for aircraft applications.

A common procedure used in pilot feedforward control is to mechanically, and/or electronically connect the pilot's stick, pedals, and throttle controls to the aerodynamic surfaces
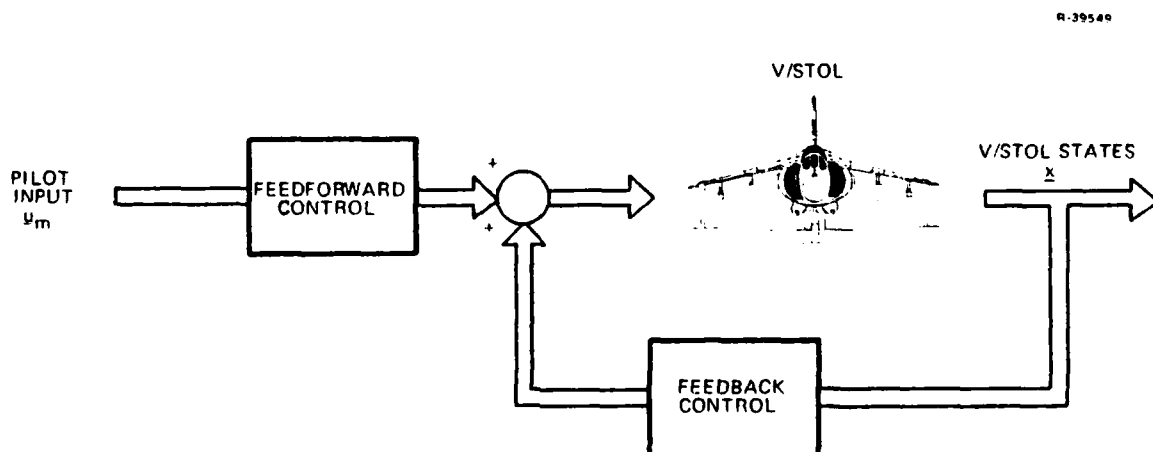
Figure 27   Basic Control Structure

and reaction control jets of the aircraft. Gearing, bob-
weights, and force producing devices are used to provide the
proper pilot tactual information that enhance pilot "feel".
Pilot control of the surfaces and jets means that the pilot in
many instances must coordinate control inputs to achieve de-
sired aircraft state responses. Often control interconnects
are employed to reduce pilot effort in turning flight and to
prevent departures at high angles of attack due to adverse
yaw.

The pilot's inputs do not have to be directly con-
nected to the aircraft's control inputs. With proper feed-
forward control-theoretic formulations, pilot command inputs
can be made to be combinations of aircraft states and controls.
Pilots have reacted favorably to many of the state command
systems such as velocity command and attitude command systems,
Refs. 21 and 24, and the F-16 command system described in Ref.
23. An advanced form of state command systems is model follow-
ing. Early efforts at having the pilot control an ideal air-
craft model then having the actual aircraft states follow the
ideal model states are discussed in Refs. 24 and 25. Essen-
tially all linear state command systems are a special case of
the general model following problem. Unfortunately, under the
conditions specified in Ref. 24, it would appear that perfect
model following is rarely possible. It is the purpose of this
chapter to show that, under a more suitable set of conditions,
perfect model output following is almost always possible.
Model output following can be used in a Digital Flight Con-
trol Systems (DFCS), and it can be designed in combination
with optimal control techniques to yield a desirable feedback/
feedforward DFCS for aircraft. This chapter will present the
results of applying the theoretical model following tools
developed in Appendix A to the AV-8A Harrier.

General CGT theory is employed to determine the feed-forward gains and control structure so that perfect output tracking is accomplished. Non-perfect conditions (parameter uncertainties, etc) occur in practice so a proportional-integral (PI) structure is used in the DFCS design to compensate for condition such as unmodeled slowly varying disturbances and modeling errors.

The CGT is compatible with any feedback design structure, such as optimal control or eigenvalue/eigenvector placement. The eigenvalue/eigenvector placement design, as the name implies, assigns the closed-loop poles of the aircraft to certain desirable locations. In addition, it structurally changes the closed-loop eigenvectors so that the commanded output of the aircraft emulates the output of the command generator. For example, if the command generator dynamics have uncoupled output dynamics then the eigenvalue/eigenvector placement design can force the aircraft to have uncoupled output dynamics. An uncoupled velocity command design will be demonstrated using the Harrier and compared with an optimal control velocity command design.

Both the optimal control design and the eigenvalue/eigenvector placement designs are direct digital realizations which retain continuous-time features. In both cases the designer may use continuous-time criteria which is automatically transformed to discrete time and solved as a discrete time problem. The discrete-time solution presented here is suitable for digital flight computer implementation. For evaluation purposes, the discrete-time closed-loop system is exactly transformed back to continuous time and evaluated using continuous-time specifications such as MIL-F-83300, Ref. 15. It is shown in Ref. 13 that the transformed discrete time solution for the optimal control approach gives essentially the same continuous-time performance as if the problem had been solved directly in

continuous time. The same is true for the eigenvalue/eigenvector placement procedure. Obtaining equivalent performance means that digital designs can be accomplished at lower sample rates. which in turn reduces computer requirements, and allows the use of more complex control algorithms in flight. Closed-loop eigenvalues and analysis of all control designs for the Harrier are presented in continuous-time while control law feedback and feedforward gains are presented in discrete time. The staircased output of the control law is smoothed in simulation plots to obtain a continuous-time representation of control movement.

Once the theoretical tools for digital feedback/feedforward design are discussed, the next task is to construct the command generator model. The AV-8A Harrier aircraft requires a considerably complex model since the aircraft transitions from a high performance aerodynamic vehicle at high speeds to an unstable reaction jet controlled platform at hover. One command generator model cannot be used at all flight conditions to always provide superior performance. The AV-8A has eight available controls and can handle a wide range of command generators. Most of this chapter will concentrate on presenting the results from six command generators used with the Harrier at different flight conditions. Comparisons will then be made and the chapter is concluded with a discussion of the command generators and feedback designs.

3.1 COMMAND GENERATOR TRACKER THEORY-DIGITAL FLIGHT CONTROL SYSTEM DESIGN

3.1.1 Explicit Model Following

The design of the command generator tracker proportional-integral (CGT-PI) control law is based upon the definition of a coupled linear time-invariant model of the AV-8A described as

40

$$\Delta \dot{\underline{x}}(t) = F \Delta \underline{x}(t) + G \Delta \underline{u}(t)$$

where $\Delta \underline{u}(t)$ is an m-vector representing control perturbations and $\Delta \underline{x}(t)$ is an n-vector representing the aircraft's dynamic states. The purpose of the CGT-PI control vector is to stabilize the aircraft about a trajectory where the desired output of the states and controls,

$$\Delta \underline{y}(t) = H \Delta \underline{x}(t) + D \Delta \underline{u}(t)$$

perfectly tracks the output of a linear, time-invariant command generator,

$$\Delta \dot{\underline{x}}_m(t) = F_m \Delta \underline{x}_m(t) + G_m \Delta \underline{u}_m(t)$$

$$\Delta \underline{y}_m(t) = H_m \Delta \underline{x}_m(t) + D_m \Delta \underline{u}_m(t)$$

The m_m-vector $\Delta \underline{u}_m(t)$ represents the pilot's input to the command generator and $\Delta \underline{x}_m(t)$ represents the n_m-vector of the command generators dynamic states. The aircraft output, $\Delta \underline{y}(t)$, and the command generator output, $\Delta \underline{y}_m(t)$, are ℓ-vector and there are at least as many controls as there are commanded outputs. The trajectory the aircraft states and controls follow when perfect tracking occurs is the "star" trajectory and has the property, starting from the initial time, t_0,

$$H \Delta \underline{x}^*(t) + D \Delta \underline{u}^*(t) = H_m \Delta \underline{x}_m(t) + D_m \Delta \underline{u}_m(t)$$

The first simplfying assumption used to obtain a solution for the CGT-PI is that $\Delta \underline{u}_m(t)$ is constant before and after the initial time. The plant is assumed to be tracking the command generator previous to t_0 and at t_0, $\Delta \underline{u}_m$ steps and remains constant. The control must transfer the aircraft from the old

to the new star trajectory caused by stepping $\Delta \underline{u}_m$ while penalizing the deviations

$$\Delta \underline{\tilde{x}} = \Delta \underline{x} - \Delta \underline{x}^* \quad ; \quad \Delta \underline{\tilde{u}} = \Delta \underline{u} - \Delta \underline{u}^* \quad ; \quad \Delta \underline{\tilde{v}} = \Delta \underline{\dot{u}} - \Delta \underline{\dot{u}}^*$$

in the following manner

$$J = \int_0^\infty \left\{ \begin{bmatrix} \Delta \underline{\tilde{x}}^T & \Delta \underline{\tilde{u}}^T \end{bmatrix} Q \begin{bmatrix} \Delta \underline{\tilde{x}} \\ \Delta \underline{\tilde{u}} \end{bmatrix} + \Delta \underline{\dot{\tilde{v}}}^T R \Delta \underline{\dot{\tilde{v}}} \right\} dt$$

The control rate deviative is included in the cost function in order to obtain the proportional-integral property in the control law as shown in Ref. 18.

The command generator tracker for arbitrary $\Delta \underline{u}_m(t)$ is presented in Ref. 12 for the continuous-time case and in Ref. 11 for the discrete-time case. The solution requires the use of compensators whose poles are the transmission zeroes of the plant. In addition, up to n $\Delta \underline{u}_m(t)$ derivatives may be needed for the continuous-time case and up to n future values of $\Delta \underline{u}_{m,k}$ may be needed in the discrete-time case. The complexity of arbitrary $\Delta \underline{u}_m(t)$ inputs exceeds the scope of this work. On the other hand, Ref. 14 demonstrates that the simplifying assumption for $\Delta \underline{u}_m$ presented in the previous paragraph performs very well if $\Delta \underline{u}_m$ is slowly varying when compared to the closed-loop plant time constants.

A digital control law which minimizes the cost function can be obtained by restricting the control, $\Delta \underline{u}$, to change only at equally spaced sampling intervals, Δt. The problem reduces to the sampled-data regulator solved in Ref. 27. The basic equations involved are listed in Table 4. The aircraft model error dynamics are obtained by subtracting the dynamic

42

TABLE 4

TRANSFORMATION OF CONTINUOUS-TIME OPTIMAL CONTROL PROBLEM TO DISCRETE-TIME

CONTINUOUS-TIME AIRCRAFT MODEL ERROR DYNAMICS WITH COMPENSATOR

$$
\begin{bmatrix} \Delta \dot{\tilde{x}} \\ \Delta \dot{\tilde{u}} \end{bmatrix} = \begin{bmatrix} F & G \\ 0 & 0 \end{bmatrix} \begin{bmatrix} \Delta \tilde{x} \\ \Delta \tilde{u} \end{bmatrix} + \begin{bmatrix} 0 \\ I \end{bmatrix} \Delta \tilde{v}
$$

CONTINUOUS-TIME COST FUNCTION

$$
J = \int_0^\infty \left\{ [\Delta \tilde{x}^T \; \Delta \tilde{u}^T] \; Q \begin{bmatrix} \Delta \tilde{x} \\ \Delta \tilde{u} \end{bmatrix} + [\Delta \tilde{v}^T R \Delta \tilde{v}] \right\} dt
$$

DISCRETE-TIME MODEL

$$
\Phi = e^{F \Delta t} \qquad \Gamma = \int_0^{\Delta t} e^{F\tau} \, d\tau \; G
$$

$$
\begin{bmatrix} \Delta \tilde{x} \\ \Delta \tilde{u} \end{bmatrix}_{k+1} = \begin{bmatrix} \Phi & \Gamma \\ 0 & I \end{bmatrix} \begin{bmatrix} \Delta \tilde{x} \\ \Delta \tilde{u} \end{bmatrix}_k + \begin{bmatrix} \sim 0 \\ \Delta t I \end{bmatrix} \Delta \tilde{v}_k
$$

DISCRETE-TIME COST FUNCTION

$$
J = \sum_{k=-1}^{\infty} [\Delta \tilde{x}^T \; \Delta \tilde{u}^T \; \Delta \tilde{v}^T]_k \begin{bmatrix} \hat{Q} & \hat{M} \\ \hat{M}^T & \hat{R} \end{bmatrix} \begin{bmatrix} \Delta \tilde{x} \\ \Delta \tilde{u} \\ \Delta \tilde{v} \end{bmatrix}_k
$$

DISCRETE-TIME WEIGHTING MATRICES

$$
\hat{Q} = \int_0^{\Delta t} e^{\begin{bmatrix} F & G \\ 0 & 0 \end{bmatrix}^T t} \; Q \; e^{\begin{bmatrix} F & G \\ 0 & 0 \end{bmatrix} t} \; dt
$$

$$
\hat{M} = \int_0^{\Delta t} e^{\begin{bmatrix} F & G \\ 0 & 0 \end{bmatrix}^T t} \; Q \left[\int_0^t e^{\begin{bmatrix} F & G \\ 0 & 0 \end{bmatrix} s} \, ds \right] dt \begin{bmatrix} 0 \\ I \end{bmatrix}
$$

$$
\hat{R} = \Delta t R + [0 \; I] \int_0^{\Delta t} \left[\int_0^t e^{\begin{bmatrix} F & G \\ 0 & 0 \end{bmatrix}^T s} \, ds \right] Q \left[\int_0^t e^{\begin{bmatrix} F & G \\ 0 & 0 \end{bmatrix} \tau} \, d\tau \right] dt \begin{bmatrix} 0 \\ I \end{bmatrix}
$$

43

equation for the star trajectory shown in Eq. A-1 (no disturbance) from the aircraft dynamics. The star trajectory is linearly related to the command generator states and controls as shown in Table 5. The feedforward matrix linearly relating the command generator states to the aircraft states satisfies the algebraic matrix equation shown in Table 5. A discussion and techniques for solving the matrix equation are presented in Appendix A. Special attention is given to the importance of transmission zeroes in finding a solution. The discrete-time control law solution is presented in Table 6 for the linearized dynamics. The closed-loop discrete-time system is obtained by converting the PI control law in incremental form back to the position form as shown in Ref. 26. Eigenvalue evaluation of the control law is obtained by mapping theclosed-loop discrete-time matrix back to an equivalent continuous-time plant using the natural logarithm of a matrix. Only eigenvalues in the primary band in the s-domain are computed. High frequency states such as body bending modes are not considered in this analysis, hence frequency folding problems do not occur as we transform back and forth between continuous and discrete time.

The CGT-PI control in incremental form that would be implemented onboard the aircraft flight computer has the form

$$
\underline{u}_k = \underline{u}'_{k-1} - C_1(\underline{x}_k - \underline{x}_{k-1}) - \Delta t C_2(\underline{y}_{k-1} - \underline{y}_{m,k-1})
$$
$$
+ [A_{21} + C_1 A_{11}] (\underline{x}_{m,k} - \underline{x}_{m,k-1})
$$

(3)

and uses total variables. When perfect tracking occurs the command error $\underline{y}_{k-1} - \underline{y}_{m,k}$ is zero, the control contribution $-C_1(\underline{x}^*_k - \underline{x}^*_{k-1})$ is cancelled by $C_1 A_{11}(\underline{x}_{m,k} - \underline{x}_{m,k-1})$ and $A_{21}(\underline{x}_{m,k} - \underline{x}_{m,k-1})$ is the feedforward term to add to $\underline{u}'_{k-1}$ to ensure $\underline{u}_k$ maintains the tracking. As discussed in Appendix A, the command generators are chosen so that either the pilot's

TABLE 5

TRANSFORMATION OF COMMAND GENERATOR TRACKER TO DISCRETE-TIME

T-2902

DISCRETE-TIME COMMAND GENERATOR MODEL

$$\Phi_m = e^{F_m \Delta t} \qquad \Gamma_m = \int_0^{\Delta t} e^{F_m \tau} \, d\tau \; G_m$$

$$\Delta \underline{x}_{m,k+1} = \Phi_m \, \Delta \underline{x}_{m,k} + \Gamma_m \, \Delta \underline{u}_m$$

DISCRETE-TIME STAR TRAJECTORY

$$\begin{bmatrix} \Delta \underline{x}_k^* \\ \Delta \underline{u}_k^* \end{bmatrix} = \begin{bmatrix} A_{11} & A_{12} \\ A_{21} & A_{22} \end{bmatrix} \begin{bmatrix} \Delta \underline{x}_{m,k} \\ \Delta \underline{u}_m \end{bmatrix}$$

FEEDFORWARD MATRIX EQUATION

$$\begin{bmatrix} (\Phi - I) & \Gamma \\ H & D \end{bmatrix} \begin{bmatrix} A_{11} & A_{12} \\ A_{21} & A_{22} \end{bmatrix} = \begin{bmatrix} A_{11}(\Phi_m - I) & A_{11}\Gamma_m \\ H_m & D_m \end{bmatrix}$$

$\underline{u}_{m,k}$ inputs eventually must return to zero making $\underline{x}_{m,k} - \underline{x}_{m,k-1}$ zero (example: acceleration commands) or the matrices A_{21} and A_{11} are sparse with entries occuring because of geometrical considerations. For implementation C_1, C_2, and any entries occuring in A_{21} and A_{11} which cannot be reconciled based on the physical geometry of the problem would be gain scheduled with flight conditions as discussed in Ref. 26. It is possible to eliminate the term in the control law which uses A_{21} and A_{11} using a discrete-time version of Davison's Servocompensator shown in Ref. 23, and an example is given in Appendix A. The prime on $\underline{u}_{k-1}'$ indicates that the control command should be limited to the natural control limits of the aircraft in order to prevent windup as discussed in Ref. 14. A block diagram of the control law is shown in Fig. 28 for linear command generators.

45

TABLE 6

SOLUTION OF THE DISCRETE-TIME OPTIMAL CONTROL PROBLEM

DISCRETE-TIME RICCATI EQUATION

$$\Phi_D = \begin{bmatrix} \Phi & \Gamma \\ 0 & I \end{bmatrix} \qquad \Gamma_D = \begin{bmatrix} 0 \\ \Delta t I \end{bmatrix}$$

$$P = \Phi_D^T P \Phi_D - (\Gamma_D^T P \Phi_D + \hat{M}^T)^T (\hat{R} + \Gamma_D^T P \Gamma_D)^{-1}$$
$$(\Gamma_D^T P \Phi_D + \hat{M}^T) + \hat{Q}$$

TYPE 0 DISCRETE-TIME OPTIMAL CONTROL LAW GAINS

$$[K_1 \quad K_2] = (\hat{R} + \Gamma_D^T P \Gamma_D)^{-1} (\Gamma_D^T P \Phi_D + \hat{M}^T)$$

TYPE 1 DISCRETE-TIME OPTIMAL CONTROL LAW GAINS

$$[C_1 \quad \Delta t C_2] \begin{bmatrix} (\Phi - I) & \Gamma \\ H & D \end{bmatrix} = [\Delta t K_1 \quad \Delta t K_2]$$

PI CONTROL LAW IN INCREMENTAL FORM

ERROR DYNAMICS:

$$\Delta \tilde{u}_k = \Delta \tilde{u}_{k-1} - C_1 (\Delta \tilde{x}_k - \Delta \tilde{x}_{k-1}) - \Delta t C_2 \Delta \tilde{y}_{k-1}$$

ORIGINAL VARIABLES:

$$\Delta \underline{u}_k = \Delta \underline{u}_{k-1} - C_1 [\Delta \underline{x}_k - \Delta \underline{x}_{k-1}] - \Delta t C_2 \Delta \underline{y}_{k-1} - (H_m D_m) \begin{bmatrix} \Delta \underline{x}_{m,k-1} \\ \Delta \underline{u}_{m,k} \end{bmatrix}$$
$$+ [A_{21} + C_1 A_{11}] [\Delta \underline{x}_{m,k} - \Delta \underline{x}_{m,k-1}]$$

CLOSED-LOOP DISCRETE-TIME SYSTEM

$$\Phi_{CL} = \begin{bmatrix} \Phi - \Gamma C_1 & -\Gamma C_2 \\ \Delta t H - \Delta t D C_1 & I - \Delta t D C_2 \end{bmatrix}$$

EQUIVALENT CLOSED-LOOP CONTINUOUS-TIME SYSTEM

$$F_{CL} = \frac{1}{\Delta t} \ln \Phi_{CL} = \frac{1}{\Delta t} \left[(\Phi_{CL} - I) - \frac{1}{2} (\Phi_{CL} - I)^2 + \frac{1}{3} (\Phi_{CL} - I)^3 - \cdots \right]$$

Figure 28   Diagram of the CGT-PI Control Law

3.1.2 Implicit Model Following

In this section an alternate procedure is presented
for determining the stabilization gains in the CGT-PI control
law. The procedure provides a technique for choosing gains
which cause the closed-loop aircraft dynamics to have the same
eigenvalues as a _desirable_ aircraft model _and_ restructures the
eigenvectors of the closed-loop aircraft dynamics so that
output transients of the aircraft are the same as the desir-
able aircraft model. The procedure is the solution to the
implicit model following problem and is accomplished using the
feedforward matrices in the CGT under special conditions. A

47

discussion and derivation of the eigenvalue/eigenvector place-
ment procedure is given in Appendix A.4. This procedure is
used in one of the AV-8A control designs in Section 3.4.

The equations for solving the eigenvalue/eigenvector
placement (EEP) problem for the CGT-PI control law are out-
lined in Table 7. The same aircraft error dynamics as in the
optimal control problem are used. The EEP gains are to sta-
bilize the plant about the star trajectory. It is important
to realize that the command generator producing the star tra-
jectory is usually not the same as the ideal aircraft model
used in the EEP problem. The ideal aircraft model in Table 7
represents the designers choice of how the closed-loop air-
craft and compensator transient dynamics should behave. The
designer can almost always only match m $\Delta\tilde{y}$ transients to m $\Delta\tilde{y}_m$
desirable transients, where m is the number of aircraft con-
trols. Insufficient control power will reduce the number of
matching transients even further. Once the EEP gains are
determined, the control law is the same as Eq. 3 and can be
evaluated using the same equivalent closed-loop continuous-
time system shown in Table 6.

Both design procedures shown in Section 3.1.1 and in
this section are direct digital designs. In optimal control,
performance is changed by adjusting the continuous-time weight-
ing matrices Q and R independent of the sampling-time. In
EEP, performance is changed by adjusting the elements in F_m',
G_m', T_x and T_u also independent of the sampling-time. A com-
parison between an optimal control design and the EEP design
is presented in Section 3.3.4.

TABLE 7

SOLUTION OF THE DISCRETE-TIME
EIGENVALUE/EIGENVECTOR PROBLEM

T-2904

CONTINUOUS-TIME AIRCRAFT MODEL ERROR DYNAMICS WITH COMPENSATOR

$$\begin{bmatrix} \Delta\dot{\tilde{x}} \\ \Delta\dot{\tilde{u}} \end{bmatrix} = \begin{bmatrix} F & G \\ 0 & 0 \end{bmatrix} \begin{bmatrix} \Delta\tilde{x} \\ \Delta\tilde{u} \end{bmatrix} + \begin{bmatrix} 0 \\ I \end{bmatrix} \Delta\tilde{v} \qquad \Delta\tilde{y} = H_A \Delta\tilde{x}$$

CONTINUOUS-TIME IDEAL AIRCRAFT MODEL ERROR DYNAMICS WITH IDEAL COMPENSATOR $(n=n_m)$

$$\begin{bmatrix} \Delta\dot{\tilde{x}}_m \\ \Delta\dot{\tilde{u}}_m \end{bmatrix} = \begin{bmatrix} F_m' & G_m' \\ T_x & T_u \end{bmatrix} \begin{bmatrix} \Delta\tilde{x}_m \\ \Delta\tilde{u}_m \end{bmatrix} \qquad \Delta\tilde{y}_m = H_m' \Delta\tilde{x}$$

DISCRETE-TIME MODELS

$$\phi_A = e^{\begin{bmatrix} F & G \\ 0 & 0 \end{bmatrix}\Delta t} \qquad \Gamma_A = \int_0^{\Delta t} e^{\begin{bmatrix} F & G \\ 0 & 0 \end{bmatrix} t} \, dt \begin{bmatrix} 0 \\ I \end{bmatrix}$$

$$\phi_m' = e^{\begin{bmatrix} F_m' & G_m' \\ T_x & T_u \end{bmatrix}\Delta t} \qquad \phi = e^{F\Delta t} \qquad \Gamma = \int_0^{\Delta t} e^{Ft} \, dt \, G$$

FEEDFORWARD MATRIX EQUATION FOR CONTROL GAINS

$$\begin{bmatrix} (\phi_A - I) & \Gamma_A \\ H_A & 0 \end{bmatrix} \begin{bmatrix} A_{11} \\ A_{12} \end{bmatrix} = \begin{bmatrix} A_{11}(\phi_m' - I) \\ H_m \end{bmatrix}$$

TYPE 0 DISCRETE-TIME EIGENVALUE/EIGENVECTOR PLACEMENT GAINS

$$[K_1 \quad K_2] = A_{12} \, A_{11}^{-1}$$

TYPE 1 DISCRETE-TIME EIGENVALUE/EIGENVECTOR PLACEMENT GAINS

$$[C_1 \quad \Delta t C_2] \begin{bmatrix} (\phi - I) & \Gamma \\ H & D \end{bmatrix} = [\Delta t K_1 \quad \Delta t K_2]$$

PI CONTROL LAW

  (SAME AS IN TABLE 6)

3.2 COMMAND ANALYSIS FOR THE AV-8A AIRCRAFT

The AV-8A aircraft has ten control surfaces, reaction jets, and engine controls which are then reduced to eight controls in Appendix C. The eight controls which can be commanded by the DFCS are: RPM, ΔN_1; stabilator, $\Delta \delta_s$; nozzle angle, $\Delta \theta_j$; pitch jets, $\Delta \delta_{pj}$; for the longitudinal axis and aileron, $\Delta \delta_a$; roll jets, $\Delta \delta_{rj}$; rudder, $\Delta \delta_r$; and yaw jet, $\Delta \delta_{yj}$; for the lateral-directional axis. Theoretically it should be possible to command eight independent combinations of states and controls with eight independent controls. Practically for aircraft, the control effect matrix, G, has at most rank six, hence sufficient control power is available for commanding six combinations of states and control. The values in the feedforward matrices S_{21} and S_{22} indicate how much travel is needed by the controls to produce the desired response. The more control power available, the smaller the numbers are in S_{21} and S_{22} relative to the maximum control throw. An example of values in S_{21} and S_{22} using various mixes of controls and commands is presented in the next three sections. In all cases except for very low speed flight, the command systems for the AV-8A designs in this chapter will have fewer commands than controls because of insufficient control power.

The V/STOL aircraft undergoes substantial changes in characteristics as the vehicle transitions from high speed to hover. More than one command system is needed to optimize piloting tasks depending on the flight condition. Examples of using more than one command system onboard an aircraft with the pilot either choosing the appropriate one or the computer phasing the systems in and out are shown in Refs. 23, 29, and 30. In this study, six different command and control systems shown in Table 8 are constructed, designed, and simulated. Each command model is determined by the desired pilot commands, $\underline{u}_m$, the desired model output vector, $\underline{y}_m$, and the available

50

TABLE 8

COMMANDS, STATES, AND CONTROLS FOR THE AV-8A

T-2905

AIR COMBAT MANEUVERING RAMP/STEP MODEL	$\underline{u}_m^T = [\dot{V}_m \ a_{n,m} \ \alpha_m \ p_{w,m} \ \beta_m]$
	$\underline{x}_m^T = [V_m \ \gamma_m \ \phi_{v,m}]$
	$\underline{y}_m^T = [V_m \ \gamma_m \ \alpha_m \ \phi_{v,m} \ \beta_m]$
	$\underline{x}^T = [\theta \ u \ q \ w \ v \ r \ p \ \phi]$
	$\underline{u}^T = [N_1 \ \delta_s \ \theta_j \ \delta_a \ \delta_r \ \delta_{yj}]$
COORDINATED TURN DYNAMIC MODEL	$\underline{u}_m^T = [\delta_{VDR,m} \ \delta_{q,m} \ \delta_{Vz,m} \ \delta_{v,m} \ \delta_{r,m}]$
	$\underline{x}_m^T = [z_m \ \theta_m \ V_{DR,m} \ q_m \ V_{z,m} \ v_m \ r_m \ \psi_m]$
	$\underline{y}_m^T = [V_{DR,m} \ \theta_m \ z_m \ \beta_m \ \psi_m]$
	$\underline{x}^T = [z \ \theta \ u \ q \ w \ v \ r \ p \ \phi \ \psi]$
	$\underline{u}^T = [N_1 \ \delta_s \ \theta_j \ \delta_{pj} \ \delta_a \ \delta_{rj} \ \delta_r \ \delta_{yj}]$
COORDINATED TURN RAMP/STEP MODEL	$\underline{u}_m^T = [a_{DR,m} \ V_{z,m} \ \theta_m \ \dot{\beta}_m \ \dot{\psi}_m]$
	$\underline{x}_m^T = [z_m \ V_{DR,m} \ \beta_m \ \psi_m]$
	$\underline{y}_m^T = [z_m \ V_{DR,m} \ \theta_m \ \beta_m \ \psi_m]$
	$\underline{x}^T = [z \ \theta \ u \ q \ w \ v \ r \ p \ \phi \ \psi]$
	$\underline{u}^T = [N_1 \ \delta_s \ \theta_j \ \delta_{pj} \ \delta_a \ \delta_{rj} \ \delta_r \ \delta_{yj}]$
ENROUTE VELOCITY COMMAND RAMP/STEP MODEL	$\underline{u}_m^T = [a_{DR,m} \ V_{z,m} \ \theta_m \ a_{CR,m} \ \dot{\psi}_m]$
	$\underline{x}_m^T = [V_{DR,m} \ z_m \ V_{CR,m} \ \psi_m]$
	$\underline{y}_m^T = [V_{DR,m} \ z_m \ \theta_m \ V_{CR,m} \ \psi_m]$
	$\underline{x}^T = [z \ \theta \ u \ q \ w \ v \ r \ p \ \phi \ \psi]$
	$\underline{u}^T = [N_1 \ \delta_s \ \theta_j \ \delta_{pj} \ \delta_a \ \delta_{rj} \ \delta_r \ \delta_{yj}]$
TERMINAL AREA VELOCITY COMMAND RAMP/STEP MODEL	$\underline{u}_m^T = [V_{DR,m} \ V_{z,m} \ \theta_m \ V_{CR,m} \ \dot{\psi}_m]$
	$\underline{x}_m^T = [x_m \ z_m \ y_m \ \psi_m]$
	$\underline{y}_m^T = [x_m \ z_m \ \theta_c \ y_m \ \psi_m]$
	$\underline{x}^T = [x \ z \ \theta \ u \ q \ w \ v \ r \ p \ \phi \ \psi \ y]$
	$\underline{u}^T = [N_1 \ \theta_j \ \delta_{pj} \ \delta_{rj} \ \delta_{yj}]$
TERMINAL AREA ATTITUDE COMMAND RAMP/STEP MODEL	$\underline{u}_m^T = [V_{DR,m} \ V_{z,m} \ \theta_m \ \phi_m \ \dot{\psi}_m]$
	$\underline{x}_m^T = [x_m \ z_m \ \psi_m]$
	$\underline{y}_m^T = [x_m \ z_m \ \theta_m \ \phi_m \ \psi_m]$
	$\underline{x}^T = [x \ z \ \theta \ u \ q \ w \ v \ r \ p \ \phi \ \psi]$
	$\underline{u}^T = [N_1 \ \theta_j \ \delta_{pj} \ \delta_{rj} \ \delta_{yj}]$

controls, $\underline{u}$. All command models have five pilot inputs. Two inputs for lateral and longtitudinal stick, one input for the other hand (usually consisting of a speed command), one input for the pedals and the fifth input can be a thumb button for a rate command (or a thumb wheel for a position command). The rate commands are model inputs, $\underline{u}_m$, which are integrated by the model to generate a state, $\underline{x}_m$, that is used in $\underline{y}_m$. For example, a step in the vertical velocity command, $V_{z,c}$, causes the position command, z_m, in the model to be a ramp. A position command is a model input that is directly used in $\underline{y}_m$ such as the pitch angle command. An example of the model state equations using the enroute velocity command system for demonstration purposes is shown in Eqs. B-1 and B-2.

In the first four command models in Table 8 there are more controls than commands. There are a number of procedures for designing the control system with excess controls. A practical but conservative approach is to interconnect two controls to form one control and continue this process until the commands and controls are equal, as is done in the current AV-8A control system. The interconnect can be chosen so that the controls saturate at the same time. An alternate approach is to use a weighted pseudoinverse to find the feedforward matrices in Eq. A-7 and the feedback matrices for CGT-PI in Eq. A-28. The pseudoinverse optimally decides how to use the excess controls to accommodate the commands. A pseudoinverse design discussing its many features is presented in Refs. 10 and 14 for a fighter aircraft. More implications about the pseudoinverse design which is the method used for the AV-8A is addressed in Section 3.3.

The V/STOL flight regimes as an aircraft approaches a ship to land can be considered to have three regions; high speed flight, transition, and low speed flight to hover. An example of these regions in the AV-8A approach profile, taken

from Ref. 7 is shown in Fig. 29. The rest of this section
discusses the command models most applicable to each regime.

3.2.1 High Speed Flight

The AV-8A at high speeds is commanded by the pilot
using the air combat maneuvering (ACM) ramp/step model in
Table 8. The high speed flight condition is chosen at the
extreme of the available AV-8A flight data, 87.6 m/s (170 kt)
straight-and-level flight. The pilot command generator inputs
are vehicle velocity rate, $\dot{V}$, normal acceleration, a_n, angle
of attack, α, roll rate about the velocity vector, p_w, and
sideslip, β. The command generator states are vehicle ve-
locity, V, flight path angle, γ, and wind-axis roll angle,
Φ_V. The ACM ramp/step model is the most complex of the com-
mand generator models and is fully described in Appendix B.1.
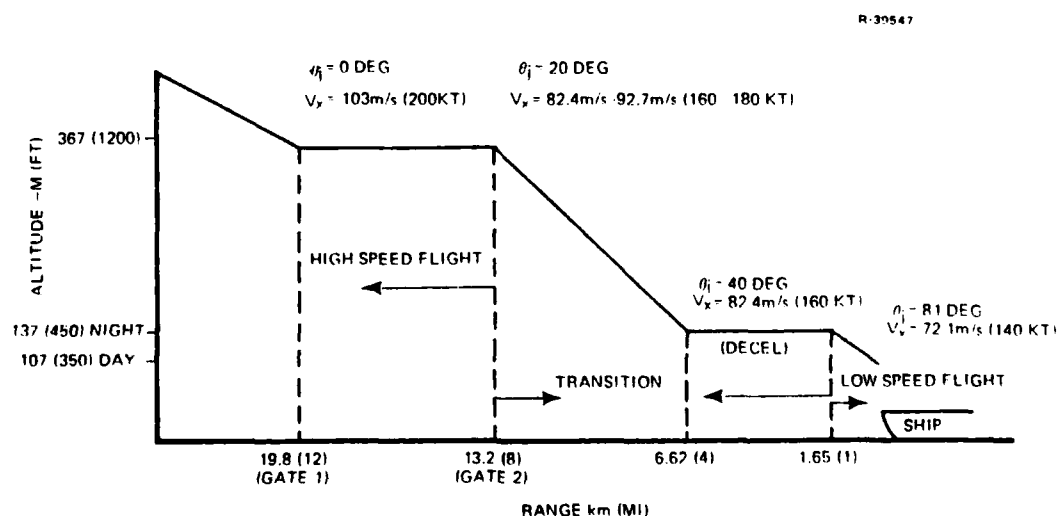
Figure 29   AV-8A Approach Profile

53

The ACM ramp/step model is a generalization using the command generator tracker of the ACM command vector used in Ref. 14. The design in Ref. 14 required that the Euler angles, ϕ and θ, be removed from the aircraft state vector for design because the angles do not approach a constant value when a rate is commanded. The CGT eliminates this difficulty by using command generator states, γ_m and $\phi_{V,m}$, which are also not constant for a rate command and are related linearly to θ and ϕ. The ACM ramp/step design greatly improves the performance of outer-loop tracking, which tended to be inferior in Ref. 14.

Originally, the ACM model included lateral acceleration, $\Delta a_{y,m}$, the velocity heading angle, $\Delta \xi_m$, and eight controls. The resulting feedforward matrices, S_{21} and S_{22} (in English units) then become

$$
\begin{bmatrix}
\Delta N_1^* \\
\Delta \delta_s^* \\
\Delta \theta_j^* \\
\Delta \delta_{pj}^* \\
\Delta \delta_a^* \\
\Delta \delta_{rj}^* \\
\Delta \delta_r^* \\
\Delta \delta_{yj}^*
\end{bmatrix}
=
\begin{bmatrix}
0.138 & 0.769 & 0.950 & \sim 0 \\
\sim 0 & 0.0418 & 0.556 & \sim 0 \\
-0.0119 & \sim 0 & \sim 0 & \sim 0 \\
\sim 0 & -0.0121 & -0.255 & \sim 0 \\
-0.0143 & -0.0763 & -6.77 & \sim 0 \\
-0.0166 & -0.0882 & -10.8 & \sim 0 \\
\sim 0 & 0.0501 & -27.0 & -0.00237 \\
\sim 0 & -0.0206 & 8.28 & \sim 0
\end{bmatrix}
\begin{bmatrix}
\Delta V_m \\
\Delta \gamma_m \\
\Delta \phi_{V,m} \\
\Delta \xi_m
\end{bmatrix}
$$

(4)

$$
+
\begin{bmatrix}
1.37 & 0.958 & 1.44 & \sim 0 & 0.478 & -8.50 \\
0.074 & 0.0350 & 0.541 & 0.0183 & -0.263 & -4.96 \\
-0.0115 & 0.244 & -0.225 & \sim 0 & \sim 0 & -0.074 \\
-0.0214 & \sim 0 & -0.253 & \sim 0 & 0.130 & 2.27 \\
-0.137 & -0.0962 & -0.133 & -0.101 & 1.32 & 60.4 \\
-0.159 & -0.111 & -0.154 & -0.368 & 5.37 & 96.7 \\
0.0860 & 0.0604 & 0.0856 & -0.779 & 11.7 & 24.1 \\
-0.0358 & -0.0251 & -0.0354 & 0.162 & -1.28 & -74.0
\end{bmatrix}
\begin{bmatrix}
\Delta \dot{V}_m \\
\Delta a_{n,m} \\
\Delta \sigma_m \\
\Delta p_{w,m} \\
\Delta \beta_m \\
\Delta a_{y,m}
\end{bmatrix}
$$

The longitudinal-lateral-directional coupling evident in Eq. 4 is caused by the coupling in the control effect matrix, Γ, due to the reaction jets. For minor $\Delta a_{y,m}$ commands all four lateral directional controls saturate as shown in the last column of the matrix A_{22} in Eq. 4. Thus, the AV-8A does not have adequate side-force control power. The feedforward matrices are recomputed by eliminating $a_{y,m}$ and ξ_m from the model and δ_{rj} and δ_{pj} from the controls. This results in

$$
\begin{bmatrix} \Delta N_1^* \\ \Delta \delta_s^* \\ \Delta n_j^* \\ \Delta \delta_a^* \\ \Delta \delta_r^* \\ \Delta \delta_{yj}^* \end{bmatrix} =
\begin{bmatrix}
0.141 & 0.782 & -0.00336 \\
-0.0121 & 0.0423 & \sim 0 \\
-0.0117 & -0.00658 & \sim 0 \\
-0.00109 & -0.00608 & -0.00747 \\
0.0139 & 0.0771 & -0.00460 \\
-0.00454 & -0.0252 & -0.01
\end{bmatrix}
\begin{bmatrix} v_m \\ \gamma_m \\ \phi_{v,m} \end{bmatrix}
$$

$$
+ \begin{bmatrix}
1.40 & 0.975 & 1.47 & -0.0328 & 0.706 \\
0.0748 & 0.0273 & 0.653 & \sim 0 & 0.00855 \\
-0.0123 & 0.244 & -0.235 & \sim 0 & \sim 0 \\
-0.0109 & -0.00756 & -0.0115 & 0.148 & -2.21 \\
0.138 & 0.0961 & 0.145 & -0.0237 & 0.589 \\
-0.0451 & -0.0314 & -0.0474 & -0.0976 & 2.10
\end{bmatrix}
\begin{bmatrix} \Delta \dot{v}_m \\ \Delta a_{n,m} \\ \Delta \alpha_m \\ \Delta p_{w,m} \\ \Delta \beta_m \end{bmatrix}
\tag{5}
$$

The values in Eq. 5 indicate a sufficient operating range before control saturation. Futhermore, the control operating range is not significantly decreased by removing δ_{pj} and δ_{rj} as active controls. The yaw jet, δ_{yj} is included because improved directional stability at high angles of attack could result by using a control whose control power does not depend on the fuselage blocked air stream.

55

3.2.2 Transition

Three command generators are used at two transition
flight conditions; the coordinated turn dynamic model, the
coordinated turn ramp/step model, and the enroute velocity
ramp/step model. The two transition flight conditions are at
51.5 m/s (100 kt) and 18 m/s (35 kt). The dynamic model is
included in the command generators to compare dynamic model
following with ramp/step model following. A complete de-
scription of the dynamic model is given in Appendix B. Dy-
namic models constitute the majority of modern control model
following results as evidenced in Refs. 25 and 31 to 33.
Ramp/step models have previously been ignored in modern control
analysis (the required theory has only recently become avail-
able) but ramp/step models are used in many classical designs
(e.g., Ref. 22).

The coordinated turn and enroute velocity ramp/step
models differ in that sideslip, β, is tracked in the former
while cross-range velocity, V_{CR}, is tracked in the later
model. The downrange and crossrange velocities are obtained
by rotating the inertial velocities of the vehicle by the com-
manded body heading angle ψ_m. In a steady-state turn without
wind and V_{CR} commanded to zero, sideslip is also zero. The
enroute velocity ramp/step system is similiar to the flight
tested velocity command system in Ref. 26.

The coordinated turn ramp/step and dynamic models
have the same command vector, $\underline{y}$, but markedly different feed-
forward matrices. Of particular interest are the feedforward
matrices S_{11} and S_{21} which must be gain scheduled for CGT-PI
implementation. The next four equations show S_{11} and S_{21} for
the dynamic and ramp/step models, respectively, at 51.5 m/s
(100 kt). The dynamic model requires at least 65 nonzero

$$
\begin{bmatrix}
\Delta z^* \\
\Delta \theta^* \\
\Delta u^* \\
\Delta q^* \\
\Delta w^* \\
\Delta v^* \\
\Delta r^* \\
\Delta p^* \\
\Delta \phi^* \\
\Delta \psi^*
\end{bmatrix}
=
\begin{bmatrix}
1.0 & 0 & 0 & 0 & 0 & 0 & 0 & 0 \\
0 & 1.0 & 0 & 0 & 0 & 0 & 0 & 0 \\
0 & -0.410 & 0.990 & 0 & -0.139 & 0 & 0 & 0 \\
0 & -0.0119 & 0 & 0.991 & 0 & 0 & 0 & 0 \\
0 & 2.92 & 0.139 & 0 & 0.989 & 0 & 0 & 0 \\
0 & 0 & 0 & 0 & 0 & 1.0 & 0 & 0 \\
0 & 0 & 0 & 0 & 0 & 0 & 0.99 & 0 \\
0 & 0.00736 & 0 & 0.00247 & -0.00517 & -2.48 & 3.79 & 0 \\
0 & -0.00515 & 0 & -0.00186 & 0.00344 & -0.138 & -2.82 & 0 \\
0 & 0 & 0 & 0 & 0 & 0 & 0 & 1.0
\end{bmatrix}
\begin{bmatrix}
\Delta z_m \\
\Delta \theta_m \\
\Delta u_m \\
\Delta q_m \\
\Delta w_m \\
\Delta v_m \\
\Delta r_m \\
\Delta \psi_m
\end{bmatrix}
+ S_{12}\Delta \underline{u}_m
$$

$$
\begin{bmatrix}
\Delta z^* \\
\Delta \theta^* \\
\Delta u^* \\
\Delta q^* \\
\Delta w^* \\
\Delta v^* \\
\Delta r^* \\
\Delta p^* \\
\Delta \phi^* \\
\Delta \psi^*
\end{bmatrix}
=
\begin{bmatrix}
1 & 0 & 0 & 0 \\
0 & 0 & 0 & 0 \\
0 & 0.99 & 0 & 0 \\
0 & 0 & 0 & 0 \\
0 & 0.139 & 0 & 0 \\
0 & 0 & 2.95 & 0 \\
0 & 0 & 0 & 0 \\
0 & 0 & 0 & 0 \\
0 & 0 & 0.587 & 0 \\
0 & 0 & 0 & 1
\end{bmatrix}
\begin{bmatrix}
\Delta z_m \\
\Delta V_{DR,m} \\
\Delta \beta_m \\
\Delta \psi_m
\end{bmatrix}
+ S_{12}\Delta \underline{u}_m
$$

$$
\begin{bmatrix} \Delta N^*_l \\ \Delta \delta^*_s \\ \Delta \theta^*_j \\ \Delta \delta^*_{pj} \\ \Delta \delta^*_a \\ \Delta \delta^*_{rj} \\ \Delta \delta^*_r \\ \Delta \delta^*_{yj} \end{bmatrix} = \begin{bmatrix} 0 & -0.936 & -0.196 & -0.150 & 1.21 & -0.0179 & 0.00140 & 0 \\ 0 & -0.110 & 0.161 & 0.244 & 0.150 & 0.0204 & 0.0102 & 0 \\ 0 & -1.43 & 0.774 & 0.0092 & 0.105 & 0.0433 & 0.0154 & 0 \\ 0 & -1.09 & 0.0616 & -0.558 & 0.318 & -0.0229 & -0.0104 & 0 \\ 0 & -0.0108 & 0.0178 & 0.00963 & -0.00925 & 0.229 & 0.0735 & 0 \\ 0 & -0.00404 & 0.00597 & 0.00341 & -0.00236 & -0.664 & -0.258 & 0 \\ 0 & -0.0136 & -0.00438 & 0.00153 & 0.0257 & 0.0229 & -0.0200 & 0 \\ 0 & \sim 0 & \sim 0 & \sim 0 & -0.00222 & -0.0317 & 0.0206 & 0 \end{bmatrix} \begin{bmatrix} \Delta z_m \\ \Delta \theta_m \\ \Delta u_m \\ \Delta q_m \\ \Delta w_m \\ \Delta v_m \\ \Delta r_m \\ \Delta \psi_m \end{bmatrix} + S_{22} \Delta \underline{u}_m
$$

$$
\begin{bmatrix} \Delta N^*_l \\ \Delta \delta^*_s \\ \Delta \theta^*_j \\ \Delta \delta^*_{pj} \\ \Delta \delta^*_a \\ \Delta \delta^*_{rj} \\ \Delta \delta^*_r \\ \Delta \delta^*_{yj} \end{bmatrix} = \begin{bmatrix} 0 & -0.0769 & 0.0611 & 0 \\ 0 & -0.0186 & 0.0483 & 0 \\ 0 & -0.121 & 0.0413 & 0 \\ 0 & -0.0725 & -0.0442 & 0 \\ 0 & -0.00122 & 0.289 & 0 \\ 0 & \sim 0 & -0.837 & 0 \\ 0 & -0.00127 & 0.069 & 0 \\ 0 & \sim 0 & 0.292 & 0 \end{bmatrix} \begin{bmatrix} \Delta z_m \\ \Delta V_{DR,m} \\ \Delta \beta_m \\ \Delta \psi_m \end{bmatrix} + S_{22} \Delta \underline{u}_m
$$

elements in S_{11} and S_{21} while the ramp/step model requires
only 18 nonzero elements to perform the same function. Further
comparisons between the two command generators are presented
in Section 3.3.3.

3.2.3   Low Speed Flight

The most difficult regime to control the AV-8A is
near hover where precise control is needed to land the air-
craft. Two command generators are used for low speed flight;
a velocity ramp/step model and an attitude ramp/step model.

58

Both command systems require precise position information which is usually available from a radar system in the terminal area. The velocity ramp/step model uses the pilot's local-level velocity commands to formulate a desirable position trajectory in inertial space which the aircraft tracks. Any lateral drift is compensated for by rolling the aircraft. Many V/STOL pilots do not care to roll the aircraft near hover since this reduces the jet thrust supporting the aircraft. Further difficulty in roll control is caused by the ground effect (see Appendix C) which destabilizes roll as the aircraft approaches the ground.

The attitude command replaces the cross-range velocity pilot command with a direct roll angle command. By fixing the pitch and roll commands, the pilot maintains a level platform at the cost of lateral drift. The attitude and velocity command systems are designed at 5.15 m/s (10 kt) using the three reaction jets, nozzle angle, and RPM to uniquely accommodate the five commands. Analysis of AV-8A models at speeds lower than 10 kts indicated the data set did not give results which agreed with low speed Harrier behavior (i.e., a highly unstable transmission zero developed in the lateral dynamics).

3.3   V/STOL DIGITAL FLIGHT CONTROL SYSTEM RESULTS

3.3.1   Control Design Procedures

The design procedure for the linear-optimal CGT-PI design involves iterating on the elements in the continuous-time cost function weighting matrices until the system responses and control motions have desirable transients. In addition, closed-loop mapped discrete-time eigenvalues should be located in desirable regions in the left-half complex

plane.   The elements in Q and R are specified as the inverse
of a maximum mean-square value as

$$Q \cong \begin{bmatrix} \dfrac{1}{\Delta x_{max}^2} I & 0 \\ 0 & \dfrac{1}{\Delta u_{max}^2} I \end{bmatrix} + \begin{bmatrix} F^T \\ G^T \end{bmatrix} \dfrac{1}{\Delta \dot{x}_{max}^2} I \quad [F \; G]$$

$$+ \begin{bmatrix} H^T \\ D^T \end{bmatrix} \dfrac{1}{\Delta y_{max}^2} I \quad [H \; D]$$

$$R = \begin{bmatrix} \dfrac{1}{\Delta \dot{u}_{max}^2} I \end{bmatrix}$$

Q is positive definite with cross weighting between states and
controls, caused primarily by acceleration weights, while R is
diagonal and also positive definite.

Experience has shown that one convenient method for
choosing Q and R is to specify Δu_{max} and $\Delta \dot{u}_{max}$ as fractions of
maximum control positions and rates, then perform all further
iterations on Δx_{max}, $\Delta \dot{x}_{max}$, and Δy_{max}.   Each command response
and each eigenvalue is primarily affected by a few of the
remaining state weights which can be selectively adjusted.
The closed-loop eigenvectors are calculated to observe which
states are predominate in a given eigenvalue.   The last fea-
ture has a significant effect on the presentation format of
the closed-loop eigenvalues for the AV-8A. Typical aircraft
have readily identifiable modes such as short period, Dutch
roll, spiral, etc.   The AV-8A does not always exhibit such

60

behavior, and rather than create new names, the eigenvalues will be identified by the state(s) most predominate in the associated eigenvector.

The Q and R matrices at the four design flight conditions are shown in Table 9. The weightings remain almost constant except at low speed flight where the most aerodynamic variation occurs. MIL-F-83300, the flying qualities specification for piloted V/STOL aircraft, Ref. 15, is used as an aid in choosing Q and R. The CGT-PI design employs full state feedback without considering the effect of estimators, hence the closed-loop eigenvalue specifications are easily met for Level 1, Category A and C flight[*]. The parts of MIL-F-83300 that deal with control power and V/STOL response proved to be more useful in the eigenvalue/eigenvector placement design procedure and the choice of the coordinated turn dynamic model shown in Appendix B.

The sampling rate chosen for the AV-8A is 10 frames per second. A number of investigations, such as Refs. 19, 26, and 35, have shown that direct digital designs can use low sample rates without degrading system performance. Reference 35, in particular, shows that for aircraft systems, 10 frames per second seems to be the break point between adequate and poor performance. The digital design for a helicopter in Ref. 26 was successfully flight tested using 10 frames per second with a control law very similiar to the CGT-PI. The

---

*Control design without considering estimator effects is partially justified by the separation theorem but recent results in Ref. 34 indicates that there may not be key guaranteed gain and phase margins using optimal control when estimators are employed. A useful area of future research would be to compute CGT-PI gain and phase margins with estimator effects.

TABLE 9
CGT-PI WEIGHTS AT DESIGN POINTS

T-2906

COST FUNCTION WEIGHTING MATRIX ELEMENTS		MAXIMUM MEAN VALUE FLIGHT CONDITIONS			
		87.5 m/s	51.5 m/s	18.0 m/s	5.15 m/s
Acceleration,	$\Delta\dot{u}$	-	-	-	4.57(15)
	$\Delta\dot{v}$ m/s^2(fps^2)	1.52(5)	1.22(4)	1.22(4)	1.22(4)
	$\Delta\dot{w}$	2.13(7)	2.13(7)	2.13(7)	1.82(6)
Body Velocity,	Δu	-	2.74(9)	2.74(9)	-
	Δv m/s (fps)	-	4.57(15)	2.74(9)	-
	Δw	-	-	-	-
Local-Level Velocity,	ΔV_{DR}	2.74(9)	-	2.74(9)	2.44(8)
	ΔV_{CR} m/s (fps)	2.74(9)	-	2.74(9)	2.44(8)
	ΔV_z	2.74(9)	2.74(9)	2.74(9)	2.44(8)
Body Angular Rate,	Δp	7	7	7	15
	Δq deg/sec	20	20	20	12
	Δr	7	7	7	5
Euler Angles,	$\Delta\phi$	2	2	2	5
	$\Delta\theta$ deg	3	2	3	3
	$\Delta\psi$	-	2	2	5
Control Position,	ΔN_1 %	13.125	13.125	13.125	13.125
	$\Delta\delta_s$ deg	5.325	5.325	5.325	-
	$\Delta\theta_j$ deg	24.625	24.625	24.625	24.625
	$\Delta\delta_{pj}$ cm^2 (in^2)	-	16.8(2.6)	16.8(2.6)	16.8(2.6)
	$\Delta\delta_a$ deg	6.0	6.0	6.0	-
	$\Delta\delta_{rj}$ cm^2 (in^2)	-	6.77(1.05)	6.77(1.05)	6.77(1.05)
	$\Delta\delta_r$ deg	7.5	7.5	7.5	-
	$\Delta\delta_{yj}$ cm^2 (in^2)	11.3(1.75)	11.3(1.75)	11.3(1.75)	11.3(1.75)
Control Rate,	$\Delta\dot{N}_1$ %/sec	3	3	3	3
	$\Delta\dot{\delta}_s$ deg/sec	2	2	2	-
	$\Delta\dot{\theta}_j$ deg/sec	3	3	3	3
	$\Delta\dot{\delta}_{pj}$ cm^2/sec (in^2/sec)	-	19.4(3)	19.4(3)	19.4(3)
	$\Delta\dot{\delta}_a$ deg/sec	2	2	2	-
	$\Delta\dot{\delta}_{rj}$ cm^2/sec (in^2/sec)	-	19.4(3)	19.4(3)	19.4(3)
	$\Delta\dot{\delta}_r$ deg/sec	2	2	2	-
	$\Delta\dot{\delta}_{yj}$ cm^2/sec (in^2/sec)	19.4(3)	19.4(3)	19.4(3)	19.4(3)

complex PIF control law in Ref. 26 required 60% of a computation frame to perform all control calculations indicating that onboard CGT-PI computations can be done within a computation frame if it operates at 10 frames per second.

3.3.2 High Speed Flight

Vectored thrust, $\Delta\theta_j$, and reaction control, $\Delta\delta_{yj}$, are the two unusual features used with the ACM command model in high speed flight. The reaction control is expected to improve sideslip response while vectored thrust will improve normal acceleration response with minimal angle of attack changes. A complication occurs when using vectored thrust because θ_j is at the position limit ($\theta_j=0°$) for straight and level flight. This section discusses how CGT-PI effectively accommodates the high speed design complexities.

The open-loop and mapped closed-loop eigenvalues for the AV-8A at high speed is shown in Table 10. Spiral and a Δq mode are open-loop unstable and interact with the integrator compensator states to form stable closed-loop complex pairs. The primary effect of using the yaw nozzle is to further stablize the sideslip mode (Δv) as expected. Figure 30 shows the effect of the reduced Δv time constant for a $\Delta p_{w,m}$ step command. Comparing the control responses in Figs. 30c and d, the CGT-PI control law hardly changes aileron authority while transferring rudder authority to the yaw nozzle. Note that in Fig. 30c, where the controls and commands are equal, the controls have an initial transient which optimally transfers the system states to the new * trajectory by locking on to the control * trajectories. In Fig. 30d there is extra freedom caused by the extra reaction jet control and the controls do not necessarily lock on to the control * trajectory indicated by the pseudoinverse method for finding the feedforward matrices. The states, however, always lock on to the * trajectory.

63

TABLE 10

EFFECTS OF CGT-PI ON THE DYNAMIC MODES AT 87.5 m/s (170 kt)

T-2907

DYNAMIC MODE	OPEN-LOOP CHARACTERISTICS			CLOSED-LOOP WITHOUT YAW NOZZLE ($\Delta\delta_s$=2.0, $\Delta\delta_{\theta j}$=3.0)			CLOSED-LOOP WITH YAW NOZZLE ($\Delta\delta_s$=3.0, $\Delta\delta_{\theta j}$=1.0)		
	NATURAL FREQUENCY, rad/sec	DAMPING RATIO	TIME CONSTANT, sec	NATURAL FREQUENCY, rad/sec	DAMPING RATIO	TIME CONSTANT, sec	NATURAL FREQUENCY, rad/sec	DAMPING RATIO	TIME CONSTANT, sec
$\int\Delta\beta-\int\Delta p_w$	-	-	-	2.33	0.596	-	2.55	0.637	-
$\Delta\theta-\Delta q$	-	-	-	1.44	0.597	-	0.99	0.764	-
$\Delta r-\Delta\phi$	2.47	0.252	-	2.76	0.363	-	3.08	0.370	-
$\Delta u-\int\Delta V$	-	-	-	0.333	0.837	-	0.333	0.839	-
Δw	-	-	0.348	-	-	0.239	-	-	0.366
ROLL MODE	-	-	0.970	-	-	0.408	-	-	0.387
$\int\Delta\sigma$	-	-	-	-	-	0.602	1.81	0.91	-
$\int\Delta\gamma$	-	-	-	-	-	0.854			-
Δv	-	-	-	-	-	2.42	-	-	0.779
SPIRAL	-	-	-0.372	-	-	-	-	-	-
PHUGOID	0.199	0.481	-	-	-	-	-	-	-
Δq	-	-	-0.767	-	-	-	-	-	-

Any mismatch in one control such as $\Delta\delta_r$ in Fig. 30d must be compensated for by a (barely perceptible) mismatch in another control, $\Delta\delta_{yj}$ in Fig. 30d. The control trajectory freedom in the pseudoinverse design is a characteristic of CGT-PI (but not a characteristic of the Type 0 CGT, as shown in Ref. 10) and no disadvantage with the method has been encountered even in the full nonlinear evaluation, performed in Ref. 14, for a fighter aircraft. In fact, many advantages are available especially when the extra controls favorably saturate for maximum performance when large commands are requested, as discussed in Ref. 13.

Recall from Fig. 28 that CGT-PI handles saturation by leaving the control at the boundary and stabilizes the vehicle using the remaining unsaturated controls. Figure 31 shows the state and control responses for the longitudinal commands with
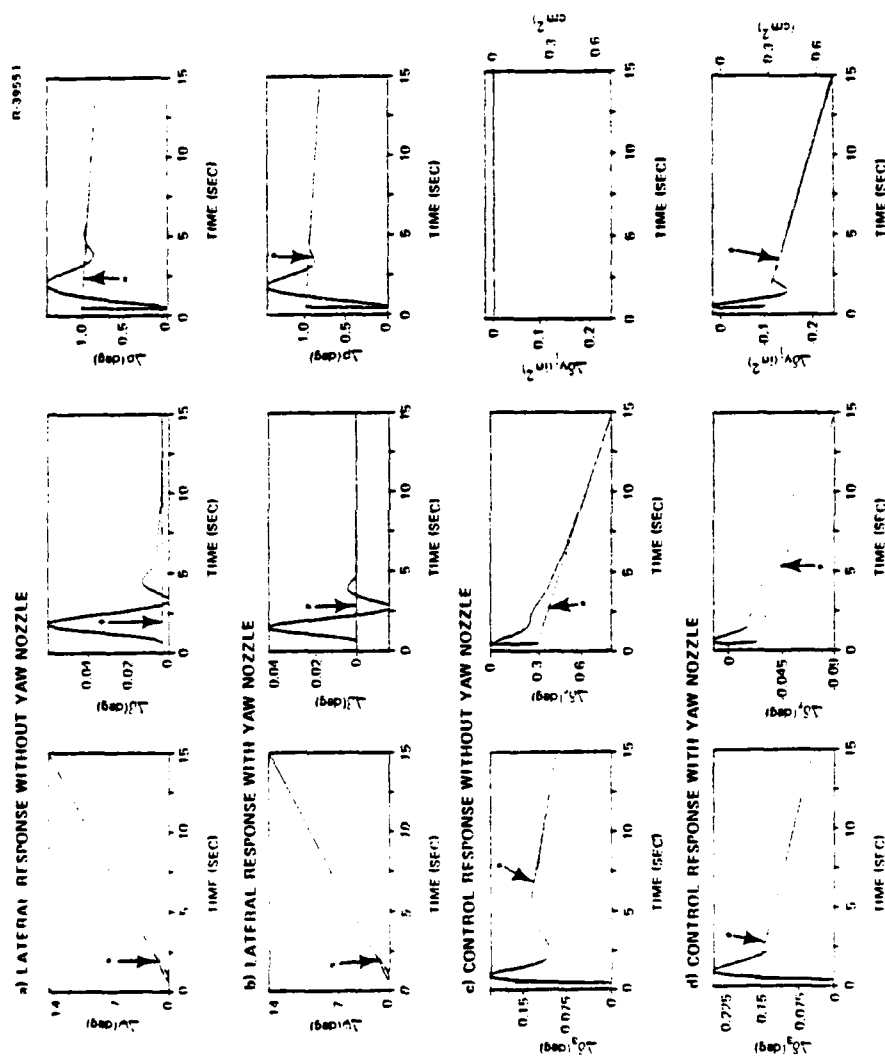
Figure 30   Comparison of Directional Response With and
Without Yaw Nozzle ($\Delta\delta_{y,j}$) at 87.5 m/s (170 kt)

a) INDIVIDUAL STATE RESPONSE TO A STEP IN AN ELEMENT IN Δy_m

b) CONTROL RESPONSE FOR A Δy RAMP COMMAND

c) CONTROL RESPONSE FOR A $\Delta\theta$ STEP COMMAND
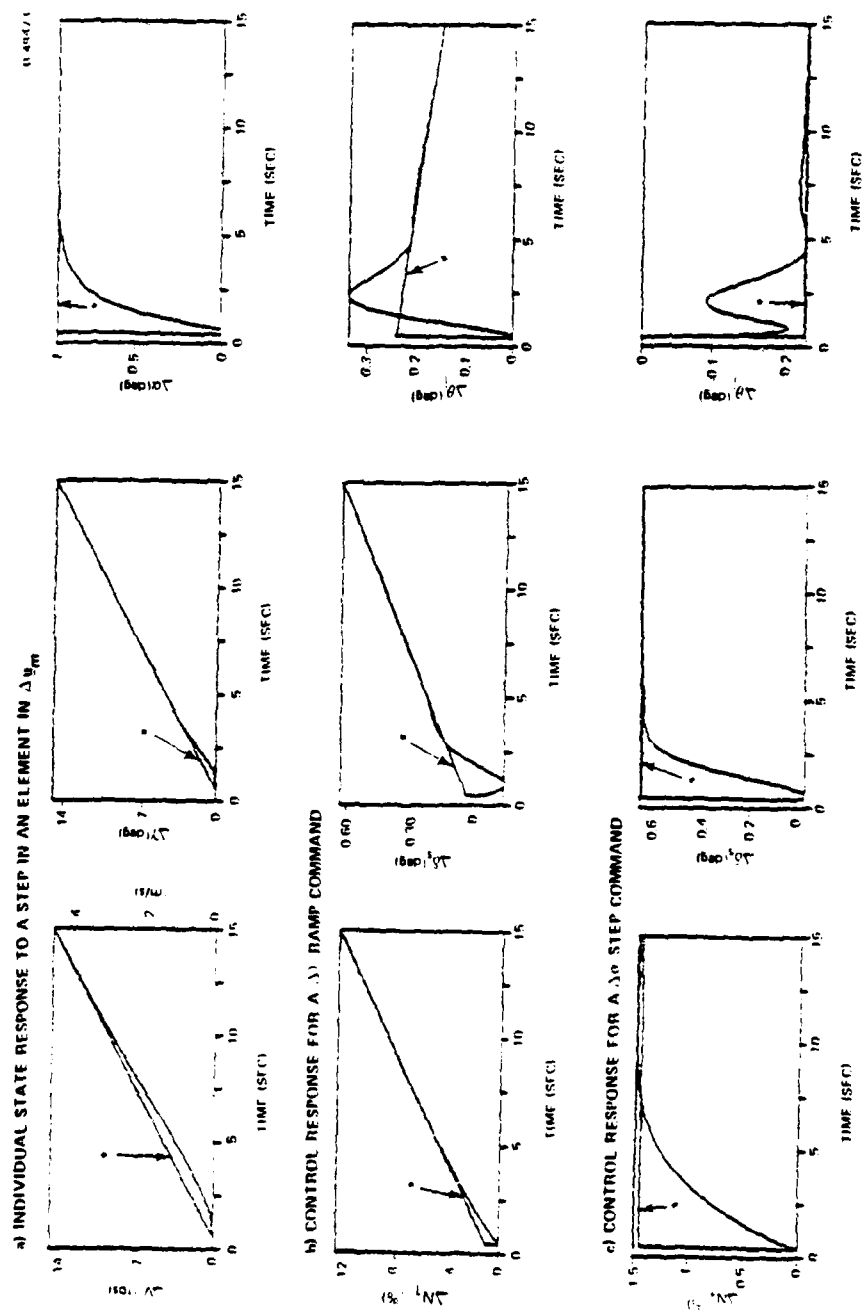
Figure 31   Longitudinal Command Response at 87.5 m/s (170 kt) With Nozzle Angle ($\Delta\delta_{\theta_j}$) Unlimited

66

unlimited $\Delta\theta_j$ movement which are adequate except that $\Delta\theta_j$ moves beyond its limits when a positive $\Delta\alpha$ is commanded. The state feedback gain for the CGT-PI which corresponds to the closed-loop eigenvalues in the middle column of Table 10 is as follows

$$C_1 = \begin{bmatrix} 0.434 & 0.586 & 0.075 & 0.0032 & {\sim}0 & {\sim}0 & {\sim}0 & {\sim}0 \\ -0.611 & 0.124 & -0.439 & -0.106 & {\sim}0 & {\sim}0 & {\sim}0 & {\sim}0 \\ 0.006 & 0.061 & -0.235 & -0.211 & {\sim}0 & {\sim}0 & {\sim}0 & {\sim}0 \\ {\sim}0 & {\sim}0 & {\sim}0 & {\sim}0 & 0.454 & -0.317 & 0.343 & 0.961 \\ {\sim}0 & {\sim}0 & {\sim}0 & {\sim}0 & 0.209 & -0.725 & 0.0732 & -0.024 \end{bmatrix}$$

The ordering of the states and controls is the same as in Table 8. The control, $\Delta\theta_j$, plays an important roll in stabilizing the vehicle with sizable pitch rate feedback, -0.235, and the largest Δw feedback gain, -0.211. The importance of $\Delta\theta_j$ in stability, but not in command response, can be down played by increasing the control's rate weighting. The state feedback gain, caused by decreasing $\Delta\dot{\theta}_{j,max}$, which corresponds to the closed-loop eigenvalues in the last column of Table 10 is

$$C_1 = \begin{bmatrix} 0.418 & 0.584 & 0.0644 & 0.00125 & {\sim}0 & -0.0333 & {\sim}0 & {\sim}0 \\ -0.819 & 0.167 & -0.586 & -0.190 & {\sim}0 & {\sim}0 & {\sim}0 & {\sim}0 \\ 0.209 & 0.00446 & -0.0227 & -0.0690 & {\sim}0 & {\sim}0 & {\sim}0 & {\sim}0 \\ {\sim}0 & {\sim}0 & {\sim}0 & {\sim}0 & 0.253 & -0.0512 & 0.277 & 0.860 \\ 0.0392 & 0.0563 & {\sim}0 & {\sim}0 & 0.0761 & -0.108 & 0.0506 & 0.108 \\ -0.0442 & -0.0596 & {\sim}0 & {\sim}0 & 0.418 & -0.783 & 0.161 & 0.266 \end{bmatrix} \tag{6}$$

Without substantially changing the closed-loop longitudinal eigenvalues the Δq-$\Delta\theta_j$ and Δw-$\Delta\theta_j$ gains have been reduced by almost an order of magnitude. When the longitudinal ACM commands are repeated in Fig. 32 with $\Delta\theta_j$ position limited using the feedback gain in Eq. 6, the aircraft remains stable, ΔV and Δy commands are accommodated, but the aircraft cannot significantly maintain an increased command in angle of attack

while holding ΔV and $\Delta\theta_j$ constant. The importance of vectored thrust is to reduce angle of attack variations when large normal acceleration commands are requested and CGT-PI performs this feature very well for a $\Delta a_{n,m}/V_o$ command of 1 sec^{-1} which produces the $\Delta\gamma$ ramp in Fig. 32a and the control responses in Fig. 32b. The maximum angle of attack variation before $\Delta\alpha$ returns to its commanded value of 0.0 is 0.1 deg when $\Delta a_{n,m}$ is commanded. In flight, the angle of attack ACM command could be preprogrammed depending on forward velocity to avoid θ_j commands beyond saturation (with pilot override available but usually not used).

3.3.3 Transition

This section presents design results for the two transition flight conditions, 51.5 m/s (100 kt) and 18.0 m/s (35 kt). Transition is characterized as a shift from the aerodynamic control surfaces to the reaction jets for stability and control. Two features are expected to occur during transition; the feedforward gain elements and the feedback gains for $\Delta\delta_s$, $\Delta\delta_a$, and $\Delta\delta_r$ should decrease with forward velocity.

The feedforward matrix S_{22} is shown in the following equations using the enroute velocity command model for 51.5 m/s (100 kt) and 18.0 m/s (35 kt), respectively.

$$
\begin{bmatrix}
\Delta N_1^* \\
\Delta\delta_s^* \\
\Delta\theta_j^* \\
\Delta\delta_{pi}^* \\
\Delta\delta_a^* \\
\Delta\delta_{rj}^* \\
\Delta\delta_r^* \\
\Delta\delta_{vj}^*
\end{bmatrix}
= S_{21}\Delta\underline{x}_m +
\begin{bmatrix}
-0.338 & -0.858 & 0.243 & 0.0141 & -0.00506 \\
-0.0662 & -0.402 & -0.368 & 0.0136 & -0.00665 \\
-0.171 & -1.53 & -1.84 & 0.0134 & -0.00766 \\
-0.128 & -0.529 & -0.275 & -0.0127 & 0.00639 \\
\sim 0 & -0.0222 & -0.0392 & 0.102 & -0.0478 \\
\sim 0 & -0.00838 & -0.0133 & -0.256 & 0.138 \\
-0.00701 & -0.0171 & 0.00626 & 0.0470 & -0.00891 \\
\sim 0 & 0.00126 & -0.00107 & 0.0713 & -0.0283
\end{bmatrix}
\begin{bmatrix}
\Delta a_{DR,m} \\
\Delta V_{z,m} \\
\Delta\theta_m \\
\Delta a_{CR,m} \\
\Delta\dot\psi_m
\end{bmatrix}
$$
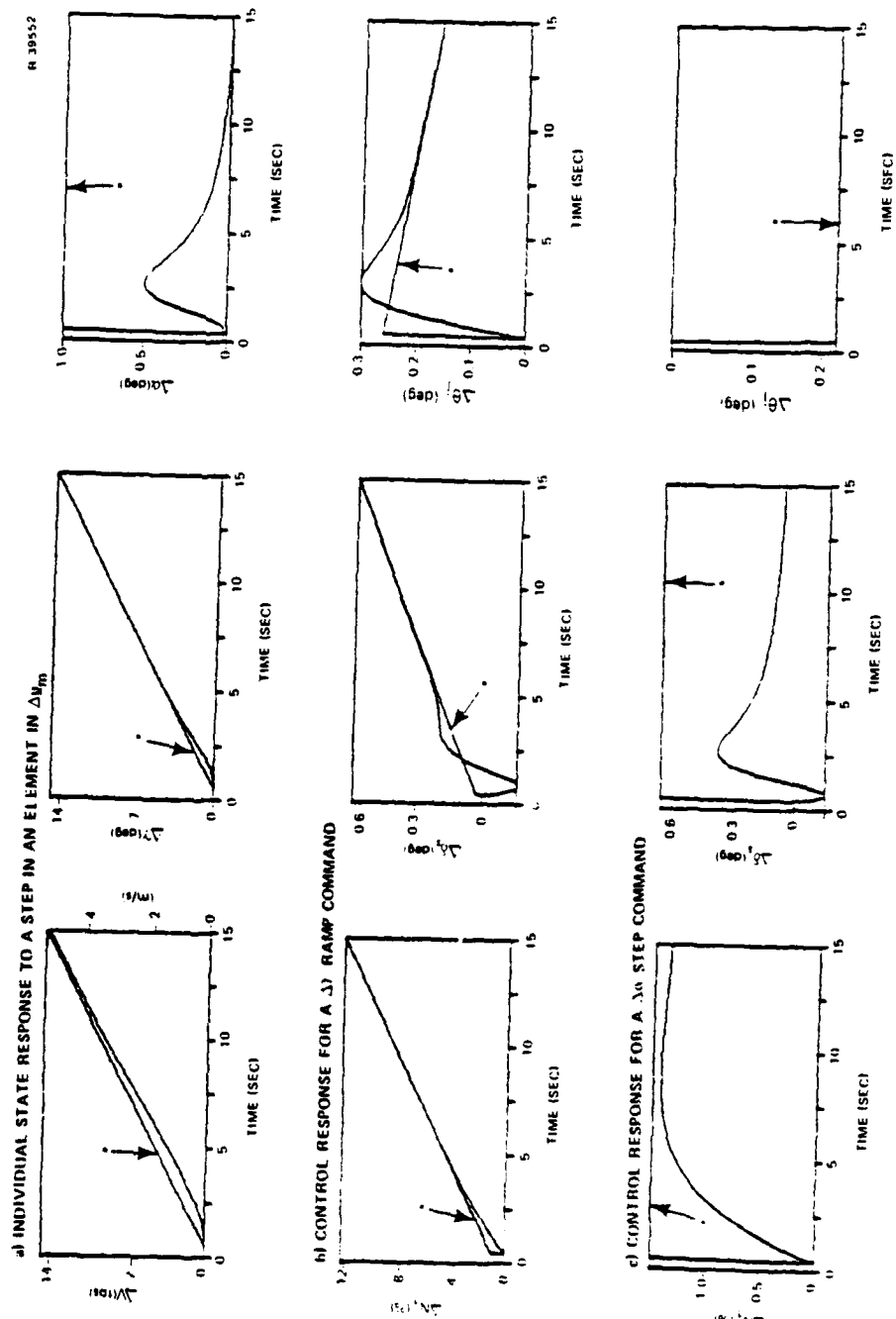
Figure 32　Longitudinal Command Response at 87.5 m/s (170 kt)
With Nozzle Angle ($\Delta \delta_{\theta j}$) Position Limited

69

$$
\begin{bmatrix} \Delta N_1^* \\ \Delta\delta_s^* \\ \Delta\theta_j^* \\ \Delta\delta_{pj}^* \\ \Delta\delta_a^* \\ \Delta\delta_{rj}^* \\ \Delta\delta_r^* \\ \Delta\delta_{yj}^* \end{bmatrix} = S_{21}\Delta x_{-m} + \begin{bmatrix} -0.121 & -0.135 & -0.0196 & \sim 0 & -0.00263 \\ \sim 0 & -0.00156 & -0.00356 & \sim 0 & \sim 0 \\ -0.0252 & -1.02 & -1.77 & \sim 0 & \sim 0 \\ -0.0609 & -0.122 & -0.0964 & -0.00102 & 0.00222 \\ \sim 0 & -0.00113 & -0.00231 & 0.00195 & \sim 0 \\ \sim 0 & \sim 0 & \sim 0 & -0.0161 & 0.0204 \\ \sim 0 & \sim 0 & \sim 0 & 0.00277 & \sim 0 \\ \sim 0 & \sim 0 & \sim 0 & -0.00198 & -0.0131 \end{bmatrix} \begin{bmatrix} \Delta a_{DR,m} \\ \Delta V_{z,m} \\ \Delta\theta_m \\ \Delta a_{CR,m} \\ \Delta\dot\psi_m \end{bmatrix}
$$

The elements for $\Delta\delta_s^*$, $\Delta\delta_a^*$, and $\Delta\delta_r^*$ decrease by an order of magnitude as expected. Similarly, the feedback gains decrease as shown in Fig. 33 using the $\Delta\phi$ to $\Delta\delta_a$ gain and the Δq to $\Delta\delta_s$ gain as typical examples. Although only four points are plotted for each gain shown in Fig. 33, indications are that the AV-8A gains have easily scheduled smooth variations with flight condition. The CGT-PI designs should readily convert to gain-scheduled nonlinear control laws using the same technique as in Ref. 26.

The closed-loop mapped eigenvalues for CGT-PI in transition flight are shown in Tables 11 and 12. The open-loop characteristics have unstable complex pairs in both the longitudinal and lateral modes. The feedback gains stabilize all modes, cause the complex pairs to have damping ratios greater than 0.5, and rearranges the eigenvectors. It should be kept in mind that the identification of states with eigenvalues is an eigenvector simplification useful in choosing Q and R. For example, $\Delta\phi$ has contributions from almost all the lateral-directional modes; identifying $\Delta\phi$ with Δr in a complex pair is obtained by a process of elimination rather than a recognized predominate involvement. As the forward velocity decreases (Table 11 to Table 12), the decreased aerodynamic effects

70
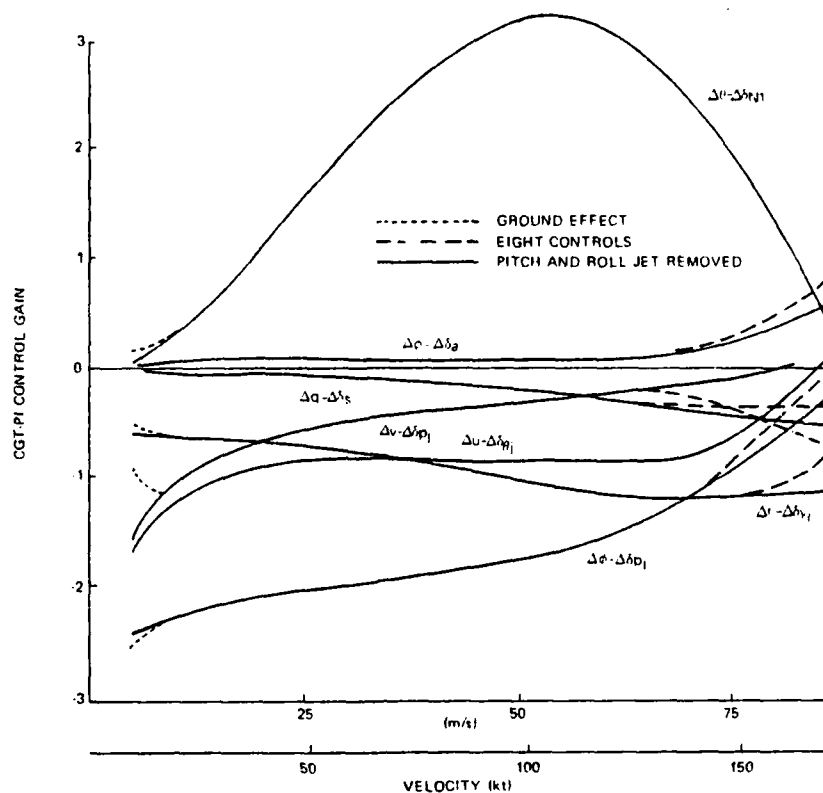
Figure 33   Feedback Gain Variations With Forward Velocity

TABLE 11

EFFECTS OF CGT-PI IN TRANSITION FLIGHT
(51.5 m/s (100 kt))

DYNAMIC MODE	OPEN-LOOP CHARACTERISTICS			ALL CONTROLS CLOSED-LOOP CHARACTERISTICS			NO REACTION JETS CLOSED-LOOP CHARACTERISTICS		
	NATURAL FREQUENCY, rad/sec	DAMPING RATIO	TIME CONSTANT, sec	NATURAL FREQUENCY, rad/sec	DAMPING RATIO	TIME CONSTANT, sec	NATURAL FREQUENCY, rad/sec	DAMPING RATIO	TIME CONSTANT, sec
$\int\Delta w$-$\int\Delta\theta$	-	-	-	3.52	0.593	-	2.15	0.234	-
Δq-Δw	-	-	-	2.51	0.717	-	1.61	0.679	-
Δr-$\Delta\theta$	-	-	-	2.31	0.739	-	0.984	0.604	-
Δz-$\int\Delta V_{DR}$	-	-	-	0.649	0.688	-	0.610	0.677	-
Δu-$\int\Delta z$	-	-	-	0.434	0.778	-	0.421	0.792	-
ROLL MODE	-	-	0.695	-	-	0.346	-	-	0.603
Δw	-	-	-	-	-	0.932	-	-	1.01
$\Delta\theta$	-	-	-	-	-	0.966	-	-	1.54
$\int\Delta\theta$	-	-	-	-	-	1.39	-	-	2.79
Δv	-	-	-	-	-	6.28	-	-	6.55
SPIRAL	-	-	21.96	-	-	-	-	-	-
$\Delta\theta$-Δu	0.394	-0.333	-	-	-	-	-	-	-
Δq	-	-	1.02	-	-	-	-	-	-
Δw	-	-	5.03	-	-	-	-	-	-
Δv-Δr	2.03	-0.0817	-	-	-	-	-	-	-

71

TABLE 12

EFFECTS OF CGT-PI IN TRANSITION FLIGHT
(18.0 m/s (35 kt))

DYNAMIC MODE	OPEN-LOOP CHARACTERISTICS			ALL CONTROLS CLOSED-LOOP CHARACTERISTICS		
	NATURAL FREQUENCY, rad/sec	DAMPING RATIO	TIME CONSTANT, sec	NATURAL FREQUENCY, rad/sec	DAMPING RATIO	TIME CONSTANT, sec
$\int\Delta w - \int V_{CR}$	-	-	-	2.69	0.666	-
$\Delta q - \Delta w$	-	-	-	1.91	0.713	-
$\Delta r - \Delta\phi$	-	-	-	1.73	0.633	-
$\Delta z - \int\Delta V_{DR}$	-	-	-	0.706	0.668	-
$\Delta u - \int\Delta z$	-	-	-	0.437	0.761	-
ROLL MODE	-	-	1.29	-	-	0.330
$\Delta\psi$	-	-	-	-	-	0.571
$\Delta\theta$	-	-	-	-	-	0.609
$\int\Delta\theta$	-	-	-	-	-	1.33
Δv	-	-	-	-	-	7.44
SPIRAL	-	-	15.67	-	-	-
$\Delta\theta - \Delta u$	0.351	-0.589	-	-	-	-
Δq	-	-	1.47	-	-	-
Δw	-	-	9.32	-	-	-
$\Delta v - \Delta r$	0.672	-0.314	-	-	-	-

cause the closed-loop poles to move closer to the imaginary axis but with approximately the same damping ratio in the complex pairs. The pseudoinverse CGT-PI design has the same number of closed-loop eigenvalues with and without the reaction jets in transition flight. Removing the reaction jets as shown n Table 11 causes a marked degradation in system closed-loop performance for fixed Q and R.

The most interesting aspect of the transition designs is in comparison between the dynamic and ramp/step models for coordinated turns. Figures 34 and 35 show state and control transients for step pitch angle commands from each type of command generator, while Figs. 36 and 37 show state and control transients for ramp yaw angle commands. The dynamic models used for model following have eigenvalues near the same regions in the complex plane as the closed-loop eigenvalues

72

for CGT-PI. If this is a reasonable design practice (i.e., a poorly damped, slow dynamic model is not a desirable command generator) then dynamic models offer little advantage over ramp/step command generators and, in fact, have a clear disadvantage from an implementation point of view (see Section 3.2.2). The dynamic model causes the aircraft to have desirable transients as the state $\Delta\underline{x}$ tracks $\Delta\underline{x}^*$ as expected, but the $\Delta\underline{x}$ transient for the ramp and step models are just as good. Stable dynamic models for command generator tracking have been researched starting from Ref. 17 but it is only recently, Refs. 11 and 12, that theory has become available for designing ramp and unstable command generator trackers using optimal control.

The last two simulation results for transition flight show the five command responses for 18.0 m/s (35 kt) in Fig. 38 using the enroute velocity command model and the effect of putting a square pulse in the vertical velocity command at 51.5 m/s (100 kt) in Fig. 39. The pitch angle and yaw angle response at 18.0 m/s (35 kt) are almost the same as the 51.5 m/s (100 kt) design responses in Figs. 34 and 35 indicating desirable closed-loop uniformity during transition. The square pulse in Fig. 39 demonstrates an important property of the CGT-PI. Even though the design requires the command model input to be constant; the input in implementation can be very time-varying without causing poor transients. If inputs are slowly varying or are changed after the system error is small, the resulting plant control inputs are essentially optimal. In Fig. 39, the pilot control command of 0.305 m/s (1 fps) for $\Delta V_{z,m}$ begins the descent, then just as $\Delta\underline{x}$ approaches $\Delta\underline{x}^*$, the $\Delta V_{z,m}$ is returned to zero. The AV-8A control transients to begin and stop the descent are essentially optimal mirror images of each other.
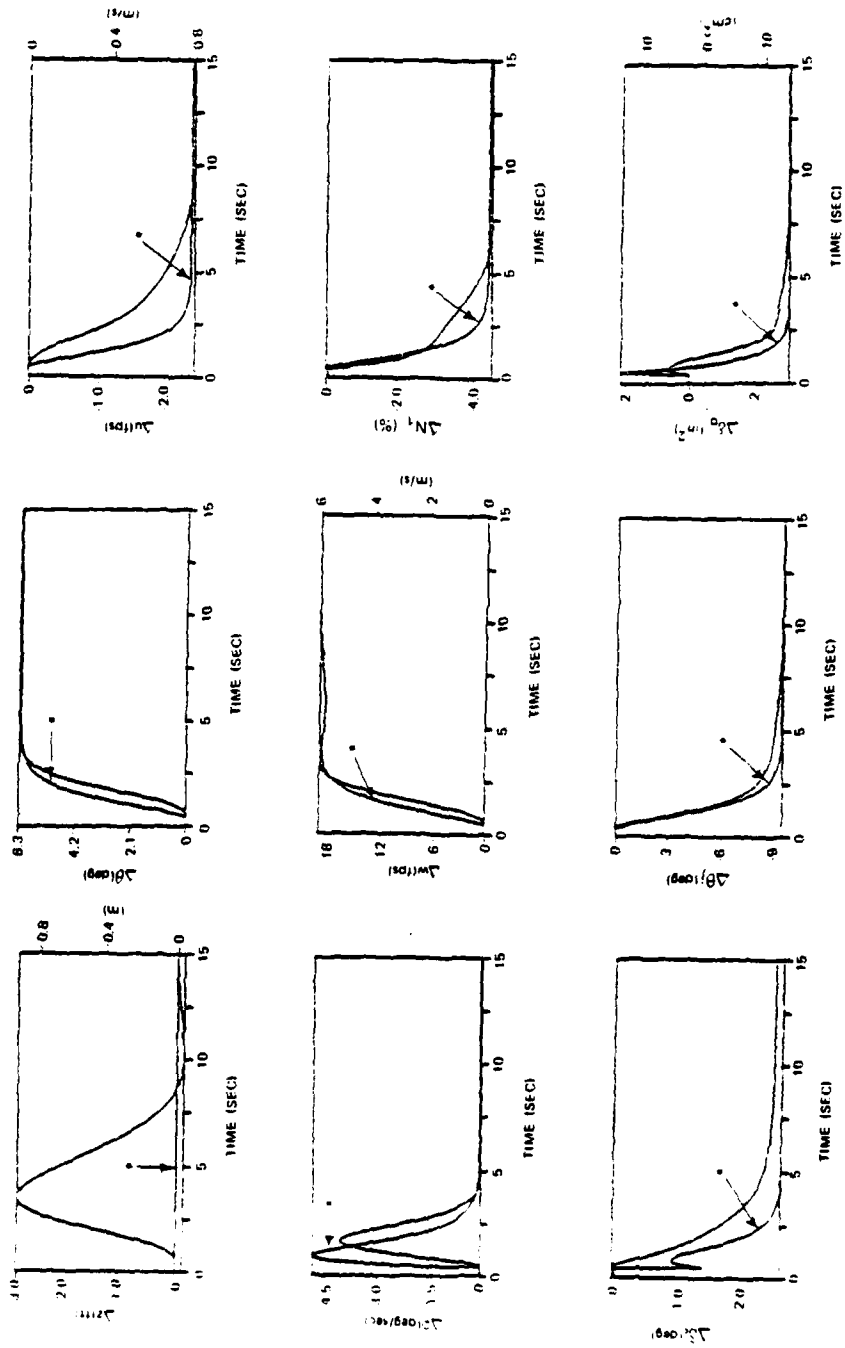
Figure 34   Longitudinal Response for Pitch Angle Model
Following at 51.5 m/s (100 kt)
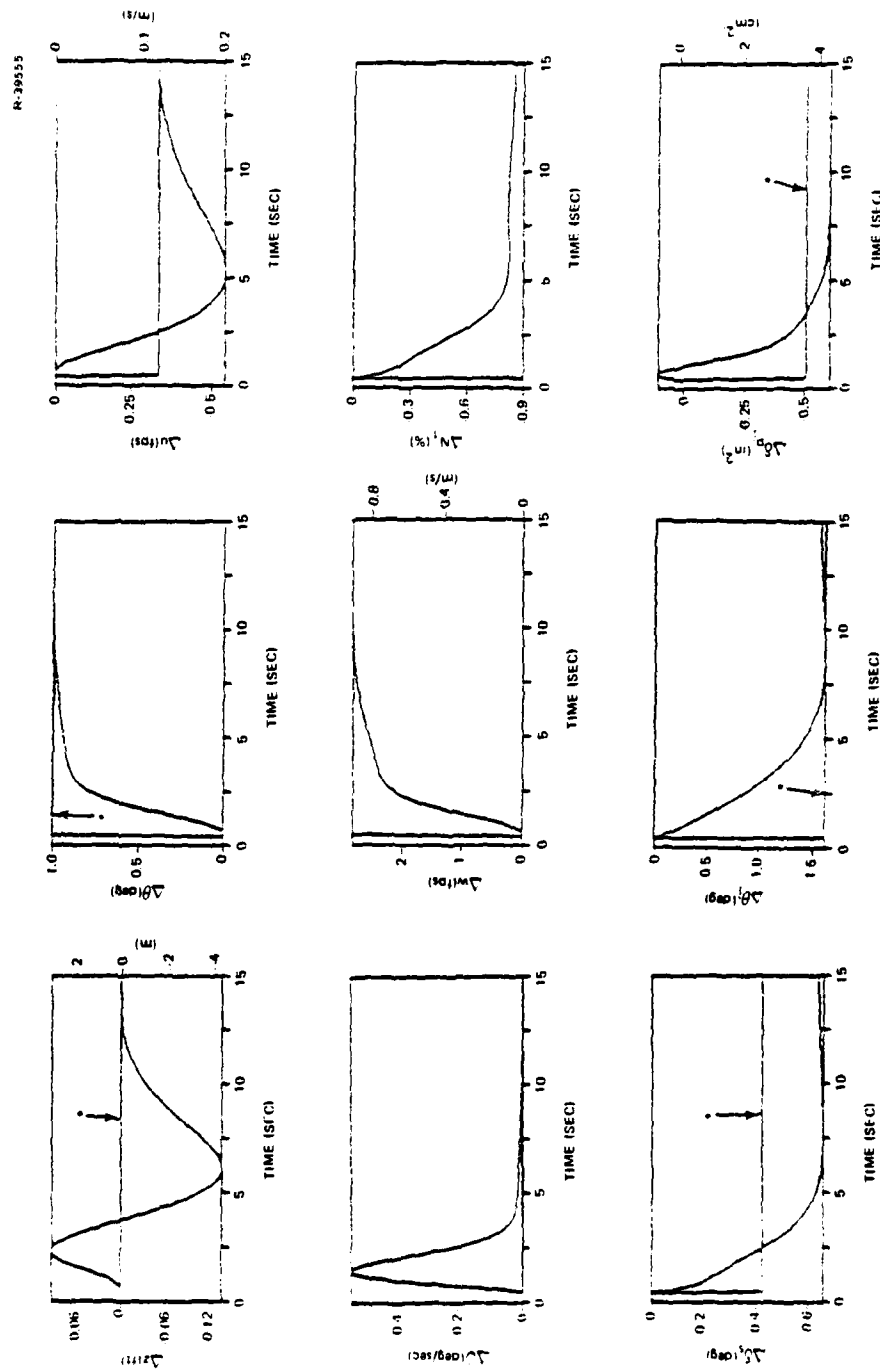
Figure 35   Longitudinal Responses for a Pitch Angle
Step Command at 51.5 m/s (100 kt)
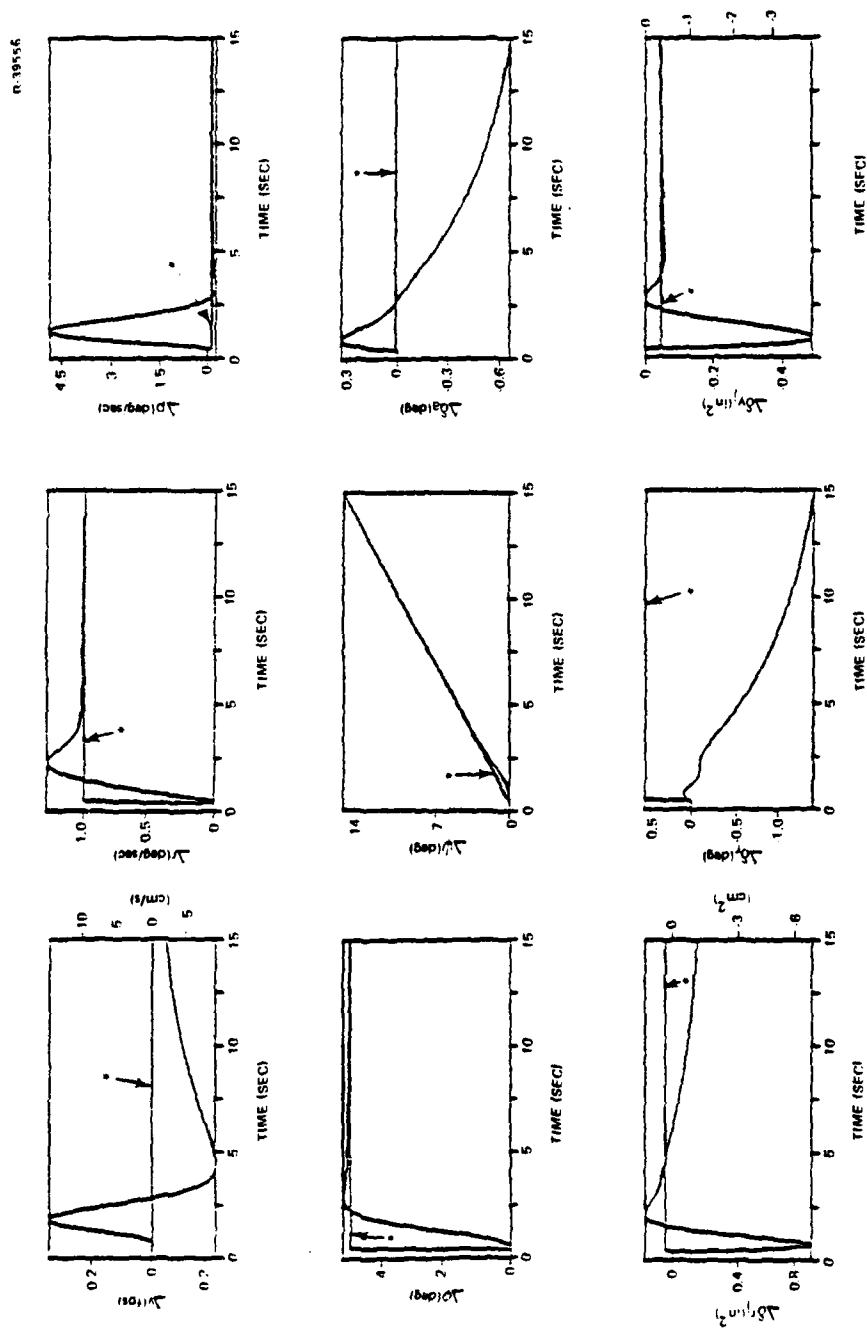
Figure 36   Lateral-Directional Response for Coordinated
Turn Ramp/Step Tracking at 51.5 m/s (100 kt)

76
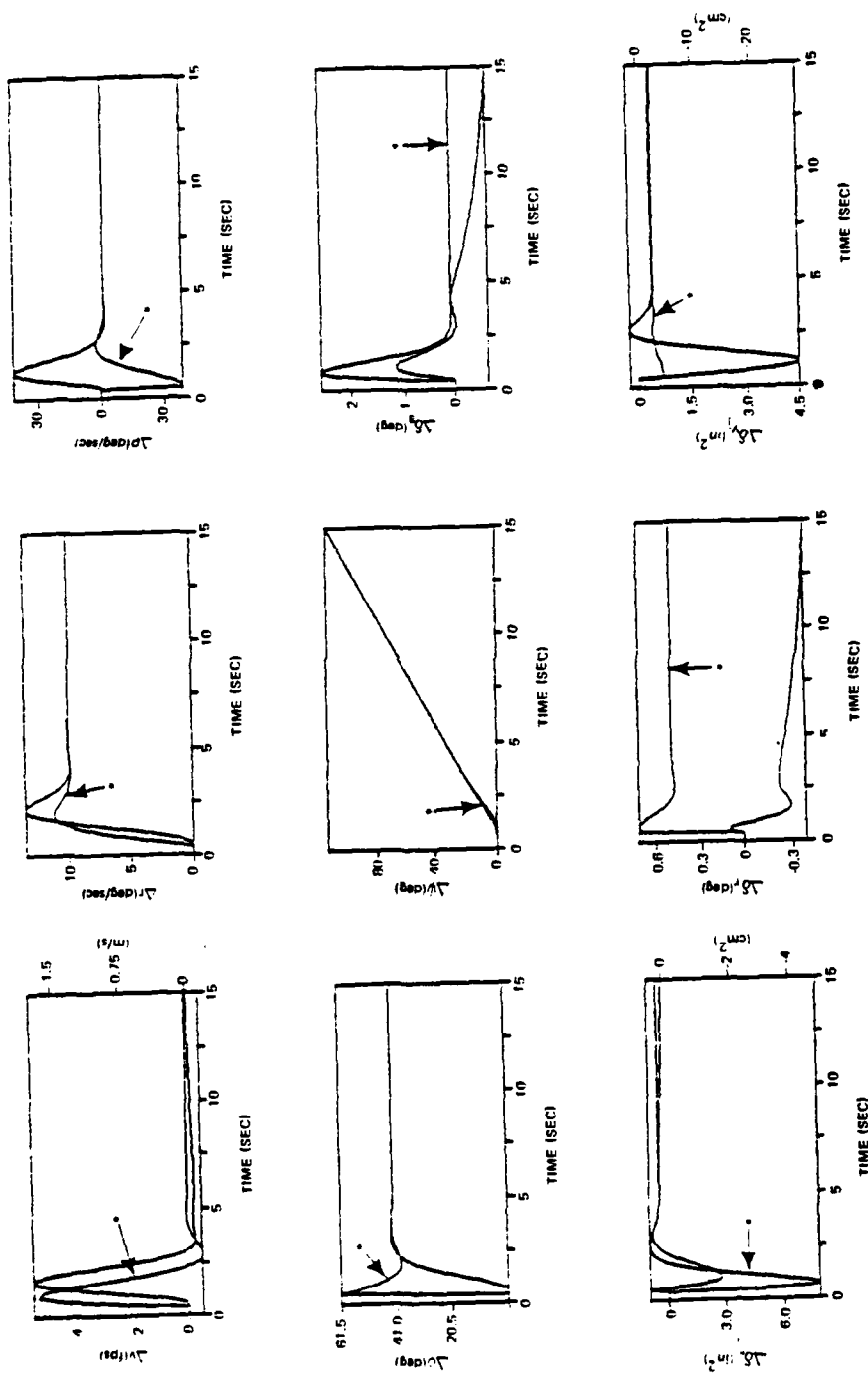
Figure 37   Lateral-Directional Response for Coordinated
Turn Model Following at 51.5 m/s (100 kt)

77
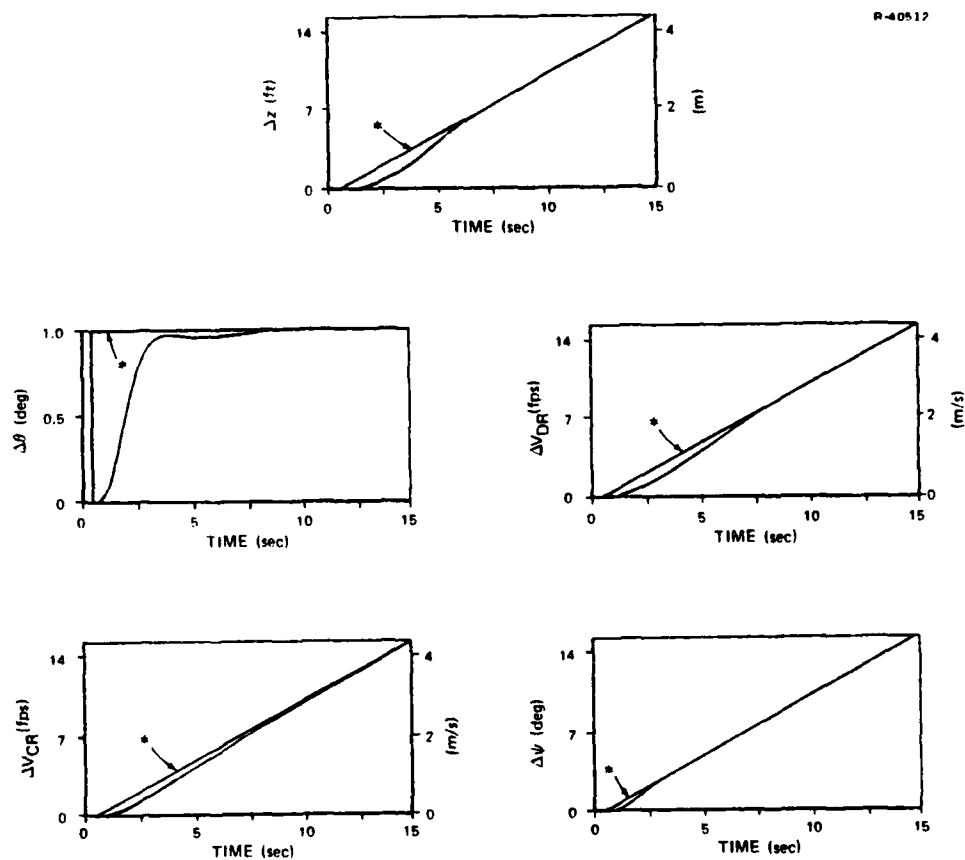
Figure 38   Velocity Command System Responses
at 18.0 m/s (35 kt)
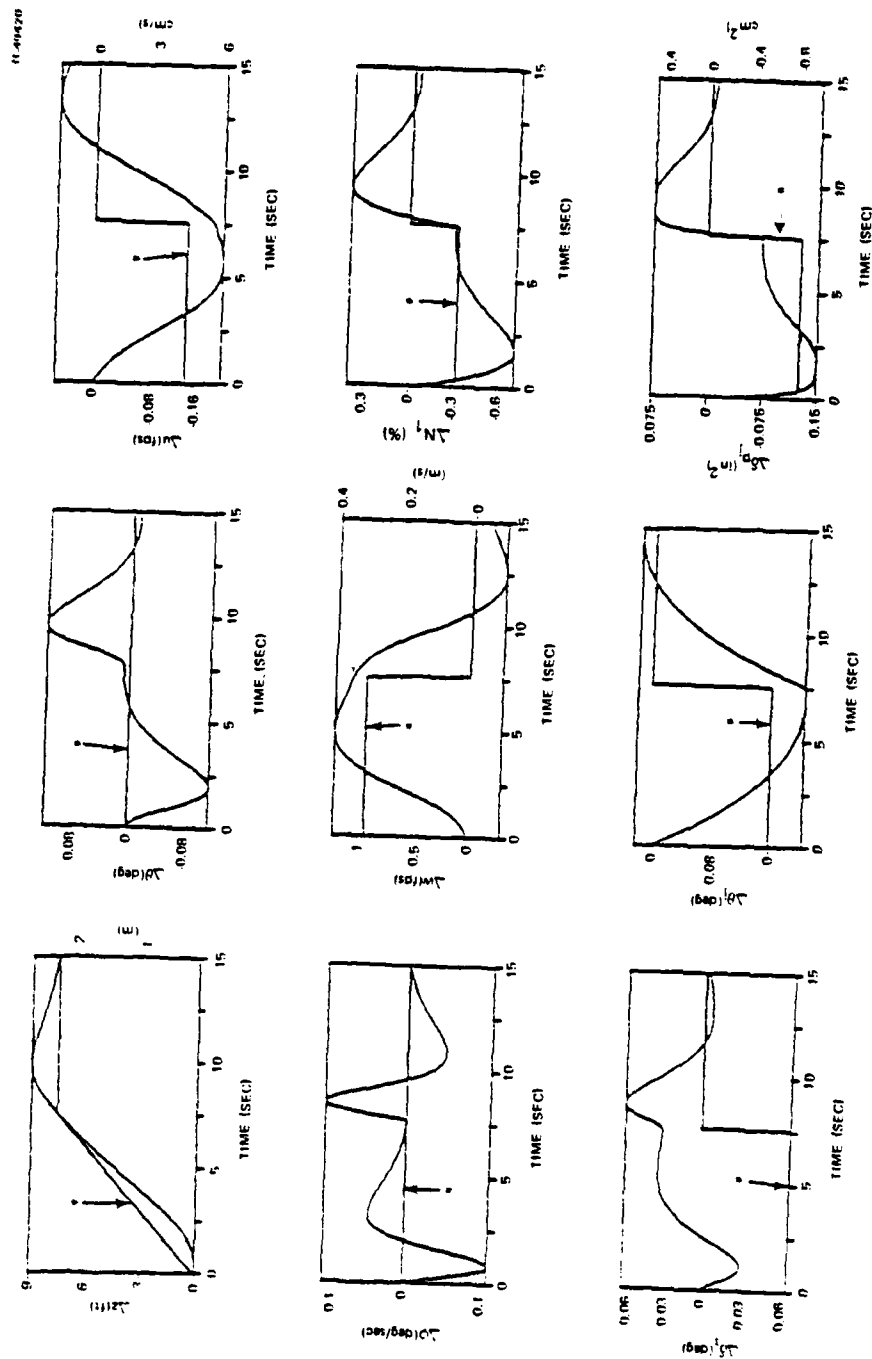
Figure 39 Longitudinal Response for a Vertical Position
Ramp Command at 51.5 m/s (100 kt)

79

3.3.4 Low Speed Flight

The AV-8A in low altitude, low speed flight, as with all V/STOL, is very difficult for a pilot to control and is known to have excessive pilot workload (Ref. 3). All of the design tools developed in Appendices A and B are applied toward relieving pilot workload in low speed flight. This section will compare the attitude and velocity command systems, study the ground effect (Appendix C), and present simulations from optimal control and eigenvalue/eigenvector placement designs.

Table 13 shows the eigenvalue characteristics for the AV-8A with velocity or attitude commands. The only significant difference is that the Δv-Δr (or Dutch roll like) mode in the velocity system splits in the attitude command system to form an almost neutrally stable lateral speed mode associated with Δv. The mode associated with Δr combines with an integrator compensator state to form a complex pair. Any attempt to stablize the Δv mode in the attitude command system degrades the steady state behavior of the $\Delta\phi_m$ command. The difference between velocity and attitude closed-loop eigenvalues is typical behavior and is also reported in Ref. 26 for a helicopter study. Figure 40 compares state responses for velocity and attitude commands. When yaw angle is commanded to be a ramp with the three positions command to zero in the velocity command system, the AV-8A turns over a spot on the ground with a small ramp increase in roll angle as shown in Fig. 40c. When a cross-range velocity command of 0.305 m/s (1 fps) with yaw angle commanded to zero is requested for the velocity command system the most noticeable effect in Fig. 40d is the roll angle peak transient of approximately 1.3 degrees. A (not unreasonable) step crosswind gust disturbance of 5.15 m/s (10 kt) could cause the velocity command system to bank the aircraft near 20 deg in transient to maintain position.

TABLE 13

EFFECTS OF CGT-PI AT LOW SPEED 5.15 m/s (10 kt)

DYNAMIC MODE	OPEN-LOOP CHARACTERISTICS			CLOSED-LOOP CHARACTERISTICS VELOCITY COMMAND			CLOSED-LOOP CHARACTERISTICS ATTITUDE COMMAND		
	NATURAL FREQUENCY, rad/sec	DAMPING RATIO	TIME CONSTANT, sec	NATURAL FREQUENCY, rad/sec	DAMPING RATIO	TIME CONSTANT, sec	NATURAL FREQUENCY, rad/sec	DAMPING RATIO	TIME CONSTANT, sec
$\Delta p - \int \Delta \phi$	-	-	-	2.47	0.641	-	2.82	0.577	-
$\Delta q - \Delta w$	0.292	-0.472	-	1.68	0.569	-	1.68	0.573	-
$\Delta v - \Delta r$	0.125	-0.779	-	1.51	0.571	-	-	-	-
$\Delta x - \int \Delta x$	-	-	-	0.583	0.612	-	0.553	0.624	-
$\Delta z - \int \Delta z$	-	-	-	0.694	0.687	-	0.605	0.704	-
$\Delta y - \int \Delta y$	-	-	-	0.635	0.689	-	-	-	-
$\Delta \theta$	-	-	2.69	-	-	0.555	-	-	0.407
$\Delta \phi$	-	-	-	-	-	0.580	-	-	0.562
$\Delta \psi$	-	-	∞	-	-	0.677	-	-	0.696
$\int \Delta \theta$	-	-	-	-	-	1.34	-	-	1.22
Δu	-	-	26.59	-	-	2.02	-	-	2.18
Δv	-	-	-	-	-	-	-	-	57.7
$\Delta r - \int \Delta \phi$	-	-	-	-	-	-	1.53	0.582	-
$\Delta p - \Delta \phi$	0.210	0.749	-	-	-	-	-	-	-

Figure 40   Comparison of Velocity and Attitude Command
Responses at 5.15 m/s (10 kt)

82

The bank angle transient in the velocity command system can be reduced at the expense of increased lateral drift.

An alternative is to give the pilot full authority in correcting lateral drift using the attitude hold command system with an explicit roll command. Any crosswind causes the aircraft to drift slowly with constant attitude. V/STOL pilots, reported in Refs. 7 and 17, prefer a level attitude in the descent to touchdown and do not actively correct for small lateral drift.

As the V/STOL descends, the vehicle enters the ground effect with subsequent changes in characteristics, particularly in roll. Table 14 shows the closed-loop eigenvalues for the optimal in ground effect (IGE) gains and indicates what happens if the out of ground effect (OGE) gains used in Table 13 are used with the IGE AV-8A model. The lateral-directional mode $\Delta p - \int \Delta \psi$ becomes very lightly damped. A check of the feedback gains in Fig. 33 shows that the $\Delta \phi$ to $\Delta \delta_{rj}$ gain should be considerably reduced when IGE occurs. Both of these observations are in agreement with Ref. 9 where it is demonstrated than pilots should not have tight attitude control IGE or PIO (pilot induced oscillation) occurs in roll. The CGT-PI control law would require special gain adaptation procedures to avoid poor performance as the vehicle descends to touchdown.

The pilot in low speed flight for the AV-8A without command augmentation, has three longitudinal controls; pitch attitude, thrust magnitude, and thrust direction to control vehicle velocity and orientation in the longitudinal axis. The controls require rapid, simultaneous, coordinated activity if the pilot wishes to change altitude without changing pitch angle and speed, and likewise for changing speed without changing altitude and pitch angle. It is recognized (Ref. 3) that a suitably decoupled command augmentation fly-by-wire

TABLE 14

EFFECTS OF GAIN ADAPTATION IN THE GROUND EFFECT AT 5.15 m/s (10 kt) FOR THE VELOCITY COMMAND SYSTEM

T-2911

DYNAMIC MODE	CLOSED-LOOP CHARACTERISTICS ADAPTED IGE GAINS			CLOSED-LOOP CHARACTERISTICS UNADAPTED OGE GAINS		
	NATURAL FREQUENCY, rad/sec	DAMPING RATIO	TIME CONSTANT, sec	NATURAL FREQUENCY, rad/sec	DAMPING RATIO	TIME CONSTANT, sec
$\Delta p - \int \Delta \psi$	2.05	0.89	-	1.89	0.0396	-
$\Delta q - \Delta w$	1.69	0.563	-	1.37	0.621	-
$\Delta v - \Delta r$	1.52	0.577	-	1.54	0.571	-
$\Delta x - \int \Delta x$	0.582	0.612	-	0.588	0.621	-
$\Delta z - \int \Delta z$	0.671	0.728	-	0.610	0.604	-
$\Delta y - \int \Delta y$	0.593	0.682	-	0.482	0.731	-
$\Delta \theta$	-	-	0.561	-	-	0.371
$\Delta \phi$	-	-	0.354	-	-	0.200
$\Delta \psi$	-	-	0.678	-	-	0.685
$\int \Delta \theta$	-	-	1.25	-	-	1.05
Δu	-	-	2.02	-	-	2.02

system is required for VSTOL aircraft to meet control objectives and that display improvements alone will not overcome deficiencies. The direct digital designed eigenvalue/ eigenvector placement CGT-PI is an ideal candidate for meeting these control requirements.

The eigenvalue/eigenvector placement (EEP) model presented in Appendix B.3 decouples forward velocity and altitude response while placing the closed-loop eigenvalues at approximately the same places as the optimal control designed velocity command system. The PI gains for the EEP design are (the ordering of the longitudinal states and controls are shown in Table B-1)

$$C_1 = \begin{bmatrix} 0.0005 & -2.16 & 2.93 & 0.298 & 3.09 & -2.19 \\ -2.18 & 0.112 & 0.737 & -3.31 & -0.186 & -0.308 \\ -0.106 & -0.581 & 1.73 & -0.0696 & 1.39 & -0.594 \end{bmatrix}$$

$$\Delta tC_2 = \begin{bmatrix} 0.00001 & -0.0394 & -0.0656 \\ -0.0456 & -0.00355 & 0.00341 \\ -0.00221 & 0.0312 & -0.0176 \end{bmatrix}$$

while the optimal control gains are

$$C_1 = \begin{bmatrix} 0.0911 & -0.910 & 0.0571 & 0.292 & -0.101 & -1.24 \\ -0.979 & 0.0325 & 0.174 & -1.71 & 0.0198 & -0.181 \\ -0.437 & -0.256 & 1.30 & -0.539 & 0.681 & -0.396 \end{bmatrix}$$

$$\Delta tC_2 = \begin{bmatrix} 0.0024 & -0.0210 & -0.0266 \\ -0.0249 & -0.0174 & 0.000891 \\ -0.0115 & 0.0702 & -0.000127 \end{bmatrix}$$

Optimal control, as expected, has smaller gains (i.e., lower control variances when noise is present) and considerably lower gains for the thrust magnitude control; all desirable features. A comparison of the response of the two designs is shown in Figs. 41 to 43 for the velocity command system. The two low frequency complex pairs associated with position in the optimal control design are replaced by stable real eigenvalues in the EEP system and this reflects into less oscillatory control movements particularly when down-range velocity is commanded in Fig. 43. The comparison of the two designs indicates that the direct digital EEP design has the potential for competing with and complementing optimal control and is an easier method for evolving time domain design objectives into actual control performance. The EEP design simulated in the figures is a first time, one iteration effort that did not take advantage of the considerable design freedom available in the choice of the ideal model.

08773

1.0

2.8   2.5
3.2   2.2
3.6

4.0   2.0

1.1

1.8

1.25   1.4   1.6
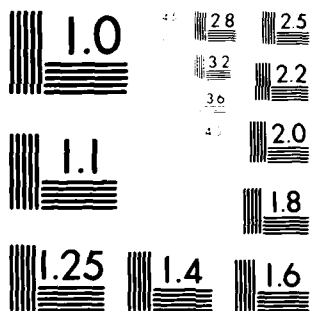
MICROCOPY RESOLUTION TEST CHART
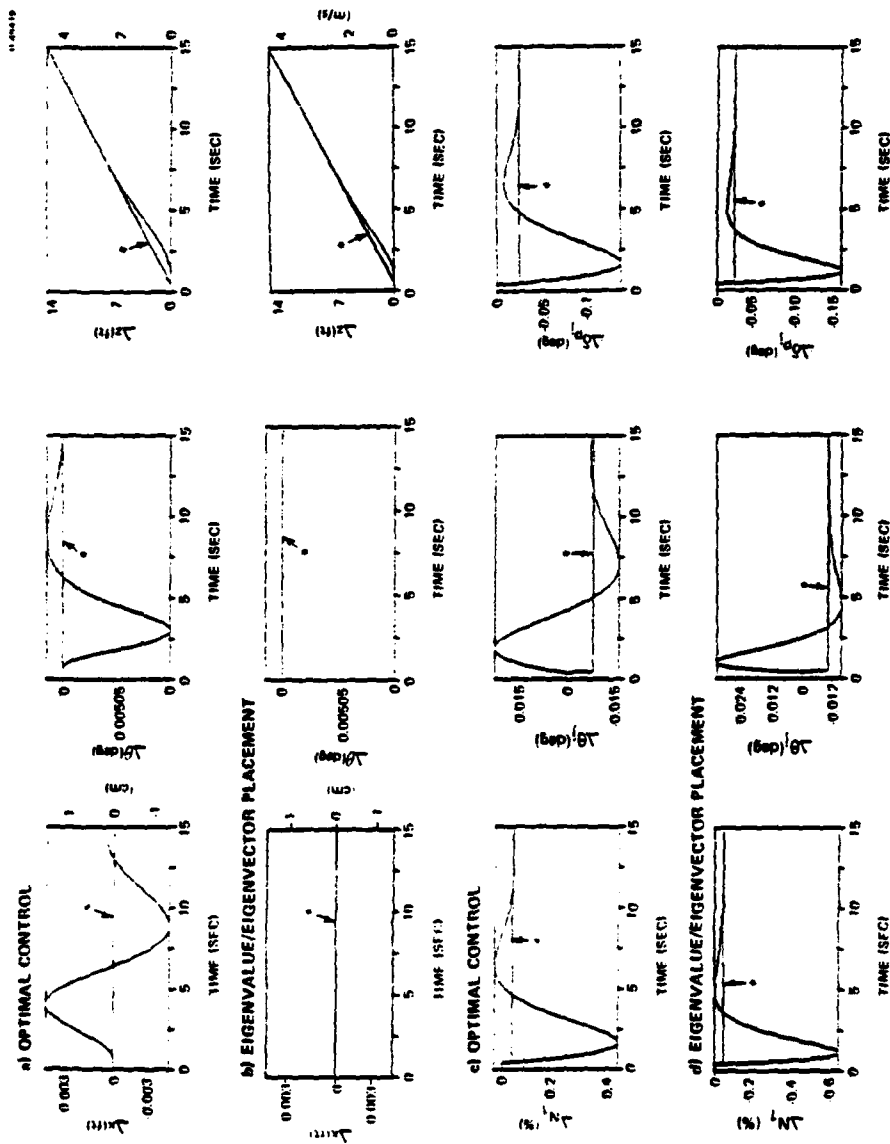
Figure 41   Comparison of Optimal Control and
Eigenvalue/Eigenvector Placement Vertical
Position Ramp Responses at 5.15 m/s (10 kt)
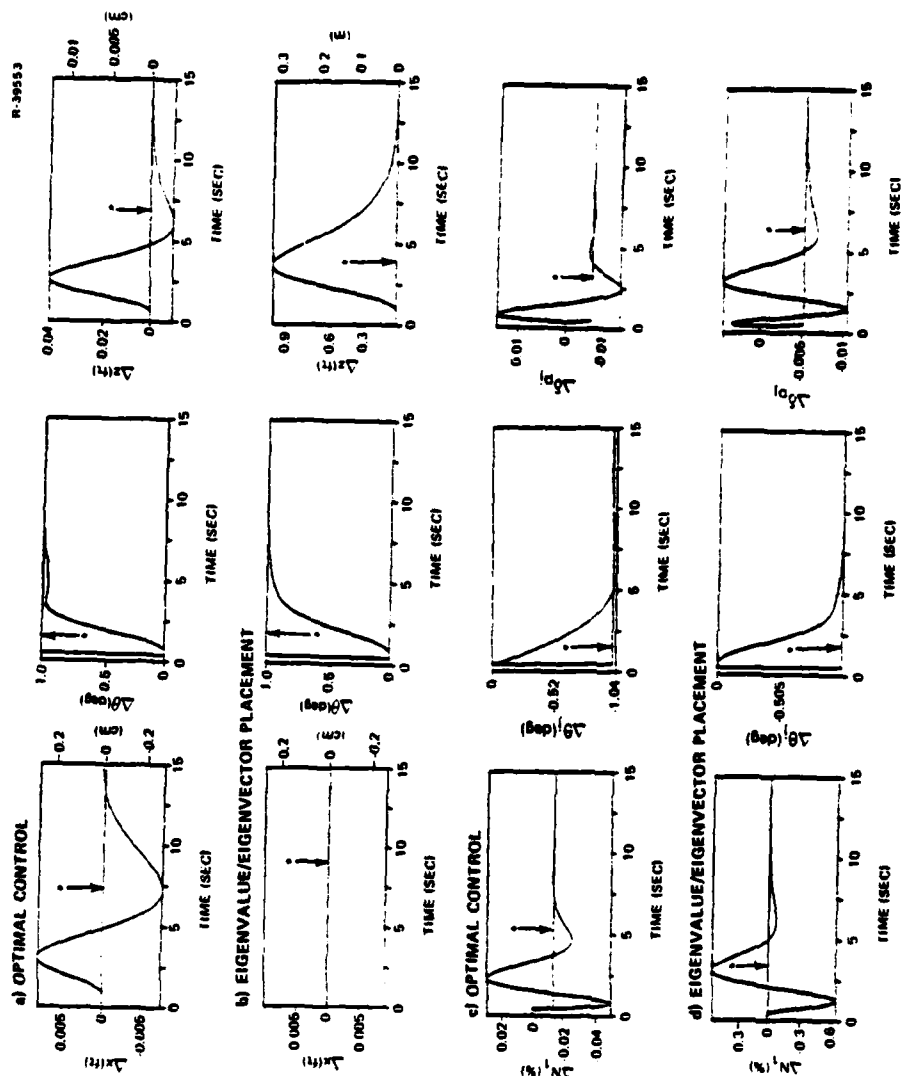
Figure 42   Comparison of Optimal Control and
Eigenvalue/Eigenvector Placement Pitch
Angle Step Responses at 5.15 m/s (10 kt)
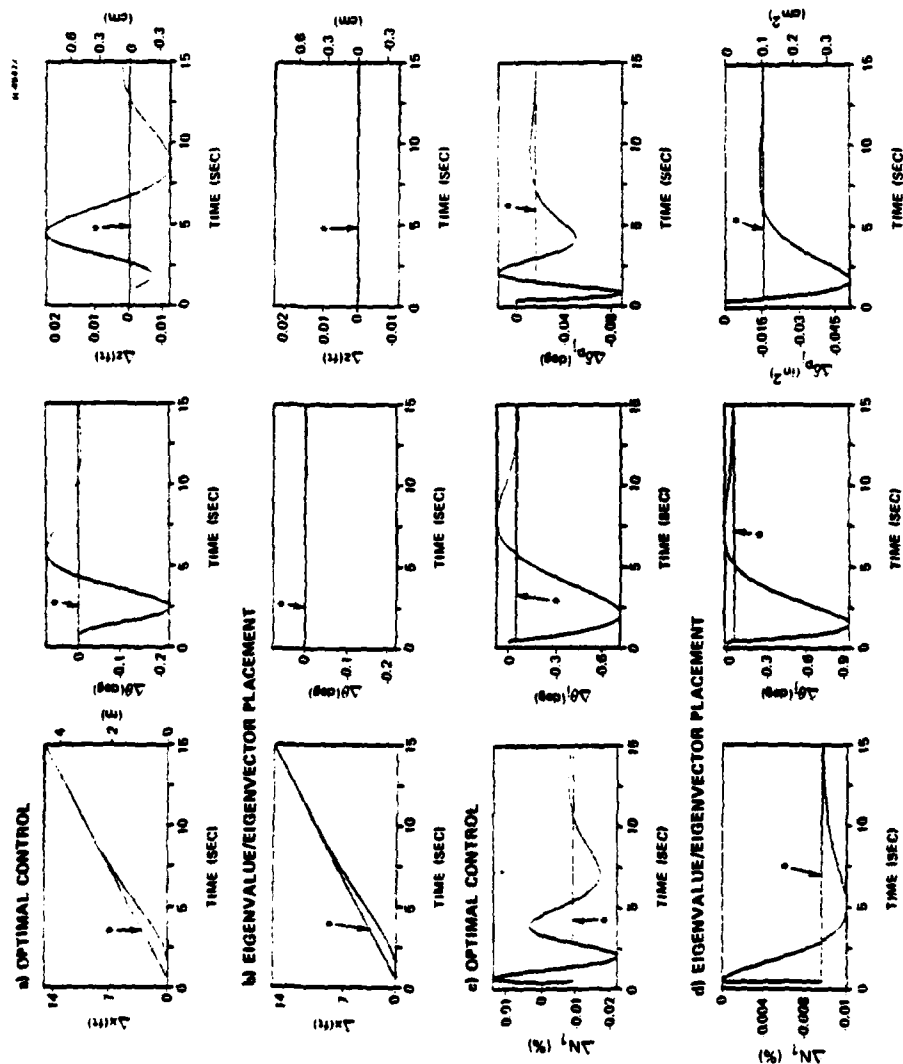
Figure 43   Comparison of Optimal Control and
Eigenvalue/Eigenvector Placement Axial
Position Ramp Responses at 5.15 m/s (10 kt)

3.4   CHAPTER SUMMARY

This chapter uses the recently developed theory of discrete-time feedforward control coupled with two powerful direct digital multivariable stabilization design procedures to obtain command augmentation systems for the AV-8A Harrier. The feedforward control allows the design of output model following for all types of command generator models; these models are constructed such that the aircraft follows their output trajectory. Six different command generator models, especially formulated for V/STOL control, are constructed, analyzed, and simulated. The two stabilization design procedures can interact equally with each of the command generator models. Each stabilization procedure has the desirable Type 1 property, and each procedure can be implemented using current fly-by-wire all digital technology.

The results with the command generator models demonstrate that rate commands, with attitude or velocity hold, (the ramp/step designs) commonly used in current classical analog designs can also be accomplished with optimal control. In a comparison between an optimal control ramp/step design and an optimal control dynamic model design, (the dynamic model being the common optimal control multivariable approach in the literature), the ramp/step approach yields comparable performance with less implementation complexity. Five of the six command generators investigated are ramp/step designs. Each of the command generators successfully uses five pilot inputs to command five aircraft outputs using all available controls independently. Thrust vectoring and reaction control at high forward velocity is shown to be difficult, but with proper considerations is feasible to design and certainly improves AV-8A performance in high speed flight. The transition and terminal area commands are velocity oriented, which is in agreement with pilot opinions. The results in this chapter

indicate, however, that in low speed flight, a roll command
rather than a cross-range velocity command is more appropriate
because pilots are reported to prefer a level platform rather
than automated lateral drift correction as the vehicle de-
scends to touchdown.

The stability augmentation designs for the AV-8A
exhibit uniform handling qualities over the flight conditions
investigated. Figure 44 shows two of the closed-loop mapped
high frequency eigenvalues overlaid on a specifications plot,
taken from Ref. 32. Results from Ref. 36 indicate desirable
positions of V/STOL complex pair eigenvalue locations for
Dutch roll (lat in Fig. 44) and short period (lon in Fig. 44).
The three V/STOL flight condition results from the design in
this chapter all fall within the optimum frequency and damping
window. When the V/STOL enters high speed flight, the aero-
dynamic controls take over at low dynamic pressure dropping
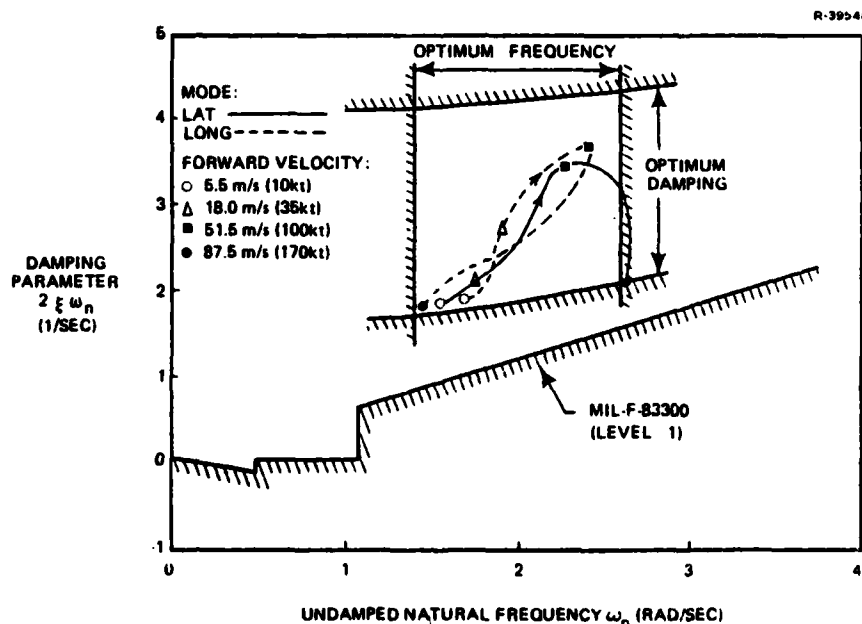
Figure 44   CGT-PI High Frequency Complex
             Pair Performance

the natural frequency of short period and the damping of Dutch roll as shown in Fig. 44.

A new direct digital design technique is presented and successfully applied to the AV-8A at low speeds. The technique is shown to be comparable to optimal control results and uniquely specifies a stability augmentation system by eigenvalue/eigenvector placement of the AV-8A dynamics. The new technique readily transforms designer time domain objectives such as decoupled response for the AV-8A at low speeds and pole placement into practice, but frequency domain performance would have to be checked for acceptability.

In summary, feedback and feedforward control theory is available for designing algorithms which greatly relieve pilot workload in commanding and stabilizing the complex, unstable, nonlinear dynamics of the V/STOL aircraft. The discrete-time feedforward/linear optimal control design combination can be a desirable candidate for improving and expanding the stability and control characteristics of current and future aircraft.

4. CONCLUSIONS AND RECOMMENDATIONS

This report has presented a number of advanced techniques for designing the stability and control systems of high performance aircraft and related performance results. In particular, the digital synthesis procedure was performed on the AV-8A Harrier in all flight regimes; ACM, high speed flight, transition and hover. The topics which have been addressed include the stability characteristics of the Harrier, new command and stabilization control theory, and it's application to the Harrier.

4.1 RESULTS

The results obtained in this investigation fall into eight categories:

- Characterization of hovering, low-speed and transition flight stability relationships, including the effects of velocity, angle of attack, flight path angle, and acceleration

- Characterization of stability during a ski-jump launch

- Characterization of low-speed stability in "ground effect" conditions

- Quantitative description of vectored thrust and reaction jet effects on the ability to stabilize and control the aircraft in maneuvering flight

- Development of an eigenvalue/eigenvector placement control law for an alternative synthesis technique to optimal control

theory and to obtain multivariable de-
coupling

- Development of a feedforward command
  theory (the command generator tracker)
  to ensure asymptotic output tracking of
  commands. A "Type 1" structure is added
  to account for aircraft parameter varia-
  tions

- Design of six pilot command models for
  precise handling and tracking of appro-
  priate aircraft variables during all
  flight regimes

- Preliminary design and analysis of a
  digital command augmentation system
  for the subject aircraft.

Actual results under each of these categories are discussed in
the following paragraphs.

Stability of the aircraft is examined using linear,
time-invariant dynamic models. Stability derivatives are
based on the AV-8A aerodynamic data contained in Ref. 6.
Vehicle stability evaluation proceeds in a manner similar to
the fighter aircraft analyses reported in Refs. 4 and 5. The
linear dynamic models include all the effects of inertial and
aerodynamic cross-couplings, and also model the effects of
vehicle acceleration on stability.

Although the general V/STOL model used here includes
the independent effects of each aerodynamic and reaction con-
trol, the trim conditions for stability analysis are found
assuming the same SAS-off control interconnects as on the
actual Harrier. Trim conditions are found in accelerated or
unaccelerated flight using the nonlinear aircraft dynamics.
For the work which examines vectored thrust and control de-
sign, the reaction jets and aerodynamic surface controls are
treated separately to maximize the payoff of the extra control

freedom. Stability relationships that are observed include those discussed in the following paragraphs:

Longitudinal stability is essentially a function of nozzle angle, θ_j. Above 50 deg θ_j, the static instability due to ram drag expresses itself as a relatively slow, unstable oscillation called the third mode, so-called because it is inherently different from the conventional short period and phugoid modes. For θ_j below 45 deg, the static instability appears as an angle-of-attack divergence that is even more unstable at lower θ_j. Finally, for the conventional flight configuration ($\theta_j = 0$ deg) at higher flight speeds, the instability completely disappears and conventional, stable, phugoid and short-period modes appear. The shipboard experience with the AV-8A, Ref. 7, agrees with these results.

Lateral stability is primarily a function of velocity and angle of attack, with the difficulty arising due to Dutch roll instability in the higher-α, lower-speed regime. In the lateral vehicle response, the classic roll and spiral modes and the Dutch roll oscillation describe the vehicle response throughout the speed regime.

Ground effect causes a large and very undesirable change in vehicle stability. Fast, unstable roll and altitude divergences appear that essentially prohibit any steady flight in ground effect.

Sideslip envelope restrictions in the transition speed range are significant due to a large positive dihedral effect and limited roll control power, as has been discussed in Ref. 8. A significant increase in roll control power on the YAV-8B lifts the sideslip envelope restrictions.

The AV-8A stability during a ski-jump launch is
studied. This launch technique (Ref. 9) allows a V/STOL air-
craft to take off at higher gross weight or lower airspeed
than is possible with a conventional short take off. The
stability study concludes that high angles of attack should be
avoided until the speed is high enough to justify the Dutch
roll instability that worsens as α increases. The highest
value of acceleration along the flight path also requires the
smallest value of nozzle angle, and therefore produces the
fastest longitudinal instability. An optimum (least unstable)
trade-off between normal and longitudinal acceleration may
exists.

Vectored thrust and reaction control in forward
flight for the AV-8A are examined using a series of command
models and the new theory of feedforward control reported in
Refs. 10 to 14. Feedforward control solves the general output-
following problem: given any desirable model to be followed,
either stable or unstable, how should the aircraft controls
move and what happens to the aircraft states when an output
vector of the aircraft states perfectly tracks an output
vector of the model states? When the dimension of the output
of the aircraft states is equal to or less than the number of
controls, the feedforward control problem almost always has a
solution.

Feedforward control solutions are performed for the
AV-8A using six different command models. Each command model
is adapted for a particular aspect of flying the V/STOL, such
as for air combat maneuvering in high speed flight, or for
3-dimensional position control near hover. Even though the
generalized AV-8A can have eight separately adjustable con-
trols only five outputs of the aircraft can be commanded.
There is insufficient lateral-directional control power to
independently command three lateral-directional outputs for
the AV-8A.

Vectored thrust at high velocities with proper control phasing allows for large normal acceleration commands with minimal increases in angle of attack as demonstrated using simulations. Near hover, proper movement of thrust magnitude and nozzle angle along with independent pitch jet control allows for complete decoupling of axial and vertical motion. Independent use of reaction jets in the lateral-directional axes at high velocities is shown to decrease sideslip excursions in rolling.

A highlight of the AV-8A digital control design study is that a significant contribution to linear control system theory has been made which has a direct and powerful impact on practical digital command augmentation system design. Feed-forward control theory, linear optimal regulator theory, and proportional-integral control, all in discrete-time, are combined to form the command generator tracker-proportional integral (CGT-PI) full authority controller. Using CGT-PI, states with non-constant steady state values are weighted in the infinite-time discrete cost function and yield optimal results. Inner-loop stability and outer-loop automatic guidance are simultaneously designed and simulated using CGT-PI. For the first time, a comparison is made between a model to be followed which has idealized dynamics but the same dimension as the aircraft model and models to be followed which are simply integrators with a lower dimension than the aircraft model. The idealized high dimensional dynamics model is shown not to offer appreciable advantages over the simpler models. For the first time, a comparison is made between discrete-time optimal control and discrete-time eigenvalue/eigenvector placement. Both stabilization procedures have the desirable closed-loop eigenvalue mapping property reported in Ref. 13 which enables the digital design to be evaluated using continuous-time specifications. The results show that each approach has its own advantages. The best procedure is to use the concepts together for maximum benefits.

The preceding paragraphs have described the contributions made in understanding the handling qualities of a jet V/STOL in hover, transition, and high speed flight. New practical control results which are better able to handle the demanding multivariable control complexity of the jet V/STOL are now available as a result of this study.

4.2   CONCLUSIONS

This investigation provided the following signigicant results and conclusions:

- Stability Characteristics

  The linear, time-invariant model, generated by linearizing the vehicle about trim points (flight conditions), exhibited several unstable characteristics. Longitudinal stability is greatly influenced by nozzle angle; angles less than 45° should be avoided in forward flight, if consistent with performance bounds. Lateral stability is influenced by velocity and angle of attack; low speed, high angles-of-attack destabilize the Dutch roll mode. Thus, sufficient velocities should be obtained in the ski-jump launch before angle-of-attack is increased. Ground effect causes large destabilizing divergence in roll and altitude; steady flight is essentially prohibited.

- Departure-Prevention Stability Augmentation

  Control laws which prevent vehicle instability and departure from controlled flight can be designed readily. The optimal linear regulator handles coupled dynamics by crossfeed paths which guarantee stability. An alternative method was developed here to accomplish this and decouple aircraft modes as well. The desired closed-loop eigenvalues (poles) and eigenvectors (modes) are chosen in the design process and the augmented vehicle will emulate

these characteristics. These techniques
enabled the augmented Harrier to perform
according to MIL specifications.

- <u>Departure-Prevention Command Augmentation Systems</u>

    Precision tracking response to pilot commands is
    afforded by employing the command generator
    tracker theory developed in this report. Feed-
    forward gains are generated using this technique
    which command the aircraft to track the pilot's
    commands. A "Type 1" proportional integral
    control was included to ensure perfect tracking
    for wide variations in the aircraft's parameters.
    This technique enabled the Harrier to perform
    properly in all flight regimes to commanded
    inputs.

- <u>Pilot Command Models</u>

    Adaptive command models were employed to obtain
    precise handling and tracking qualities at all
    flight regimes. Six different command models
    were constructed for a particular aspect of
    V/STOL flight and the gains can be scheduled
    as a function of flight condition. Hover
    requires three-dimensional position control
    and combat maneuvering requires accelera-
    tion commands -- up to five commands may be
    given simultaneously and independently.
    This scheme was necessary for a pilot to
    precisely handle the Harrier under such
    varying flight regimes.

- <u>CCV Design</u>

    The above techniques were employed in con-
    structing the AV-8A control laws since eight
    separate controls are available to obtain
    six degrees of vehicle freedom. The con-
    troller was generated for ACM, enroute,
    transition, terminal velocity and attitude
    flight regimes. Performance was superb
    in all regimes -- except attitude control
    at Hover. Side face thrust must be im-
    proved.

4.3 RECOMMENDATIONS

It is recommended that the following studies be undertaken to extend and demonstrate the utility of the work described in this report.

- Evaluate the CGT Using Nonlinear Aircraft Simulation

  Using the digitally implemented controller and gain adaptation logic, evaluate the Type 1 CGT and pilot command models by numerical simulation.

- Pilot-Aircraft Stability

  Determine pilot-aircraft stability boundaries as a function of the pilots' adaptation to changing flight conditions. Construct pilot strategies for controlling the "bare" airframe and suggest ARI configurations to alleviate difficulties.

- Evaluate the Sensitivity of Controller Gain Schedules to the Aircraft Model

  Evaluate the robustness of the control law with respect to aircraft parameter or trajectory variations.

- Effects of Partial State Feedback

  The aircraft sensors employed to measure the aircraft degrees of freedom and landing coordinates require state estimators to filter noise properly and reconstruct any non-measured states. The inclusion of this effort must be considered before implementation in the actual aircraft. A final design can be issued at this time.

- Investigate the Computational Advantages of Multi-Rate Control and Estimation

  The size of the onboard computer is largely a function of algorithm complexity and update rate. The advantages of sampling channels at various rates to reduce computational requirements should be evaluated.

APPENDIX A
DISCRETE-TIME COMMAND GENERATOR TRACKER

A most basic control problem is to require a plant, such as the V/STOL, to respond to command inputs, in the presence of disturbances, such that the output of the plant maintains a desired trajectory in real time. A method for solving this tracking problem is to formulate the desired trajectory and disturbances as the output of a system of linear differential equations. The tracking problem then reduces to finding the appropriate feedforward gains from the command generator linear system states and disturbance states to the plant control inputs so that command generator tracking is obtained. It is the purpose of this appendix to solve the command generator tracking (CGT) problem for linear, time-invariant, discrete-time plants.

The solutions of the command generator tracking problem for discrete-time, linear, time-invariant plants and models is a straightforward analogy of the continuous-time solution presented in Ref. 26. The only new concept needed, in both the continuous and discrete-time cases, is the introduction of the star trajectory. The star trajectories are curves in time that the plant states and controls must follow so that the plant output perfectly matches the model output when modeled disturbances affect the plant. The star trajectory primarily serves as a notational convenience and an aid in constructing the command generator tracking control laws.

The star trajectory is a generalization of steady-state and has appeared for continuous-time plants in Refs. 37

and 38. The star trajectory is determined by solving a set of algebraic matrix equations. Two new numerical procedures are shown in this appendix to solve the algebraic equations. An important by-product of the numerical procedures is the indication of sufficient conditions for a solution of the algebraic equations. The transmission zeroes of the discrete plant play an important role in understanding the sufficient conditions for finding the star trajectories. Transmission zeroes are the concept of zeroes of a transfer function generalized to multivariable systems and have become an important concept in the control literature (Ref. 39). The first part of this appendix defines discrete-time transmission zeroes and solves the CGT problem for linear, time-invariant plants.

An important feature of the command generator tracker is that it can be used in combination with classical or modern feedback control design procedures. Proper feedback control, especially proportional plus integral (PI) control, causes any errors between the actual plant trajectories and the ideal plant trajectories to decay to zero. PI control laws are useful when used with the CGT because the integral compensator estimates the model control's feedforward contribution to the plant control, forces the difference between plant output and model output to zero for certain types of plant modeling errors and can accommodate unmodeled bias disturbances in the plant. The discrete-time CGT-PI combination is the structure used with optimal control theory to design the control laws for the V/STOL in Chapter 4. A derivation of the CGT-PI control law is shown in the second part of this appendix.

This appendix concludes with a demonstration of eigenvalue/eigenvector assignment for discrete-time plants. Eigenvalue/eigenvector assignment of the plant modes can be accomplished using a special version of the CGT and is a form

101

of implicit model following. An example using CGT eigenvalue/ eigenvector placement is applied to the V/STOL in Chapter 4 and shows how feedback can be used to decouple the modes of the plant.

A.1   THE STAR TRAJECTORY

A discrete-time, linear, time-invariant plant may be represented as

$$\Delta \underline{x}_{k+1} = \Phi \Delta \underline{x}_k + \Gamma \Delta \underline{u}_k + E \Delta \underline{w}_k$$

$$\Delta \underline{y}_k = H \Delta \underline{x}_k + D \Delta \underline{u}_k + B \Delta \underline{w}_k$$

$$\Delta \underline{w}_{k+1} = \Phi_w \Delta \underline{w}_k$$

where $\Delta \underline{x}_k$ is an n-state vector, $\Delta \underline{u}_k$ is an m-control vector, $\Delta \underline{y}_k$ is an ℓ-observation vector, $\Delta \underline{w}_k$ is a p-disturbance vector and Φ, Γ, E, H, D, B, Φ_w are constant matrices of suitable dimension. It is assumed that the pair (Φ, Γ) is stabilizable and the pair (Φ, H) is detectable. A command generator (or model to be followed) can similarly be expressed as

$$\Delta \underline{x}_{m,k+1} = \Phi_m \Delta \underline{x}_{m,k} + \Gamma_m \Delta \underline{u}_{m,k}$$

$$\Delta \underline{y}_{m,k} = H_m \Delta \underline{x}_{m,k} + D_m \Delta \underline{u}_{m,k}$$

$$\Delta \underline{u}_{m,k} - \Delta \underline{u}_{m,k-1} = 0$$

where $\Delta \underline{x}_{m,k}$ is an n_m-state vector, $\Delta \underline{u}_{m,k}$ is an m_m-constant control vector, $\Delta \underline{y}_{m,k}$ is an ℓ-observation vector and Φ_m, Γ_m,

H_m, D_m are constant matrices of suitable dimension. The objective of the command generator tracker is to force the error state

$$\Delta\underline{\varepsilon}_k = [H \ D \ B] \begin{bmatrix} \Delta\underline{x}_k \\ \Delta\underline{u}_k \\ \Delta\underline{w}_k \end{bmatrix} - [H_m \ D_m] \begin{bmatrix} \Delta\underline{x}_{m,k} \\ \\ \Delta\underline{u}_{m,k} \end{bmatrix}$$

to go to zero. When the command error is zero, the plant states and controls are said to be tracking the star trajectory.

The star trajectory is defined to be the state and control trajectories, $\Delta\underline{x}_k^*$, and $\Delta\underline{u}_k^*$ that satisfy the plant dynamics

$$\Delta\underline{x}_{k+1}^* = \Phi\Delta\underline{x}_k^* + \Gamma\Delta\underline{u}_k^* + E\Delta\underline{w}_k \qquad (A-1)$$

and causes the command error to be zero, i.e.,

$$[H \ D \ B] \begin{bmatrix} \Delta\underline{x}_k^* \\ \Delta\underline{u}_k^* \\ \Delta\underline{w}_k \end{bmatrix} = [H_m \ D_m] \begin{bmatrix} \Delta\underline{x}_{m,k} \\ \\ \Delta\underline{u}_{m,k} \end{bmatrix} \qquad (A-2)$$

for all $k \geq 0$. An excellent analogy is that the star trajectory for linear systems is the counterpart of the nominal trajectory in nonlinear systems. Since the star trajectory is linear, it would be expected that the star trajectory satisfies a linear relationship with $\Delta\underline{x}_m$, $\Delta\underline{u}_m$, and $\Delta\underline{w}$. When the command $\Delta\underline{y}_m$ is constant and the disturbance is constant, (i.e., Φ_w, Φ_m, D_m are identity matrices, and B, Γ_m, H_m are zero matrices) Eqs. A-1 and A-2 can be combined to form

103

$$\begin{bmatrix} (\Phi-I) & \Gamma \\ \\ H & D \end{bmatrix} \begin{bmatrix} \Delta \underline{x}^* \\ \\ \Delta \underline{u}^* \end{bmatrix} = \begin{bmatrix} -E\Delta \underline{w} \\ \\ \Delta \underline{u}_m \end{bmatrix}$$

If the quad partition, $\begin{smallmatrix} (\Phi-I) & \Gamma \\ H & D \end{smallmatrix}$, is invertible, $\Delta \underline{x}^*$ and $\Delta \underline{u}^*$ can be found using the inverse

$$\begin{bmatrix} \Delta \underline{x}^* \\ \\ \Delta \underline{u}^* \end{bmatrix} = \begin{bmatrix} (\Phi-I) & \Gamma \\ \\ H & D \end{bmatrix}^{-1} \begin{bmatrix} -E\Delta \underline{w} \\ \\ \Delta \underline{u}_m \end{bmatrix} \qquad (A-3)$$

For constant commands and disturbances, the degenerate star trajectories are points in R^n and R^m and are linearly related to $\Delta \underline{w}$ and $\Delta \underline{u}_m$. Using Eq. A-3 as a guide, the star trajectories when $\Delta \underline{y}_m$ is not a constant is assumed to satisfy the linear relationship

$$\begin{bmatrix} \Delta \underline{x}_k^* \\ \\ \Delta \underline{u}_k^* \end{bmatrix} = \begin{bmatrix} A_{11} & A_{12} & A_{13} \\ \\ A_{21} & A_{22} & A_{23} \end{bmatrix} \begin{bmatrix} \Delta \underline{x}_{m,k} \\ \Delta \underline{u}_m \\ \Delta \underline{w}_k \end{bmatrix} \qquad (A-4)$$

The star trajectory can be determined if solutions for A_{11} to A_{23} exists in terms of plant and model parameters. The feed-forward matrices A_{11} to A_{23} are assumed to be constant and have the appropriate dimensions indicated in Eq. A-4.

A matrix equation for the feedforward matrices can be found by using the plant equations and the command error equation. Augmenting the plant with the command equation, Eq. A-2,

104

subtracting $[\Delta \underline{x}_k^{*T} \quad 0]^T$ from both sides and substituting Eq. A-4 for the vector $[\Delta \underline{x}_k^{*T} \quad \Delta \underline{u}_k^{*T}]^T$ produces.

$$
\begin{bmatrix} \Delta \underline{x}_{k+1}^* & -\Delta \underline{x}_k^* \\ \\ & \Delta \underline{y}_k^* \end{bmatrix} = \begin{bmatrix} (\Phi-I) & \Gamma \\ \\ H & D \end{bmatrix} \begin{bmatrix} A_{11} & A_{12} & A_{13} \\ \\ A_{21} & A_{22} & A_{23} \end{bmatrix} \begin{bmatrix} \Delta \underline{x}_{m,k} \\ \Delta \underline{u}_{m,k} \\ \Delta \underline{w}_k \end{bmatrix}
$$

$$
+ \begin{bmatrix} E \\ B \end{bmatrix} \Delta \underline{w}_k \tag{A-5}
$$

Subtracting $\Delta \underline{x}_k^*$ from $\Delta \underline{x}_{k+1}^*$ in the top row of Eq. A-4 and augmenting the alternate version of the command equation produces

$$
\begin{bmatrix} \Delta \underline{x}_{k+1}^* & -\Delta \underline{x}_k^* \\ \\ & \Delta \underline{y}_k^* \end{bmatrix} = \begin{bmatrix} A_{11}(\Phi_m-I) & A_{11}\Gamma_m & A_{13}(\Phi_w-I) \\ \\ H_m & D_m & 0 \end{bmatrix} \begin{bmatrix} \Delta \underline{x}_{m,k} \\ \Delta \underline{u}_m \\ \Delta \underline{w}_k \end{bmatrix} \tag{A-6}
$$

Equating the right-hand expressions in Eqs. A-5 and A-6 with $\Delta \underline{x}_{m,k}$, $\Delta \underline{u}_m$, and $\Delta \underline{w}_k$ arbitrary vectors produces the matrix equation for the feedforward matrices,

$$
\begin{bmatrix} (\Phi-I)\Gamma \\ H \quad D \end{bmatrix} \begin{bmatrix} A_{11} & A_{12} & A_{13} \\ A_{21} & A_{22} & A_{23} \end{bmatrix} = \begin{bmatrix} A_{11}(\Phi_m-I) & A_{11}\Gamma_m & A_{13}(\Phi_w-I)-E \\ H_m & D_m & -B \end{bmatrix} \tag{A-7}
$$

The next section presents two numerical procedures for calculating A_{11} to A_{23} in Eq. A-7 and indicates sufficient conditions for the existance of a solution.

A.2 NUMERICAL METHODS

Two numerical procedures for solving the feedforward matrix equation are presented in this section for the case when the number of controls, m, is greater than or equal to the number of commands, ℓ. The first procedure is numerically inefficient but intuitively instructive about the conditions for the existence of a feedforward matrix solution. The second procedure is numerically efficient and is used to generate the results in Chapter 4.

The feedforward matrix solution will depend on a relationship between the eigenvalues of the model and the discrete-time transmission zeroes of the discrete plant. Using a discrete-time analogy to the results in Ref. 40, a discrete-time transmission zero is any complex number, λ, which satisfies

$$\text{rank} \begin{bmatrix} (\Phi - \lambda I) & \Gamma \\ \\ H & D \end{bmatrix} < n + \ell \qquad (A-8)$$

The transmission zeroes can be determined using the eigenvalue/eigenvector relationship in Ref. 41 given by

$$\begin{bmatrix} \Phi & \Gamma \\ \\ H & D \end{bmatrix} \begin{bmatrix} \xi_x \\ \\ \xi_u \end{bmatrix} = \lambda \begin{bmatrix} I & 0 \\ \\ 0 & 0 \end{bmatrix} \begin{bmatrix} \xi_x \\ \\ \xi_u \end{bmatrix} \qquad (A-9)$$

where $[\xi_x^T \ \xi_u^T]^T$ is the transmission zeroes eigenvector. Using the right-weighted-pseudoinverse,

$$\begin{bmatrix} \Phi & \Gamma \\ \\ H & D \end{bmatrix} \begin{bmatrix} \Pi_{11} & \Pi_{12} \\ \\ \Pi_{21} & \Pi_{22} \end{bmatrix} = \begin{bmatrix} I & 0 \\ \\ 0 & I \end{bmatrix} \qquad\qquad \text{(A-10)}$$

Equation A-9 can be rewritten as

$$\Pi_{11} \underline{\xi}_x = \frac{1}{\lambda} \underline{\xi}_x \qquad\qquad \text{(A-11)}$$

$$\Pi_{21} \underline{\xi}_u = \frac{1}{\lambda} \underline{\xi}_x$$

The inverse of all eigenvalues of Π_{11} which are invariant under all pseudoinverses in Eq. A-10 are the transmission zeroes. An invariant <u>zero</u> eigenvalue, $\lambda_{\Pi,i}$, of Π_{11} means the transmission zero ($1/\lambda_{\Pi,i}$) is at infinity as in the classical sense for scalar transfer functions. When ℓ and m are equal, the pseudoinverse becomes an inverse and <u>all</u> eigenvalues of Π_{11} are transmission zeroes. An instructive but numerically poor way to compute the pseudoinverse is

$$\begin{bmatrix} \Pi_{11} & \Pi_{12} \\ \\ \Pi_{21} & \Pi_{22} \end{bmatrix} = Q_p^{-1} \begin{bmatrix} (\Phi-I) & \Gamma \\ \\ H & D \end{bmatrix}^T \left(\begin{bmatrix} (\Phi-I) & \Gamma \\ \\ H & D \end{bmatrix} Q_p^{-1} \begin{bmatrix} (\Phi-I) & \Gamma \\ \\ H & D \end{bmatrix}^T \right)^{-1}$$

where Q_p is the pseudoinverse weighting matrix. For the numerical results in the Chapter 4, the weighted pseudoinverse is actually computed using singular value decomposition (Ref. 42).

For the first numerical procedure one can use to compute the feedforward matrices, assume that T_m is the diagonalizing matrix for Φ_m and T_w is the diagonalizing matrix for Φ_w. Treating each matrix column partition in Eq. A-7 separately, each partition can be rewritten as follows

$$
\begin{bmatrix} \Phi & \Gamma \\ \\ H & D \end{bmatrix} \begin{bmatrix} A_{11} & T_m \\ \\ A_{21} & T_m \end{bmatrix} = \begin{bmatrix} A_{11}T_mT_m^{-1}\Phi_mT_m \\ \\ H_mT_m \end{bmatrix} \tag{A-12}
$$

$$
\begin{bmatrix} (\Phi-I) & \Gamma \\ H & D \end{bmatrix} \begin{bmatrix} A_{12} \\ A_{22} \end{bmatrix} = \begin{bmatrix} A_{11} & \Gamma_m \\ D_m \end{bmatrix} \tag{A-13}
$$

$$
\begin{bmatrix} \Phi & \Gamma \\ \\ H & D \end{bmatrix} \begin{bmatrix} A_{13} & T_w \\ \\ A_{23} & T_w \end{bmatrix} = \begin{bmatrix} A_{13}T_wT_w^{-1}\Phi_wT_w - ET_w \\ \\ -BT_w \end{bmatrix} \tag{A-14}
$$

If $\lambda_{m,i}$ denotes an eigenvalue of Φ_m and $\lambda_{w,i}$ denotes an eigenvalue of Φ_w, then Eqs. A-12 and A-14 can be rewritten as

$$
\begin{bmatrix} (\Phi-\lambda_{m,i}I) & \Gamma \\ \\ H & D \end{bmatrix} \begin{bmatrix} (A_{11}\ T_m)_i \\ \\ (A_{21}\ T_m)_i \end{bmatrix} = \begin{bmatrix} 0 \\ \\ (H_m\ T_m)_i \end{bmatrix} \quad i=1,\ldots,n_m
$$

$$\begin{bmatrix} (\Phi - \lambda_{w,i} I) & \Gamma \\ \\ H & D \end{bmatrix} \begin{bmatrix} (A_{13}\ T_w)_i \\ \\ (A_{23}\ T_w)_i \end{bmatrix} = \begin{bmatrix} (-ET_w)_i \\ \\ (-BT_w)_i \end{bmatrix} \quad i=1,\ldots,n_w$$

where $(A)_i$ denotes the ith column of the matrix A. Comparing the above two equations and Eq. A-12, with the definition of a transmission zero in Eq. A-8, it follows that the feedforward matrices have a solution provided no eigenvalue of either Φ_m or Φ_w is equal to a transmission zero of the plant and no discrete-time transmission zero is equal to one. Under these conditions, the quad partition matrix on the left-hand side of the above feedforward matrix equations have full rank and solutions for A_{11} to A_{23} are determined by solving each equation using singular value decomposition. Numerical procedures for handling complex matrices are found in Ref. 43.

In the second numerical procedure, the right pseudo-inverse of the quad partition matrix is used directly in Eq. A-7 to produce,

$$A_{11} = \Pi_{11}\ A_{11}\ \Phi_m + \Pi_{12}\ H_m \tag{A-15}$$

$$A_{13} = \Pi_{11}\ A_{13}\ \Phi_w - \Pi_{11}\ E - \Pi_{12}\ B \tag{A-16}$$

$$A_{21} = \Pi_{21}\ A_{11}\ \Phi_m + \Pi_{22}\ H_m$$

$$A_{23} = \Pi_{21}\ A_{13}\ \Phi_w - \Pi_{21}\ E - \Pi_{22}\ B$$

$$A_{12} = \chi_{11}\ A_{11}\ \Gamma_m + \chi_{12}\ D_m$$

$$A_{22} = X_{21} A_{11} \Gamma_m + X_{22} D_m$$

where

$$\begin{bmatrix} (\Phi - I) & \Gamma \\ \\ H & D \end{bmatrix} \begin{bmatrix} X_{11} & X_{12} \\ \\ X_{21} & X_{22} \end{bmatrix} = \begin{bmatrix} I & 0 \\ \\ 0 & I \end{bmatrix} \qquad (A\text{-}17)$$

The pseudoinverse, χ, shown in Eq. A-17 has the same weighting matrix used in constructing Π and is similarly computed using singular value decomposition. The non-trivial equations are Eqs. A-15 and A-16 which have the form

$$X = A \ X \ B + C$$

where X is unknown. A numerical algorithm to solve Eqs. A-15 and 16 is available by generalizing the results in Ref. 44 and using iterative residulization. The algorithm has a solution provided

$$\lambda_{\Pi,i} \ \lambda_{m,j} \neq 1$$

$$\lambda_{\Pi,i} \ \lambda_{w,j} \neq 1$$

where $\lambda_{\Pi,i}$ are the eigenvalues of Π_{11}. Using Eq. A-11 and the above two eigenvalue conditions, Eqs. A-15, A-16, and A-17 have a solution provided no eigenvalue of either Φ_m or Φ_w is equal to a transmission zero of the plant and no discrete-time transmission zeroes are equal to one. The conditions needed to determine the feedforward matrices using either numerical procedure presented is the same. The second numerical procedure has the advantage of using only real numbers (i.e., no complex arithmetic is needed) and the algorithms employed are noted for their efficiency.

110

A.3 PROPORTIONAL-INTEGRAL CONTROL ABOUT THE STAR TRAJECTORY

If the plant shown in Eq. A-1 is stable, then the open-loop control obtained by commanding $\Delta \underline{u}$ with $\Delta \underline{u}^*$ will cause the plant to asymptotically track $\Delta \underline{y}_m$ when $\Delta \underline{x}(0)$ and $\Delta \underline{x}^*(0)$ are not equal. For the AV-8A aircraft, however, many flight conditions are either unstable or have poor performance. The problem can be rectified by using additional control compensation.

One simple compensation is state feedback about the star trajectory

$$\Delta \underline{u}_k = \Delta \underline{u}_k^* + K(C\Delta \underline{x}_k - C\Delta \underline{x}_k^*) \tag{A-18}$$

where $C\Delta \underline{x}_k$ indicates that full state feedback is not necessary. If the error states,

$$\Delta \tilde{\underline{x}}_k = \Delta \underline{x}_k - \Delta \underline{x}_k^*$$

$$\Delta \tilde{\underline{u}}_k = \Delta \underline{u}_k - \Delta \underline{u}_k^*$$

are defined, substituting Eq. A-18 into the plant dynamics produces

$$\Delta \tilde{\underline{x}}_{k+1} = (\Phi - \Gamma KC) \Delta \tilde{\underline{x}}_k$$

If K is choosen so that the closed loop system is asymptotically stable then the error state $\Delta \tilde{\underline{x}}_k$ goes to zero as k increases, $\Delta \underline{x}_k$ goes to $\Delta \underline{x}_k^*$, $\Delta \underline{u}_k$ goes to $\Delta \underline{u}_k^*$, and $\Delta \underline{y}_k$ goes to $\Delta \underline{y}_{m,k}$.

The control law shown in Eq. A-18 can be rearranged to indicate the feedback and feedforward gains.

111

$$\Delta\underline{u}_k = KC\Delta\underline{x}_k + (A_{21}-KCA_{11})\Delta\underline{x}_{m,k} + (A_{22}-KCA_{12})\Delta\underline{u}_m$$

$$+ (A_{23}-KCA_{13})\Delta\underline{w}_k$$

If the plant dynamics have modeling errors (almost always the case) but K keeps the closed-loop plant stable, then perfect asymptotic tracking will probably not occur because the feedforward matrices are incorrect. Other problems in implementing the feedback/feedforward control law occur because $\Delta\underline{w}_k$ is usually not measured and noise disturbs the plant and disturbances. The last two problems mentioned are outside the scope of this work but are discussed in Refs. 28 and 45. The disturbance is dropped from the rest of this appendix.

Modeling error mismatch and feedforward matrix inaccuracies can be handled using additional compensator states. Examples of some current control theory work in this area for continuous-time problems are given in Refs. 46 and 47. Unfortunately none of these references demonstrate the connection between the feedforward matrices and compensators and no optimal control designs are presented. The discrete-time feedforward matrices presented in this appendix and the discrete-time star trajectories needed in the optimal control approach are new developments.

As an example of the connection between the feedforward matrices and compensators, consider the problem addressed in Section A.1 of tracking a constant command. Comparing Eqs. A-3, A-4, and A-17, the feedback/feedforward control law is

$$\Delta\underline{u}_k = KC\Delta\underline{x}_k + (\chi_{22} - KC\chi_{12})\Delta\underline{u}_m$$

If χ_{22} and χ_{12} are incorrect $\Delta\underline{y}_k$ will not necessarily be equal to $\Delta\underline{u}_m$ in steady-state. Consider next including integrator

states to form a proportional-integral control law as shown in Ref. 26. The control law in incremental form is

$$\Delta \underline{u}_k = \Delta \underline{u}_{k-1} + K_1 C(\Delta \underline{x}_k - \Delta \underline{x}_{k-1}) + K_2(\Delta \underline{y}_{k-1} - \Delta \underline{u}_m)$$

If there are modeling errors, but the proportional gain K_1 and the integral gain K_2 stabilize the plant, $\Delta \underline{y}_k$ is guaranteed to approach $\Delta \underline{u}_m$ in steady-state. Although χ_{22} and χ_{12} are needed in the derivation of the optimal PI control law as shown in Ref. 26, they are not needed in implementation.

In the AV-8A command models used in Chapter 4, most of the $\Delta \underline{y}_m$ commands are not constants hence there is an indication more advanced compensation is needed. In the following paragraphs, the discrete-time PI control law is re-derived including the generalized command model. After the derivation is complete, a discussion is presented indicating why the PI control law is usually adequate when using the complex command models presented in Chapter 4.

We begin by defining the error states and controls as before and include

$$\Delta \underline{\tilde{v}}_k = \Delta \underline{v}_k - \Delta \underline{v}_k^*$$

where $\Delta \underline{v}_k$ is the control difference,

$$\Delta \underline{u}_k = \Delta \underline{u}_{k-1} + \Delta t \Delta \underline{v}_{k-1} \qquad (A-19)$$

The ideal trajectory, $\Delta \underline{v}_k^*$, can be constructed as

$$\Delta \underline{v}_k^* = \frac{1}{\Delta t}(\Delta \underline{u}_k^* - \Delta \underline{u}_{k-1}^*) = \frac{1}{\Delta t}\left(A_{12}\left[\Delta \underline{x}_{m,k} - \Delta \underline{x}_{m,k-1}\right]\right)$$

Subtracting the ideal model response shown in Eq. A-1 from the plant, and adding and subtracting $\Delta t \underline{v}_k$ from Eq. A-19 produces

$$
\begin{bmatrix} \tilde{\underline{x}}_{k+1} \\ \tilde{\underline{u}}_{k+1} \end{bmatrix} = \begin{bmatrix} \Phi & \Gamma \\ 0 & I \end{bmatrix} \begin{bmatrix} \tilde{\underline{x}}_k \\ \tilde{\underline{u}}_k \end{bmatrix} + \begin{bmatrix} 0 \\ \Delta t I \end{bmatrix} \tilde{\underline{v}}_k
$$

The assumption is introduced that previous to k=0, the command $\Delta \underline{u}_m$ is constant and after k=0, $\Delta \underline{u}_m$ is constant, but at k=0 the command instantaneously changes,

$$
\Delta \underline{u}_{m,k} = \Delta \underline{u}_m(+) \qquad k = 0, 1, 2, \ldots
$$

$$
\Delta \underline{u}_{m,k} = \Delta \underline{u}_m(-) \qquad k = \ldots, -2, -1
$$

$$
\Delta \underline{u}_m(+) - \Delta \underline{u}_m(-) \neq 0 \qquad\qquad \text{(A-20)}
$$

In implementation, any time $\Delta \underline{u}_m$ changes the linear time-invariant plant is considered to be at k=0 (superposition). Equation A-20 allows us to continue with the derivation as if $\Delta \underline{u}_m$ is constant but will indicate the correct procedure to undergo if $\Delta \underline{u}_{m,k}$ is different from $\Delta \underline{u}_{m,k-1}$. If $\Delta \underline{u}_{m,k}$ is slowly varying with respect to the closed-loop system time constants, the control sequence will be almost always optimal.

The actual objective of the _optimal_ control is to transfer the plant from perfectly tracking the model output for $\Delta \underline{u}_m(-)$ to perfectly tracking the model output for $\Delta \underline{u}_m(+)$ while minimizing the cost function

$$
J = \sum_{k=-1}^{\infty} [\Delta \tilde{\underline{x}}_k \ \Delta \tilde{\underline{u}}_k \ \Delta \tilde{\underline{v}}_k]^T \begin{bmatrix} Q_1 & M_1 & M_2 \\ M_1^T & Q_2 & M_3 \\ M_2^T & M_3^T & R \end{bmatrix} \begin{bmatrix} \Delta \tilde{\underline{x}}_k \\ \Delta \tilde{\underline{u}}_k \\ \Delta \tilde{\underline{v}}_k \end{bmatrix}
$$

114

The cost function starts at $k=-1$ because $\Delta \tilde{\underline{v}}_{-1}$ is <u>not</u> specified, i.e.,

$$\tilde{\underline{v}}_{-1} = \frac{1}{\Delta t} (\tilde{\underline{u}}_0 - \tilde{\underline{u}}_{-1})$$

Before minimizing the cost function, a contradiction in the value of $\Delta \underline{x}_0^*$ must first be resolved.

At $k=1$ and $k=0$, Eq. A-4 produces

$$\begin{bmatrix} \Delta \underline{x}_{-1}^* \\ \\ \Delta \underline{u}_{-1}^* \end{bmatrix} = \begin{bmatrix} A_{11} & A_{12} \\ \\ A_{21} & A_{22} \end{bmatrix} \begin{bmatrix} \Delta \underline{x}_{m,-1} \\ \\ \Delta \underline{u}_m(-) \end{bmatrix} \tag{A-21}$$

$$\begin{bmatrix} \Delta \underline{x}_0^* \\ \\ \Delta \underline{u}_0^* \end{bmatrix} = \begin{bmatrix} A_{11} & A_{12} \\ \\ A_{21} & A_{22} \end{bmatrix} \begin{bmatrix} \Delta \underline{x}_{m,0} \\ \\ \Delta \underline{u}_m(+) \end{bmatrix} \tag{A-22}$$

and the ideal plant transient is

$$\Delta \underline{x}_0^* = \Phi \Delta \underline{x}_{-1}^* + \Gamma \Delta \underline{u}_{-1}^* \tag{A-23}$$

$\Delta \underline{x}_0^*$ specified by Eq. A-22 is not equal to $\Delta \underline{x}_0^*$ specified by Eqs. A-21 and A-23. To eliminate this discrepancy the requirement that

$$\Delta \underline{u}_{m,k} - \Delta \underline{u}_{m,k-1} = 0 \tag{A-24}$$

is invoked <u>only at index k</u>. As the system progresses with a constant $\Delta\underline{u}_m$, whenever $\Delta\underline{u}_{m,k}$ is different from $\Delta\underline{u}_{m,k-1}$, we go back to k-1 and <u>restart</u> all variables we have control over in time. For example, $\Delta\underline{x}_{m,k-1}$, $\Delta\underline{u}_{m,k-1}$, $\Delta\underline{x}^*_{k-1}$, and $\Delta\underline{u}^*_{k-1}$ can be changed but $\Delta\underline{x}_{k-1}$ and $\Delta\underline{u}_{k-1}$ are immutable for casual systems.

All that happens then is that the model is simulated as

$$\Delta\underline{x}_{m,k} = \Phi_m \, \Delta\underline{x}_{m,k-1} + \Gamma_m \, \Delta\underline{u}_{m,k}$$

and $\Delta\underline{u}_{m,k}$ can replace $\Delta\underline{u}_{m,k-1}$ in implementation as long as casuality is not violated. For example, $\Delta\underline{x}_{-1}$ and $\Delta\underline{u}_{-1}$ have already occurred when the cost function starts to be minimized, and $\Delta\underline{u}_m(+)$ becomes known at k=0. To stress the importance of Eq. A-24, the index k is not dropped for $\Delta\underline{u}_m$ in the following derivation.

The control, $\Delta\underline{\tilde{v}}_k$, which minimizes the cost function under general conditions is simply the solution to the linear optimal regulator,

$$\Delta\underline{\tilde{v}}_k = -K_1 \, \Delta\underline{\tilde{x}}_k - K_2 \, \Delta\underline{\tilde{u}}_k$$

where K_1 and K_2 are gains determined from the linear optimal regulator algebraic Riccati equation solution. The control $\Delta\underline{\tilde{u}}_k$ becomes

$$\Delta\underline{\tilde{u}}_k = \Delta\underline{\tilde{u}}_{k-1} - \Delta t K_1 \, \Delta\underline{\tilde{x}}_{k-1} - \Delta t K_2 \, \Delta\underline{\tilde{u}}_{k-1} \qquad (A-25)$$

and does not have the integral property.

The incremental form of the discrete control which has the Type 1 property is

$$\Delta \tilde{\underline{u}}_k = \Delta \tilde{\underline{u}}_{k-1} - C_1(\Delta \tilde{\underline{x}}_k - \Delta \tilde{\underline{x}}_{k-1}) - \Delta t C_2 (H\ D) \begin{bmatrix} \Delta \tilde{\underline{x}}_{k-1} \\ \\ \Delta \tilde{\underline{u}}_{k-1} \end{bmatrix} \quad \text{(A-26)}$$

The question to be answered is this: What transformation allows the Type 1 gain matrices, C_1 and C_2, to be expressed in terms of the Type 0 gains K_1 and K_2. The solution begins by noting that

$$\Delta \tilde{\underline{x}}_k - \Delta \tilde{\underline{x}}_{k-1} = (\Phi - I)\, \Delta \tilde{\underline{x}}_{k-1} + \Delta \tilde{\underline{u}}_{k-1}$$

and substituting this into Eq. A-26 producing,

$$\Delta \tilde{\underline{u}}_k = \Delta \tilde{\underline{u}}_{k-1} - [C_1\ \Delta t C_2] \begin{bmatrix} (\Phi - I) & \Gamma \\ \\ H & D \end{bmatrix} \begin{bmatrix} \Delta \tilde{\underline{x}}_{k-1} \\ \\ \Delta \tilde{\underline{u}}_{k-1} \end{bmatrix} \quad \text{(A-27)}$$

Equation A-27 is equivalent to Eq. A-25 if

$$[C_1\ \Delta t C_2] \begin{bmatrix} (\Phi - I) & \Gamma \\ \\ H & D \end{bmatrix} = [\Delta t K_1\ \Delta t K_2] \quad \text{(A-28)}$$

Equation A-28 is solved only for $\ell \leq m$, because for $\ell > m$ the cost function is almost always not finite.

The left weighted pseudoinverse of the quad partition transpose is used in Eq. A-28 so that the unknown gain magnitudes have the best possible alignment. If the same

117

pseudoinverse weighting matrix is used in Eq. A-28 as in Eq. A-17, the gains are determined from

$$[C_1 \ \Delta t C_2] = [\Delta t K_1 \ \Delta t K_2] \begin{bmatrix} x_{11} & x_{12} \\ x_{21} & x_{22} \end{bmatrix}$$

If $\ell < m$, Eq. A-28 is not necessarily an equality after C_1 and C_2 are calculated, and care should be taken when using the substitution.

With C_1 and C_2 determined, the PI command generator tracker becomes,

$$\Delta \underline{u}_k = \Delta \underline{u}_{k-1} - C_1(\Delta \underline{x}_k - \Delta \underline{x}_{k-1}) - \Delta t C_2 \left\{ (H \ D) \begin{bmatrix} \Delta \underline{x}_{k-1} \\ \Delta \underline{u}_{k-1} \end{bmatrix} \right.$$

$$\left. - (H_m D_m) \begin{bmatrix} \Delta \underline{x}_{m,k-1} \\ \Delta \underline{u}_{m,k} \end{bmatrix} \right\}$$

$$+ [C_1 A_{11} + A_{21}] \ [\Delta \underline{x}_{m,k} - \Delta \underline{x}_{m,k-1}] \qquad (A-29)$$

where $\Delta \underline{x}^*$ and $\Delta \underline{u}^*$ have been eliminated using Eq. A-4 and the following substitution

$$[C_1 \; I] \begin{bmatrix} \Delta \underline{x}_k^* - \Delta \underline{x}_{k-1}^* \\[1em] \Delta \underline{u}_k^* - \Delta \underline{u}_{k-1}^* \end{bmatrix} = [C_1 \; I] \begin{bmatrix} A_{11} & A_{12} \\[1em] A_{21} & A_{22} \end{bmatrix} \begin{bmatrix} \Delta \underline{x}_{m,k} - \Delta \underline{x}_{m,k-1} \\[1em] 0 \end{bmatrix}$$

Equation A-29 and A-25 have the same transient if $\ell = m$ but markedly different responses to sensor noise and plant variation.

The control law shown in Eq. A-29 depends on A_{11} and A_{21} but not on A_{12} and A_{22}. Any modeling errors that impact on A_{11} and A_{21} degrade the performance of the control law. There are basically two types of command models used in the AV-8A control law, models which generate ramps

$$\Delta \underline{x}_{m,k1} = \Delta \underline{x}_{m,k} + \Delta t \Delta \underline{u}_{m,k}$$

and model states that are dynamically stable. For the stable model states, the term $\Delta \underline{x}_{m,k} - \Delta \underline{x}_{m,k-1}$ in Eq. A-29 has an initial contribution to the control, $\Delta \underline{u}_k$, when $\Delta \underline{u}_{m,k}$ steps but as k increases $\Delta \underline{x}_{m,k} - \Delta \underline{x}_{m,k-1}$ approaches zero and the proportional-integral property of the control law shown in Eq. A-29 forces $\Delta \underline{y}_k$ to $\Delta \underline{y}_{m,k}$. The CGT-PI performs well for sufficiently asymptotically stable dynamic command models.

The same argument applies for the ramp command model. For example, when the pilot inputs a constant acceleration command, $\Delta \underline{a}$, the controls move to gain speed. Eventually, the pilot will stop accelerating the vehicle, $\Delta \underline{x}_{m,k} - \Delta \underline{x}_{m,k-1}$ becomes zero and the control law will force $\Delta \underline{y}_k$ to $\Delta \underline{y}_{m,k}$ removing any errors caused by modeling errors in A_{11} and A_{21}. In many instances with the AV-8A command models, A_{11} and A_{21} for ramp/step models are very sparse and any numbers at all are either 1 or can be investigated to determine their origin in

119

the original plant dynamics. Explicit expressions for A_{11} and A_{21} can then be programmed in implementation with no numerical inaccuracy. An example of sparse A_{11} and A_{21} are shown in Section 3.2.2.

The control law which removes the knowledge requirement for A_{11} and A_{21} when using <u>ramp models</u> is, of course, a Type 2 control law of the form

$$\Delta \underline{u}_k = \Delta \underline{u}_{k-1} + C_3(\Delta \underline{x}_k - \Delta \underline{x}_{k-1}) + \Delta t C_4 \Delta \underline{\xi}_{k-1}$$
$$+ \Delta t C_5 (\Delta \underline{y}_{k-1} - \Delta \underline{y}_{m,k-1})$$

$$\Delta \underline{\xi}_k = \Delta \underline{\xi}_{k-1} + \Delta t(\Delta \underline{y}_{k-1} - \Delta \underline{y}_{m,k-1})$$

In the Type 2 control law $\Delta t C_4 \Delta \underline{\xi}_{k-1}$ estimates the constant $[C_1 A_{11} + A_{21}]$ $[\Delta \underline{x}_{m,k} - \Delta \underline{x}_{m,k-1}]$. A fruitful area of research would be to combine the star trajectory, feedforward matrices, and Davison's servocompensator, (Ref. 46) into a unified, design approach using optimal control for discrete systems.

A.4   EIGENVALUE/EIGENVECTOR PLACEMENT

A new result in direct digital control design theory is presented in this section. In the CGT control law, using simple state feedback, consider the case where $\Delta \underline{x}_m$ has the same number of states as Δx, Φ_m has desirable eigenvalues and eigenvectors and Γ_m is a desirable control input matrix. The control law using full state feedback and dropping the disturbance term is

$$\Delta \underline{u}_k = K \Delta \underline{x}_k + (A_{21} - K A_{11}) \Delta \underline{x}_{m,k} + (A_{22} - K A_{12}) \Delta \underline{u}_m$$

Assume the feedback gain is chosen so that

$$K = A_{21} A_{11}^{-1} \qquad\qquad (A-30)$$

The control law becomes

$$\Delta \underline{u}_k = K\Delta \underline{x}_k + (A_{22} - A_{21} A_{11}^{-1} A_{12})\Delta \underline{u}_m \qquad\qquad (A-31)$$

Command generator tracking is obtained without feeding forward $\Delta \underline{x}_{m,k}$. The feedback gain shown in Eq. A-30 structurally changes the plant to behave like the model. Equation A-30 can be shown to be the discrete analog of an eigenvalue/eigenvector placement procedure discussed in Ref. 48.

The structural change caused by using K in Eq. A-30 for feedback is clearly evident by comparing the transfer function of the model with the transfer function of the plant, using Eq. A-31. Substituting Eq. A-31 into the plant produces

$$\Delta \underline{x}_{k+1} = A_{11} \Phi_m A_{11}^{-1} \Delta \underline{x}_k + \Gamma(A_{22} - A_{21} A_{11}^{-1} A_{12})\Delta \underline{u}_m$$

The first structural change noted is that the eigenvalues of the plant closed-loop matrix,

$$\Phi + \Gamma K = A_{11} \Phi_m A_{11}^{-1}$$

have been changed to the eigenvalues of the model, Φ_m. Noting that (D is assumed to be zero),

$$\Gamma A_{21} = A_{11}(\Phi_m - I) - (\Phi - I)A_{11}$$

$$\Gamma A_{22} = A_{11} \Gamma_m - (\Phi - I)A_{12}$$

the transfer function of the closed plant becomes after some manipulation,

121

$$\Delta \underline{y}_k = H(zI - A_{11} \Phi_m A_{11}^{-1})^{-1} [A_{11} \Gamma_m$$

$$+ (zI - A_{11} \Phi_m A_{11}^{-1})A_{12} + A_{12}(I-zI)]\Delta \underline{u}_m$$

Using the following information,

$$(zI - A_{11} \Phi_m A_{11}^{-1})^{-1} = A_{11}(zI-\Phi_m)^{-1} A_{11}^{-1}$$

$$(I-zI)\underline{u}_m = 0$$

$$H A_{11} = H_m$$

$$H A_{12} = D_m$$

the transfer function reduces to

$$\Delta \underline{y}_k = [H_m(zI-\Phi_m)^{-1} \Gamma_m + D_m]\Delta \underline{u}_m \qquad (A-32)$$

Comparing the transfer function in Eq. A-32 with the transfer function of the model

$$\Delta \underline{y}_{m,k} = [H_m(zI-\Phi_m)^{-1} \Gamma_m + D_m]\Delta \underline{u}_m$$

it follows that the gain in Eq. A-30 structurally changes the eigenvectors of the plant so that $\Delta \underline{y}_k$ is equal to $\Delta \underline{y}_{m,k}$ for constant $\Delta \underline{u}_m$ when the release condition for $\Delta \underline{x}_m(0)$ satisfies.

$$\Delta \underline{x}_{m,o} = A_{11}^{-1} \Delta \underline{x}_o - A_{11}^{-1} A_{12} \Delta \underline{u}_{m,o}$$

The eigenvalue/eigenvector placement procedure is demonstrated with the V/STOL aircraft using a PI design in Chapter 3.

APPENDIX B
COMMAND AUGMENTATION MODELS

Six command models shown in Table 8 are used to control the AV-8A at various flight conditions. Each command model has advantages and disadvantages depending on the application. This appendix presents the nonlinear relationships needed to construct the command vector $\underline{y}$ for each of the command models from the aircraft body states. The nonlinear relationships are linearized so that the feedback gains and feedforward matrices can be determined. Also shown are the linear and nonlinear command model dynamics used for model following and eigenvalue/eigenvector placement.

B.1 LINEAR AND NONLINEAR RELATIONSHIPS

The command augmentation system design method used in Chapter 4 requires the nonlinear version of the command model and the aircraft command vector, $\underline{y}$, for implementation and requires the linearized model and command vector for design. The first four command models in Table 8 are linear and do not have to be linearized. These models consist of simple integrators for the ramp commands and direct feedthrough of the model control, $\underline{u}_m$, for the step commands.

For example, the enroute ramp/step velocity command system is represented as

$$
\begin{bmatrix} V_{DR,m} \\ z_m \\ V_{CR,m} \\ \psi_m \end{bmatrix}_{k+1} = I \begin{bmatrix} V_{DR,m} \\ z_m \\ V_{CR,m} \\ \psi_m \end{bmatrix}_k + \begin{bmatrix} \Delta t & 0 & 0 & 0 & 0 \\ 0 & \Delta t & 0 & 0 & 0 \\ 0 & 0 & 0 & \Delta t & 0 \\ 0 & 0 & 0 & 0 & \Delta t \end{bmatrix} \begin{bmatrix} a_{DR,m} \\ V_{Z,m} \\ \theta_m \\ a_{CR,m} \\ \dot\psi_m \end{bmatrix}
$$

$$(B\text{-}1)$$

$$
\underline{Y}_{m,k} = \begin{bmatrix} 1 & 0 & 0 & 0 \\ 0 & 1 & 0 & 0 \\ 0 & 0 & 0 & 0 \\ 0 & 0 & 1 & 0 \\ 0 & 0 & 0 & 1 \end{bmatrix} \begin{bmatrix} V_{DR,m} \\ z_m \\ V_{CR,m} \\ \psi_m \end{bmatrix}_k + \begin{bmatrix} 0 & 0 & 0 & 0 & 0 \\ 0 & 0 & 0 & 0 & 0 \\ 0 & 0 & 1 & 0 & 0 \\ 0 & 0 & 0 & 0 & 0 \\ 0 & 0 & 0 & 0 & 0 \end{bmatrix} \begin{bmatrix} a_{DR,m} \\ V_{Z,m} \\ \theta_m \\ a_{CR,m} \\ \dot\psi_m \end{bmatrix}_{k+1}
\quad (B\text{-}2)
$$

The control vector $[a_{DR,m}, V_{Z,m}, \theta_m, a_{CR,m}, \dot\psi_m]^T$ is the pilot's input vector, $\Delta\underline{u}_m$. The other ramp/step models in Table 8 have structures similar to Eqs. B-1 and B-2 for both implementation and design, except for the air combat maneuvering (ACM) model. The nonlinear ACM model for the AV-8A at 87.5 m/s (170 kt) in continuous time is

$$
\dot{V}_m = \dot{V}_m \tag{B-3}
$$

$$
\dot\phi_{V,m} = P_{W,m} + \tan \gamma_m \, \sin \phi_{V,m} \, \frac{a_{n,m}}{V_m} + \tan \gamma_m \, \cos \phi_{V,m} \, \frac{a_{y,m}}{V_m}
$$
$$(B\text{-}4)$$

$$
\dot\xi_m = \frac{\sin \phi_{V,m}}{\cos \gamma_m} \, \frac{a_{n,m}}{V_m} + \frac{\cos \phi_{V,m}}{\cos \gamma_m} \, \frac{a_{y,m}}{V_m} \tag{B-5}
$$

$$\dot{\gamma}_m = \cos \phi_{V,m} \frac{a_{n,m}}{V_m} - \sin \phi_{V,m} \frac{a_{y,m}}{V_m} \qquad (B-6)$$

The complete ACM linearized command model becomes

$$
\begin{bmatrix} \Delta \dot{V}_m \\[2mm] \Delta \dot{\gamma}_m \\[2mm] \Delta \dot{\phi}_{V,m} \\[2mm] \Delta \dot{\xi}_m \end{bmatrix}
=
\begin{bmatrix}
0 & 0 & 0 & 0 \\[2mm]
-\dot{\gamma}_0/V_0 & 0 & -\cos \gamma_0 \dot{\xi}_0 & 0 \\[2mm]
\sin \gamma_0 \frac{-\xi_0}{V_0} & \cos \gamma_0 (1-\tan^2 \gamma_0)\xi_0 & \tan \gamma_0 \dot{\gamma}_0 & 0 \\[2mm]
-\dot{\xi}_0/V_0 & \tan \gamma_0 \, \xi_0 & \dfrac{\dot{\gamma}_0}{\tan \gamma_0} & 0
\end{bmatrix}
\begin{bmatrix} \Delta V_m \\[2mm] \Delta \gamma_m \\[2mm] \Delta \phi_{V,m} \\[2mm] \Delta \xi_m \end{bmatrix}
$$

$$
+
\begin{bmatrix}
1 & 0 & 0 & 0 & 0 & 0 \\[2mm]
0 & \cos \phi_{V,0} \frac{1}{V_0} & 0 & 0 & 0 & -\sin \phi_{V,0} \frac{1}{V_0} \\[2mm]
0 & \tan \gamma_0 \sin \phi_{V,0} \frac{1}{V_0} & 0 & 1 & 0 & \tan \gamma_0 \cos \phi_{V,0} \frac{1}{V_0} \\[2mm]
0 & \frac{\sin \phi_{V,0}}{\cos \gamma_0} \frac{1}{V_0} & 0 & 0 & 0 & \frac{\cos \phi_{V,0}}{\cos \gamma_0} \frac{1}{V_0}
\end{bmatrix}
\begin{bmatrix} \Delta \dot{V}_m \\[2mm] \Delta a_{n,m} \\[2mm] \Delta \alpha_m \\[2mm] \Delta P_{w,m} \\[2mm] \Delta \beta_m \\[2mm] \Delta a_{y,m} \end{bmatrix}
\ (B-7)
$$

The discrete equivalent of the linearized ACM command vector is formed using results shown in Table 5. Note that a_y and a_m are not the conventional specific contact force components, but do include the effects of gravity. Hence $\dot{V}$, a_y, and a_n completely describe the earth-relative acceleration of the aircraft.

The aircraft states that are commanded by the CGT-PI control to follow $\underline{y}_m$ form the aircraft command hold vector, $\underline{y}$ (Table 8). Many of the elements in the $\underline{y}$ vectors have non-linear relationships with the aircraft body states used in

$$\underline{x}^T = [x \ z \ \theta \ u \ q \ w \ v \ r \ p \ \phi \ \psi \ y]$$

125

design. In order to present the nonlinear and linearized
relationships we find it convenient to place the different
hold vectors into four groups.

The aircraft velocity in wind axis is the first group
and is related to the body-axis velocity by

$$
\begin{bmatrix} V \\ \beta \\ \alpha \end{bmatrix} = \begin{bmatrix} \sqrt{u^2 + v^2 + w^2} \\ \tan^{-1}(v/\sqrt{u^2 + w^2}) \\ \tan^{-1}(w/u) \end{bmatrix}
$$

V is the velocity magnitude, β is the sideslip angle and α is
the angle of attack. The velocity of the vehicle expressed in
inertial axis (a nonrotating, flat earth is assumed) helps
form the second group and is expressed as

$$
\begin{bmatrix} V_x \\ V_y \\ V_z \end{bmatrix} = H_B^I(\theta, \phi) \begin{bmatrix} u \\ v \\ w \end{bmatrix}
$$

The body to inertial transformation, H_B^I, is given by

$$
H_B^I(\psi, \theta, \phi) = \begin{bmatrix} \cos\psi & -\sin\psi & 0 \\ \sin\psi & \cos\psi & 0 \\ 0 & 0 & 1 \end{bmatrix} \begin{bmatrix} \cos\theta & 0 & \sin\theta \\ 0 & 1 & 0 \\ -\sin\theta & 0 & \cos\theta \end{bmatrix} \begin{bmatrix} 1 & 0 & 0 \\ 0 & \cos\phi & -\sin\phi \\ 0 & \sin\phi & \cos\phi \end{bmatrix}
$$

where roll, ϕ, pitch, θ, and yaw, ψ, are the body Euler
angles. The second group is composed of the vehicle velocity
expressed in local-level axes,

126

$$
\begin{bmatrix} V_{DR} \\ V_{CR} \\ V_z \end{bmatrix} = \begin{bmatrix} \cos\psi & \sin\psi & 0 \\ -\sin\psi & \cos\psi & 0 \\ 0 & 0 & 1 \end{bmatrix} \begin{bmatrix} V_x \\ V_y \\ V_z \end{bmatrix}
$$

In the models in Chapter 4, the vehicle is always assumed to be heading north which makes the nominal yaw angle zero.

The third group is the inertial velocity magnitude and inertial velocity Euler angles that are related to the inertial velocities by

$$
\begin{bmatrix} V \\ \xi \\ \gamma \end{bmatrix} = \begin{bmatrix} \sqrt{V_x^2 + V_y^2 + V_z^2} \\ \arccos\left(V_x/\sqrt{V_x^2 + V_y^2}\right) \\ \arcsin\left(V_z/\sqrt{V_x^2 + V_y^2 + V_z^2}\right) \end{bmatrix}
$$

ξ is the velocity heading angle and γ is the flight path angle. The last group consists of the wind-axis roll angle, ϕ_V, used in the air combat maneuvering command vector. The angle, ϕ_V, completes the transformations between the different axis systems as shown in Fig. B-1. The angle, ϕ_V, is calculated using one of the elements in the transformation

$$
H_V^W(\phi_V) = \begin{bmatrix} 1 & 0 & 0 \\ 0 & \cos\phi_V & \sin\phi_V \\ 0 & -\sin\phi_V & \cos\phi_V \end{bmatrix}
$$

$$
= H_B^W(\alpha,\beta) \; H_I^B(\phi,\theta,\psi) \; H_V^I(\gamma,\xi) \tag{B-5}
$$

127
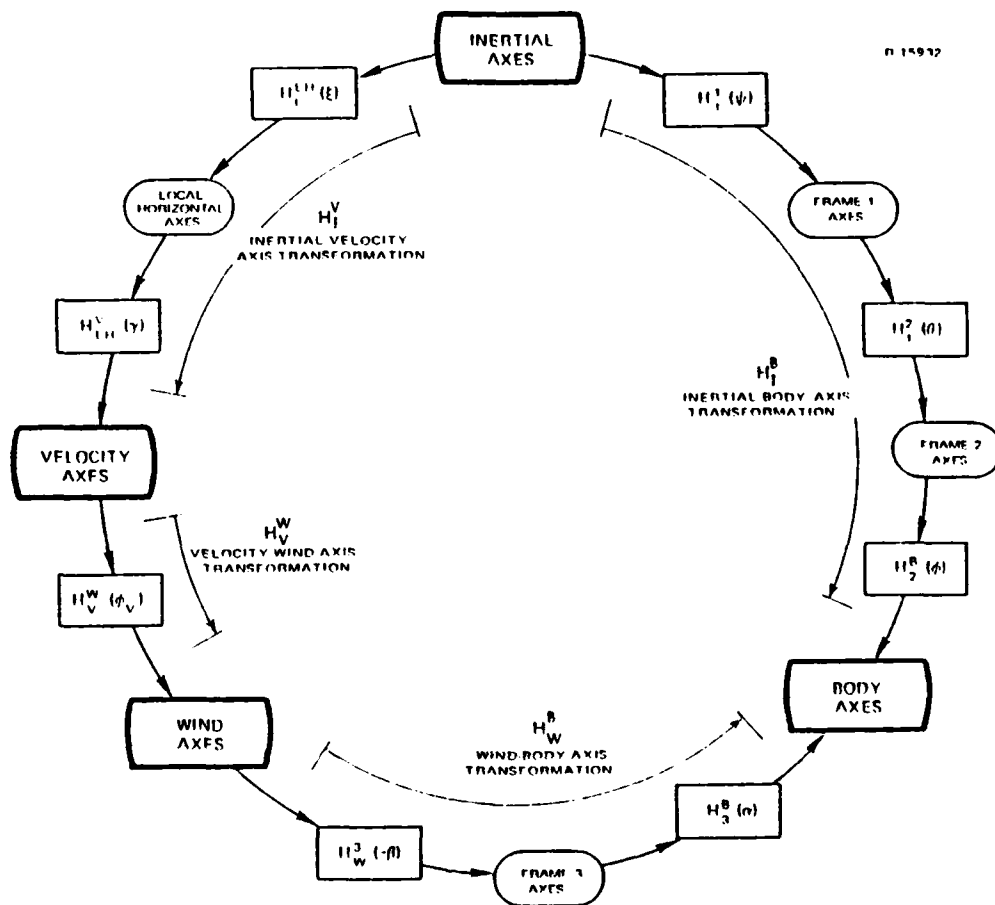
Figure B-1   Reference Axis Transformations
                (Arrows Indicate Right-Hand Rotation)

The body to wind axis transformation is the transpose of

$$
H_W^B(\alpha,\beta) = \begin{bmatrix} \cos\alpha & 0 & -\sin\alpha \\ 0 & 1 & 0 \\ \sin\alpha & 0 & \cos\alpha \end{bmatrix} \begin{bmatrix} \cos\beta & \sin\beta & 0 \\ -\sin\beta & \cos\beta & 0 \\ 0 & 0 & 1 \end{bmatrix}
$$

while the velocity to inertial axis transformation is the
transpose of

128

$$H_I^V(\gamma,\xi) = \begin{bmatrix} \cos\gamma & 0 & -\sin\gamma \\ 0 & 1 & 0 \\ \sin\gamma & 0 & \cos\gamma \end{bmatrix} \begin{bmatrix} \cos\xi & \sin\xi & 0 \\ -\sin\xi & \cos\xi & 0 \\ 0 & 0 & 1 \end{bmatrix}$$

Using available aircraft sensors (IMU, barometric altimeter, gyros, angle of attack and sideslip sensors) and ground radar when the aircraft is in the terminal area, Kalman filtering can be used to provide estimates of the commands used in all the command vectors, $\underline{y}$. An example of a Kalman filter design for a simple velocity command system is shown in Ref. 26.

The linearized version of each of the four command vector groups are shown next. Each of the linearized vectors are to be related to the linearized body-axis state vector, $\Delta\underline{x}^T$. The linearized wind-axis velocity vector is

$$\begin{bmatrix} \Delta V \\ \Delta\beta \\ \Delta\alpha \end{bmatrix} = J_W^{-1}(V_o,\beta_o)\ H_B^W(\alpha_o,\beta_o) \begin{bmatrix} \Delta u \\ \Delta v \\ \Delta w \end{bmatrix}$$

J_W is a diagonal matrix which has elements 1, V_o, and $V_o \cos \beta_o$. The inertial velocity vector varies with the Euler angles, hence the linearized inertial velocity vector includes the sensitivity to $\Delta\phi$, $\Delta\theta$, and $\Delta\psi$:

$$\begin{bmatrix} \Delta V_x \\ \Delta V_y \\ \Delta V_z \end{bmatrix} = H_{B,o}^I \begin{bmatrix} \Delta u \\ \Delta v \\ \Delta w \end{bmatrix} - H_{B,o}^I\ \tilde{v}_{B,o}\ L_{B,o} \begin{bmatrix} \Delta\phi \\ \Delta\theta \\ \Delta\psi \end{bmatrix} \tag{B-6}$$

$\tilde{v}_{B,o}$ is the cross-product equivalent matrix of the body axis velocities (no wind)

$$\tilde{v}_{B,o} = \begin{bmatrix} 0 & -w_o & v_o \\ w_o & 0 & -u_o \\ -v_o & u_o & 0 \end{bmatrix}$$

$L_{B,o}$ transforms Euler angle perturbations to body-axis coordinates and is given by

$$L_{B,o} = \begin{bmatrix} 1 & \sin \phi_o \tan \theta_o & \cos \phi_o \tan \theta_o \\ 0 & \cos \phi_o & -\sin \phi_o \\ 0 & \sin \phi_o \sec \theta_o & \cos \phi_o \sec \theta_o \end{bmatrix}$$

Since the nominal yaw angle is always zero in the design, the perturbation local-level velocity is the same as the perturbation inertial velocity. The linearized version of the inertial velocity magnitude and inertial Euler angles is accomplished by first relating them to the linearized inertial velocity vector,

$$\begin{bmatrix} \Delta V \\ \Delta \xi \\ \Delta \gamma \end{bmatrix} = \begin{bmatrix} \cos \gamma_o \cos \xi_o & \cos \gamma_o \sin \xi_o & -\sin \gamma_o \\ \dfrac{-\sin \xi_o}{V_o \cos \gamma_o} & \dfrac{\cos \xi_o}{V_o \cos \gamma_o} & 0 \\ \dfrac{-\sin \gamma_o \cos \xi_o}{V_o} & \dfrac{-\sin \gamma_o \sin \xi_o}{V_o} & \dfrac{-\cos \gamma_o}{V_o} \end{bmatrix} \begin{bmatrix} \Delta V_x \\ \Delta V_y \\ \Delta V_z \end{bmatrix}$$

130

Equation B-6 is substituted into Eq. B-7 to relate ΔV, $\Delta \xi$, and $\Delta \gamma$ to the perturbation body-axis states. The final and rather involved linearization is for ϕ_V. Using Eq. B-5, with $\Delta \phi_V$ the first element in the three state vector, $\Delta \underline{\mu}_W^V$, the linearization is

$$\Delta \underline{\mu}_W^V = H_{B,o}^W [I + H_{I,o}^B \, L_{V,o} \, J_{V,o}^{-1} \, \tilde{V}_{V,o} \, H_{I,o}^V \, H_{B,o}^I] L_{B,o} \begin{bmatrix} \Delta \phi \\ \Delta \theta \\ \Delta \psi \end{bmatrix}$$

$$- H_{B,o}^W [L_{W,o} \, J_{W,o}^{-1} + H_{I,o}^B \, L_{V,o} \, J_{V,o}^{-1} \, H_{W,o}^V] H_{B,o}^W \begin{bmatrix} \Delta u \\ \Delta v \\ \Delta w \end{bmatrix}$$

The matrices which have not already been identified in the expression for $\Delta \underline{\mu}_W^V$ are

$$\tilde{V}_{V,o} = \begin{bmatrix} 0 & 0 & 0 \\ 0 & 0 & -V_o \\ 0 & V_o & 0 \end{bmatrix}$$

$$L_{V,o} J_{V,o}^{-1} = \begin{bmatrix} 0 & \dfrac{\sin \xi_o}{V_o \cos \gamma_o} & 0 \\ 0 & \dfrac{-\cos \xi_o}{V_o \cos \gamma_o} & 0 \\ 0 & 0 & \dfrac{-1}{V_o} \end{bmatrix}$$

and

131

$$L_W J_W^{-1} = \begin{bmatrix} 0 & \dfrac{\sin \alpha_o}{V_o} & 0 \\[2em] 0 & 0 & \dfrac{1}{V_o \cos \beta_o} \\[2em] 0 & \dfrac{-\cos \alpha_o}{V_o} & 0 \end{bmatrix}$$

Using the equations given in this appendix, each of the six command hold vectors can be placed in the form

$$\Delta \underline{y} = H(\underline{x}_0) \, \Delta \underline{x}$$

The matrix D is not required for any of the command vectors. For the command vectors in Table 8 and the AV-8A dynamics at the different flight conditions, the matrix

$$\text{rank} \begin{bmatrix} F(x_0) & G(x_0) \\[1.5em] H(\underline{x}_0) & 0 \end{bmatrix} = n + \ell$$

always has full rank. When the quad partition matrix has full rank, the PI feedback gains can always be computed and the first of two conditions needed to compute the feedforward gains is satisfied.

B.2   MODEL FOLLOWING DESIGN

While most of command models used in the AV-8A control designs are simple integrators, a dynamic command model

132

is also used for comparative purposes from both a design and implementation point of view. This section describes the dynamic command model and discusses reasons for the choice of the numbers used in the model.

The longitudinal dynamics in the command model are desirably separated from the lateral-directional dynamics and have the form

$$
\begin{bmatrix} \Delta \dot{z}_m \\ \Delta \dot{\theta}_m \\ \Delta \dot{V}_{DR,m} \\ \Delta \dot{q}_m \\ \Delta \dot{V}_{z,m} \end{bmatrix} = \begin{bmatrix} 0 & 0 & 0 & 0 & 1 \\ 0 & 0 & 0 & 1 & 0 \\ 0 & 0 & f_1 & 0 & 0 \\ 0 & f_2 & 0 & f_3 & 0 \\ 0 & 0 & 0 & 0 & f_4 \end{bmatrix} \begin{bmatrix} \Delta z_m \\ \Delta \theta_m \\ \Delta V_{DR,m} \\ \Delta q_m \\ \Delta V_{z,m} \end{bmatrix}
$$

$$
+ \begin{bmatrix} 0 & 0 & 0 \\ 0 & 0 & 0 \\ g_1 & 0 & 0 \\ 0 & g_2 & 0 \\ 0 & 0 & g_3 \end{bmatrix} \begin{bmatrix} \Delta \delta_{VDR,m} \\ \Delta \delta_{q,m} \\ \Delta \delta_{Vz,m} \end{bmatrix} \qquad (B-8)
$$

The down-range velocity of the vehicle, height, and pitch angle command model dynamics are decoupled. The f_i elements are chosen to achieve acceptable closed-loop properties while the g_i elements are chosen to achieve response-to-input sensitivities compatible with the appropriate MIL-F-83300 requirements (Ref. 15). The elements f_1 and g_1 are -0.5 (2 second time constant) and 5.0 respectively. The numbers are taken from Ref. 19 where a model following system is

133

constructed similiar to Eq. B-8 for the X-22A V/STOL aircraft. The pitch angle and pitch rate time constants are chosen to be 0.625 seconds and 0.4 seconds respectively using Ref. 29 as a guide. The control element g_2 is set at 25.06 in order to meet the pitch attitude response in MIL-F-83300,

$$1.18(3) \leq \frac{\Delta\theta_m}{\Delta\delta_{q,m}} \leq 7.87(20) \text{ deg/cm (deg/inch) in one second}$$

The g_2 chosen gives a $\Delta\theta/\Delta\delta_{q,m}$ of approximately 1.57 deg/cm (4.0 deg/inch) for the command model. The MIL-F-83300 requirement on velocity response for the vertical axis is

$$12(100) \leq \frac{\Delta V_{z,m}}{\Delta\delta_{Vz,m}} \leq 90(750) \text{ mpm/cm (fpm/inch) in one second}$$

Setting f_4 to -1.5 (0.667 time constant) for good response characteristics, a g_3 of 11.26 provides a $\Delta V_{z,m}/\Delta\delta_{V,z,m}$ of 42 mpm/cm (350 fpm/inch) in one second for the command model.

In the lateral-directional command model, a turn-coordinated system is considered desirable. Only two of the states, Δv and $\Delta\psi$, are to be commanded and lateral-directional coupling is not particularly desirable hence the model becomes

$$\begin{bmatrix} \Delta\dot{v}_m \\ \Delta\dot{r}_m \\ \Delta\dot{\psi}_m \end{bmatrix} = \begin{bmatrix} f_5 & f_6 & 0 \\ f_7 & f_8 & 0 \\ 0 & 1 & 0 \end{bmatrix} \begin{bmatrix} \Delta v_m \\ \Delta r_m \\ \Delta\psi_m \end{bmatrix} + \begin{bmatrix} g_4 & g_5 \\ g_6 & g_7 \\ 0 & 0 \end{bmatrix} \begin{bmatrix} \Delta\delta_{r,m} \\ \Delta\delta_{v,m} \end{bmatrix} \qquad \text{(B-9)}$$

If roll angle and roll rate, $\Delta\phi_m$ and Δp_m, are included in the model without coupling to the above states and controls, the appropriate columns in the feedforward matrices (see Appendix

134

A) are zero. The ideal dynamic model does not have to have the same number of states as the aircraft model. The element f_6 in F_m in Eq. B-9 is set approximately equal to its counterpart in the plant dynamics (-2.9066 in F, -2.9 in F_m).

A desirable complex pair for Δv_m and Δr_m has a natural frequency of 2.07 rad/sec and a damping ratio of 0.6. These choices place the models lateral model approximately in the middle of the optimum frequency and damping window shown in Fig. 43. Assuming f_5 and f_8 are equal the values become -1.242 and 0.9456 for f_5 and f_7, respectively. Two conditions are used to determine g_4 and g_6. First, when $\Delta \delta_{\dot\psi,c}$ is stepped, the steady-state value of Δv_m should be zero and second, the yaw response should satisfy the requirement in MIL-F-83300 given by

$$2.36(6.0) \leq \frac{\Delta\psi}{\Delta\delta_{\dot\psi,c}} \leq 9.06(23) \text{ deg/cm (deg/inch) in one second}$$

Using a $\Delta\psi/\Delta\delta_{\dot\psi,c}$ of 2.53 deg/cm (6.43 deg/inch) the values for g_4 and g_6 are 23.2 and 9.936 respectively. When $\Delta\delta_{v,c}$ is commanded to 2.54 cm (1 inch), the steady-state value of Δv_m is to be 3.05 m/s (10 fps) with Δr_m in steady-state at zero. The values for g_5 and g_7 become 12.42 and -9.456 respectively. The pilot command, $\Delta\delta_{v,c}$, would normally be considered a pedal control and is designed not to be used by the pilot to execute a coordinated turn.

B.3   EIGENVALUE/EIGENVECTOR PLACEMENT MODEL

This section discusses how the longitudinal continuous-time eigenvalue/eigenvector placement (EEP) model used in Section 4.3.4 is constructed and indicates the numerical values in the model. The eigenvalue/eigenvector

135

placement model requires a structure completely different from the feedforward gain model presented in the previous section.

The EEP model must have all eigenvalues in the open left-half complex plane. The plant eigenvalues will be changed by feedback to the EEP model eigenvalues and asymptotic tracking requires all closed-loop eigenvalues to be stable. The EEP model modes should be structurally similar to the modes in the original plant in order to avoid large gains and sensitivity to modeling errors. For example, complex roots in the aircraft open-loop dynamics such as Dutch roll and short period generally should also appear in the EEP model but at more desirable locations. The EEP model to be used in Chapter 4 is compared with an optimal control proportional-integral control design, hence, additional compensator states are adjoined to the usual aircraft body-axis states in the EEP model to obtained the Type 1 property. The compensator states are the same as the control states adjoined to the plant which allow the control rate to be weighted in the optimal control cost function (Table 4).

The EEP model in continuous-time has the form

$$
\begin{bmatrix} \Delta \dot{\underline{x}}_m \\ \Delta \dot{\underline{u}}_m \end{bmatrix} = \begin{bmatrix} F_m & G_m \\ 0 & T_u \end{bmatrix} \begin{bmatrix} \Delta \underline{x}_m \\ \Delta \underline{u}_m \end{bmatrix}
$$

No control input to the model is required since the EEP model is not to be used for control interconnect design. The EEP model is used to design a PI control law for low speed flight using the longitudinal dynamics. The three available AV-8A longitudinal controls at hover can be used to force three outputs of the aircraft to have transients exactly like the EEP model and at the same time force all the eigenvalues of

136

the plant to be those of the EEP model. The three outputs chosen are Δx_m, Δz_m, and $\Delta\theta_m$ of the following ideal model,

$$
\begin{bmatrix} \Delta\dot{x}_m \\ \Delta\dot{z}_m \\ \Delta\dot{\theta}_m \\ \Delta\dot{u}_m \\ \Delta\dot{q}_m \\ \Delta\dot{w}_m \\ \Delta\dot{\delta}_u \\ \Delta\dot{\delta}_q \\ \Delta\dot{\delta}_w \end{bmatrix}
=
\begin{bmatrix}
0 & 0 & 0 & 1 & 0 & 0 & 0 & 0 & 0 \\
0 & 0 & 0 & 0 & 0 & 1 & 0 & 0 & 0 \\
0 & 0 & 0 & 0 & 1 & 0 & 0 & 0 & 0 \\
f_x & 0 & 0 & f_u & 0 & 0 & g_u & 0 & 0 \\
0 & 0 & f_\theta & 0 & f_q & f_{qw} & 0 & g_q & 0 \\
0 & f_z & 0 & 0 & f_{wq} & f_q & 0 & 0 & g_w \\
0 & 0 & 0 & 0 & 0 & 0 & \tau_u & 0 & 0 \\
0 & 0 & 0 & 0 & 0 & 0 & 0 & \tau_q & 0 \\
0 & 0 & 0 & 0 & 0 & 0 & 0 & 0 & \tau_w
\end{bmatrix}
\begin{bmatrix} \Delta x_m \\ \Delta z_m \\ \Delta\theta_m \\ \Delta u_m \\ \Delta q_m \\ \Delta w_m \\ \Delta\delta_u \\ \Delta\delta_q \\ \Delta\delta_w \end{bmatrix}
\quad\text{(B-10)}
$$

The feedback gains determined using the discrete version of Eq. B-10 will have the same form as Eq. A-25, and will require the same gain transformation using the command vector $H(\underline{x}_0)$ matrix as shown in Eq. A-28. After the transformation, the EEP gains will be C_1 and C_2 in Eq. A-29 just as in the optimal control design. The control modes τ_u, τ_q, and τ_w in Eq. B-10 will be the integrator eigenvalues after the transformation shown in Eq. A-28. The EEP model dynamics have the velocity and position states $\Delta\underline{x}$ and $\Delta\underline{u}$ decoupled from the rest of the states. Decoupled velocity control is known to obtain favorable pilot ratings (Ref. 3). The element f_{qw} is also set to zero so that a Δz command does not change pitch angle in the transient response.

The rest of the f and τ elements are chosen so that the eigenvalues of the EEP model are approximately the same as the corresponding optimal control design eigenvalues subject to the eigenvector constraints dictated in Eq. B-10. This

137

choice satisfies the EEP model requirements previously mentioned and makes the comparison between EEP model design and optimal control design easier. Table B-1 shows the closed-loop optimal control eigenvalues, the EEP model eigenvalues, and the EEP model parameters that generated the results. The parameters g_u, g_q, and g_w have little effect on C_1 and C_2 and are chosen to be 2.5, 30.03, and 26.86 respectively using MIL-F-83300 and the results in the previous section. More discussion comparing EEP and optimal control is given in Chapter 4.

TABLE B-1

COMPARISON BETWEEN OPTIMAL CONTROL AND
EIGENVALUE/EIGENVECTOR PLACEMENT CLOSED-LOOP EIGENVALUES

T-2912

DYNAMIC MODE	OPTIMAL CONTROL			EIGENVALUE/EIGENVECTOR PLACEMENT			EIGENVALUE/EIGENVECTOR MODEL ELEMENTS
	NATURAL FREQUENCY, rad/sec	DAMPING RATIO	TIME CONSTANT, sec	NATURAL FREQUENCY, rad/sec	DAMPING RATIO	TIME CONSTANT, sec	
Δq-Δw	1.68	0.569	-	1.77	0.614	-	$\begin{pmatrix} f_q = -2.181 \\ f_{wq} = 4.96 \end{pmatrix}$
Δx-$\int \Delta x$	0.694	0.687	-	$\begin{pmatrix} 1.43 \\ 1.25 \end{pmatrix}$			$\begin{pmatrix} f_x = -0.35 \\ \tau_u = -0.8 \end{pmatrix}$
Δz-$\int \Delta z$	0.635	0.689	-	$\begin{pmatrix} 1.39 \\ 1.11 \end{pmatrix}$			$\begin{pmatrix} f_z = -1.0494 \\ \tau_w = -0.9 \end{pmatrix}$
Δu	-	-	2.02			2.00	$f_u = -1.2$
$\Delta \theta$	-	-	0.555			0.682	$f_\theta = -3.147$
$\int \Delta \theta$	-	-	1.34			1.33	$\tau_q = -0.75$

138

APPENDIX C
AIRCRAFT AERODYNAMIC AND CONTROL SYSTEM MODEL

The aerodynamic and mass data used in this report are discussed in this appendix. A simple ground-effect model is also described, and a description of the AV-8A control system is included.

C.1   AERODYNAMIC AND MASS DATA

The basic source of aerodynamic data for the AV-8A V/STOL aircraft is Ref. 6. The aircraft size and mass data used in this report are given in Table C-1. The aircraft model used in this report included independent effects of ten control variables, as listed in Table C-2. Note that on the actual AV-8A, some of these are mechanically interconnected as discussed later in this appendix.

TABLE C-1
CHARACTERISTICS OF THE AV-8A HARRIER

T-3068

Mass, m	410.0	slugs	5983.	kg
Reference Area, S	201.0	ft^2	18.67	m^2
Mean Aerodynamic Chord, $\bar{c}$	7.95	ft	2.42	m
Wing Span, b	25.25	ft	7.70	m
Center of Gravity Location, x_{cg}			0.09	$\bar{c}$
z_{cg}			0.00	$\bar{c}$

139

TABLE C-2
CONTROL VARIABLE RANGES

T-3069

Throttle, δ_{N1}	105%	to	0%
Stabilator, δ_s	11.3	to	-10.0 deg
Nozzle Angle, $\delta_{\theta j}$	98.5	to	0.0 deg
Front Pitch Jet, δ_{FP}	7.23	to	0.0 in^2
Rear Pitch Jet, δ_{RP}	8.68	to	0.0 in^2
Aileron, δ_a	12.0	to	-12.0 deg
Right Roll Jet, δ_{RR}	4.2	to	-4.2 in^2
Left Roll Jet, δ_{LR}	4.2	to	-4.2 in^2
Rudder, δ_r	15.0	to	-15.0 deg
Yaw Jet, δ_{yj}	3.5	to	-3.5 in^2

The linearized aircraft model used in this study is based on the complete six-degree-of-freedom nonlinear aircraft equations of motion.

$$\dot{\underline{x}}_I = H_B^I \, \underline{v}_B \tag{C-1}$$

$$\dot{\underline{v}}_B = L_B^{-1} \, \underline{\omega}_B^I \tag{C-2}$$

$$\dot{\underline{v}}_B = (\underline{F}_B + \underline{T}_B)/m + H_I^B \underline{g}_I - \tilde{\omega}_B^I \underline{v}_B \tag{C-3}$$

$$\dot{\underline{\omega}}_B^I = I_B^{-1}(\underline{M}_B + \underline{G}_B) - I_B^{-1}\tilde{\omega}_B^I I_B \underline{\omega}_B^I \tag{C-4}$$

The following paragraphs describe the functional relations used to calculate the aerodynamic and thrust forces and moments. The data which is used in these relationships is given in Ref. 6.

140

The thrust forces and moments and those due to the reaction jets are not direct functions of dynamic pressure, and they are calculated, for the purposes of this report, for sea-level standard atmosphere conditions. Figure C-1 illustrates the point of application of all these forces. The reaction jet forces are calculated first, and they are a function of the pressure ratio in the reaction ducting

$$\varepsilon_{RCS} = \varepsilon_{RCS}(\delta_{N1}, \delta_{\theta j}, \delta_{ATOT}) \tag{C-5}$$

where

$$\delta_{ATOT} = \delta_{FP} + \delta_{RP} + \left|\delta_{LR}\right| + \left|\delta_{RR}\right| + \left|\delta_{YAW}\right| \tag{C-6}$$

The absolute value signs are necessary because a "negative jet area" is used to indicate a thrust in the opposite direction for the bi-directional jets. The reaction jet duct is shut

R 42144
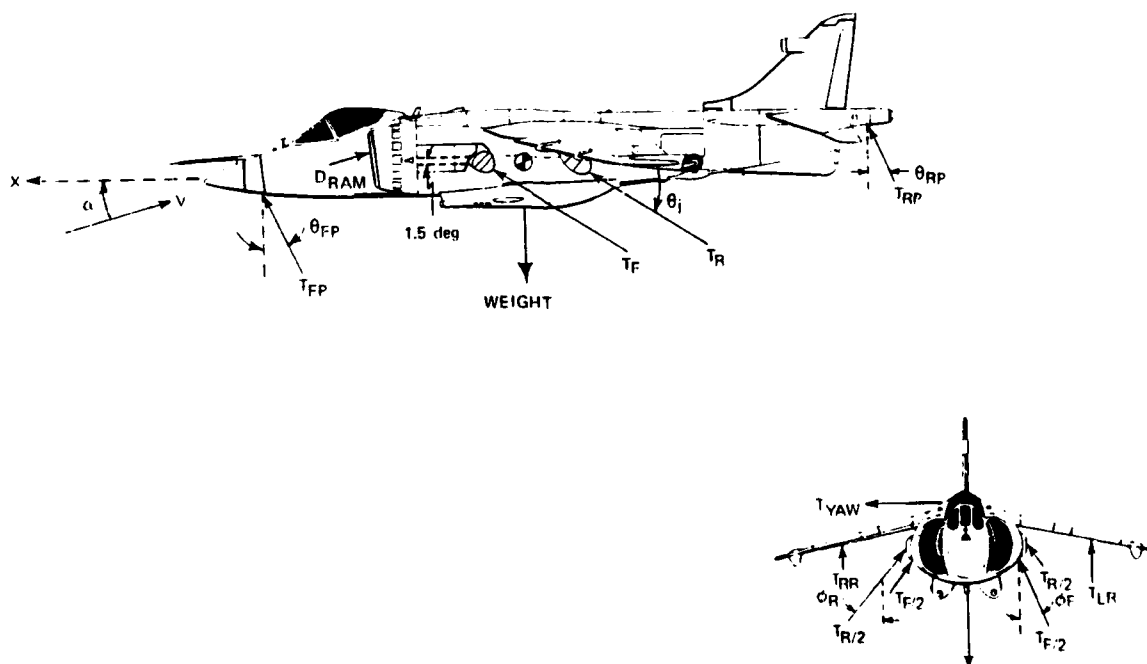
Figure C-1   Main Nozzle RCS Jet Location

141

off for nozzle angles below 20 deg, which is the only effect of $\delta_{\theta j}$, and the duct pressure increases with engine speed. The effect of δ_{ATOT} is to decrease the duct pressure as the reaction jets open. The magnitude of the thrust at each reaction jet is a function of the duct pressure ratio and the reaction jet opening

$$T_{FP} = T_{FP}(\delta_{FP}, \varepsilon_{RCS}) \qquad (C-7)$$

$$T_{RP} = T_{RP}(\delta_{RP}, \varepsilon_{RCS}) \qquad (C-8)$$

$$T_{LR} = T_{LR}(\delta_{LR}, \varepsilon_{RCS}) \qquad (C-9)$$

$$T_{RR} = T_{RR}(\delta_{RR}, \varepsilon_{RCS}) \qquad (C-10)$$

$$T_{YAW} = T_{YAW}(\delta_{YAW}, \varepsilon_{RCS}) \qquad (C-11)$$

The total reaction control system mass flow can now be calculated

$$\dot{m}_{RCS} = \dot{m}_{RCS}(T_{RCS}, \delta_{N1}) \qquad (C-12)$$

where

$$T_{RCS} = T_{FP} + T_{RP} + \left| T_{LR} \right| + \left| T_{RR} \right| + \left| T_{YAW} \right| \qquad (C-13)$$

The absolute values are necessary for those reaction control jets which are bi-dimentional.

The individual reaction jet force vectors in body axes can now be calculated.

$$\underline{T}_{FP} = \begin{bmatrix} T_{FP} \sin(\theta_{FP}) \\ 0 \\ -T_{FP} \cos(\theta_{FP}) \end{bmatrix} \qquad (C-14)$$

$$\underline{T}_{RP} = \begin{bmatrix} T_{RP} \, \sin(\theta_{RP}) \\ 0 \\ -T_{RP} \, \cos(\theta_{RP}) \end{bmatrix} \qquad \text{(C-15)}$$

where θ_{FP} and θ_{RP} are constants. The actual value of θ_{FP} is negative.

$$\underline{T}_{LR} = \begin{bmatrix} 0 \\ 0 \\ -T_{LR} \end{bmatrix} \qquad \text{(C-16)}$$

$$\underline{T}_{RR} = \begin{bmatrix} 0 \\ 0 \\ -T_{RR} \end{bmatrix} \qquad \text{(C-17)}$$

$$\underline{T}_{YAW} = \begin{bmatrix} 0 \\ T_{YAW} \\ 0 \end{bmatrix} \qquad \text{(C-18)}$$

The main nozzle thrust depends primarily on throttle, reaction control mass flow and forward speed, with $\dot{m}_{RCS}$ causing a decrease in thrust. The effect of nozzle angle on the thrust magnitude is small, since it only affects the rear nozzle splay angle.

$$T_F = T_F(\delta_{N1}, \, \dot{m}_{RCS}, \, M) \qquad \text{(C-19)}$$

$$T_R = T_R(\delta_{N1}, \delta_{\theta j}, \dot{m}_{RCS}, M) \qquad (C\text{-}20)$$

The projection of the thrust magnitude on the body axes is a function of nozzle angle.

$$\underline{T}_F = \begin{bmatrix} T_F \cos(\theta_t) \\ 0 \\ -T_F \sin(\theta_t) \end{bmatrix} \qquad (C\text{-}21)$$

$$\underline{T}_R = \begin{bmatrix} T_R \cos(\theta_t) \\ 0 \\ -T_R \sin(\theta_t) \end{bmatrix} \qquad (C\text{-}22)$$

where, as shown in Fig. C-1

$$\theta_t = 1.5 \text{ deg} + \delta_{\theta j} \qquad (C\text{-}23)$$

The last engine-induced force is ram drag. This force is aligned with the velocity vector and is applied to the vehicle at the engine intakes. It is a function of engine speed and forward velocity.

$$D_{RAM} = D_{RAM}(\delta_{N1}, M) \qquad (C\text{-}24)$$

The projection of this force on body axes depends on the aerodynamic angles

$$\underline{T}_{RAM} = H_W^B(\alpha, \beta) \begin{bmatrix} -D_{RAM} \\ 0 \\ 0 \end{bmatrix} \qquad (C\text{-}25)$$

The total thrust-induced force is the sum of the reaction control forces, the main nozzle forces and the ram drag.

$$\underline{T}_B = \underline{T}_{FP} + \underline{T}_{RP} + \underline{T}_{LR} + \underline{T}_{RR} + \underline{T}_{YAW} + \underline{T}_F + \underline{T}_R + \underline{T}_{RAM} \quad \text{(C-26)}$$

The moment vector applied to the vehicle by each of these forces is the cross product of the location of the point of application of the force and the force vector. Using $\Delta\underline{x}$ to represent the location of the point of application relative to the aircraft cg, and using $\Delta\tilde{x}$ to represent the cross-product equivalent matrix, the thrust moments appear as follows:

$$\underline{G}_B = \Delta\tilde{x}_{FP}\, \underline{T}_{FP} + \Delta\tilde{x}_{RP}\, \underline{T}_{RP} + \Delta\tilde{x}_{LR}\, \underline{T}_{LR}$$

$$+ \Delta\tilde{x}_{RR}\, \underline{T}_{LR} + \Delta\tilde{x}_{YAW}\, \underline{T}_{YAW} + \Delta\tilde{x}_F\, \underline{T}_F$$

$$+ \Delta\tilde{x}_R\, \underline{T}_R + \Delta\tilde{x}_{RAM}\, \underline{T}_{RAM} \quad \text{(C-27)}$$

The aerodynamic forces and moments depend on dynamic pressure (this model is not designed to operate at hover), but are modified by the engine-induced flow field. This flow field is defined by the nozzle angle, $\delta_{\theta j}$, and the jet-to-forward velocity ratio, V_j/V.

$$V_j/V = \sqrt{T/(\tfrac{1}{2}\,\rho V^2\, S_N)} \quad \text{(C-28)}$$

where S_N is the nozzle reference area and T is the total front and rear nozzle thrust.

The aerodynamic forces in body axes are calculated from wind-axis force coefficients as follows

$$\underline{F}_B = \begin{bmatrix} \cos \alpha & 0 & -\sin \alpha \\ 0 & 1 & 0 \\ \sin \alpha & 0 & \cos \alpha \end{bmatrix} \begin{bmatrix} -\frac{1}{2} \rho V^2 & S & C_D \\ \frac{1}{2} \rho V^2 & S & C_Y \\ -\frac{1}{2} \rho V^2 & S & C_L \end{bmatrix}$$ (C-29)

where the coefficients are calculated from tabular values according to the equations

$$C_D = C_{D_o}(\alpha, \delta_S, V_j/V, \delta_{\theta j}) + C_{D_q} \frac{q \bar{c}}{2V}$$ (C-30)

$$C_Y = C_{Y_o}(\beta, \alpha, V_j/V, \delta_{\theta j}) + C_{y_{\delta r}} \delta_r + C_{y_{\delta a}} \delta_a$$

$$+ (C_{y_p} p_S + C_{y_r} r_S) \frac{b}{2V}$$ (C-31)

$$C_L = C_{L_o}(\alpha, \delta_S, V_j/V, \delta_{\theta j}) + (C_{L_{\dot{\alpha}}} \dot{\alpha} + C_{L_q} q) \frac{\bar{c}}{2V}$$ (C-32)

The stability axis roll and yaw rates are found as follows

$$\begin{bmatrix} p_S \\ q_S \\ r_S \end{bmatrix} = \begin{bmatrix} \cos \alpha & 0 & \sin \alpha \\ 0 & 1 & 0 \\ -\sin \alpha & 0 & \cos \alpha \end{bmatrix} \begin{bmatrix} p \\ q \\ r \end{bmatrix}$$ (C-33)

The aerodynamic moments are calculated in a similar manner.

146

$$
\underline{M}_B = \begin{bmatrix} \cos\alpha & 0 & -\sin\alpha \\ 0 & 1 & 0 \\ \sin\alpha & 0 & \cos\alpha \end{bmatrix} \begin{bmatrix} \tfrac{1}{2}\rho V^2 & Sb & C_{l_S} \\ \tfrac{1}{2}\rho V^2 & S\bar{c} & C_m \\ \tfrac{1}{2}\rho V^2 & Sb & C_{n_S} \end{bmatrix} \qquad (C\text{-}34)
$$

where

$$
C_{l_S} = C_{l_o}(\beta,\ \alpha,\ V_j/V,\ \delta_{\theta j}) + C_{l_{\delta r}}(V)\delta_r + C_{l_{\delta a}}\delta_a
$$

$$
+\ (C_{l_p}\, p_S + C_{l_r}(\alpha)r_S)\,\frac{b}{2V} \qquad (C\text{-}35)
$$

$$
C_m = C_{m_o}(\alpha,\ \delta_S,\ V_j/V,\ \delta_{\theta j}) + (C_{m_{\dot\alpha}}\dot\alpha + C_{m_q}q)\,\frac{\bar{c}}{2V}
$$

$$
-\ C_z(\frac{x_{cg}}{\bar{c}} - \frac{x_{yo}}{\bar{c}}) + C_x(\frac{z_{cg}}{\bar{c}} - \frac{z_{yo}}{\bar{c}}) \qquad (C\text{-}36)
$$

where $x_{cg_o} = 0.09\ \bar{c}$, $z_{cg_o} = 0.0\ \bar{c}$

$$
C_{n_S} = C_{n_o}(\beta,\ \alpha,\ V_j/V,\ \delta_{\theta j}) + C_{n_{\delta r}}\delta_r + C_{n_{\delta a}}(\alpha)\delta_a
$$

$$
+\ (C_{n_p}(\alpha)p_S + C_{n_r}r_S)\,\frac{b}{2V} \qquad (C\text{-}37)
$$

For use in the study reported here, the nonlinear equations described above are used to calculate vehicle trim conditions. Static trim is straightforward, since all of the "inner eight" states $(\theta,u,q,w,v,r,p,\phi)$ are constant. Quasi-static trim involves a force and moment balance which produces locally-constant earth-relative acceleration. Specifically,

quasi-static trim involves constant $\dot{V}$, α, β, p, q, and r in this application. About each of these trim conditions, a linearized aircraft model is found by taking into account all interactions between states and controls. Analysis of this linear system provides the handling quality data presented in Chapter 2. These linear systems also provide the basis for flight control design presented in Chapter 3.

C.2   GROUND EFFECTS MODEL

The ground effects included in this study are due to suck down (loss of lift as altitude decreases) and fountain flow effects on roll and pitch moments.

Reference 6 discusses a 6 per cent lift loss during a decent from 20 ft altitude to zero. Assuming the thrust at 20 ft is about equal to weight and the suck down is linear between zero and 20 ft produces the following

$$\frac{\partial Z}{\partial h} = \frac{0.06 \cdot mg}{20 \text{ ft}} = 40 \text{ lb}_f/\text{ft} \qquad (C\text{-}38)$$

$$= 580 \text{ N/m}$$

Reference 17 includes a thorough analysis of the effects of the ground on pitch and roll moments for the VAK-191B. Since the configurations of the VAK-191B and the AV-8A differ significantly, the following adjustments were made to Ref. 17 data for use with the AV-8A. The AV-8A has four splayed nozzles on its lift-cruise engine, while the VAK-191B has four nozzles on its lift-cruise engine and two vertical lift engines. The lift-cruise nozzles of the VAK-191B do not appear to be as widely splayed as those of the Harrier. All of this leads to the subjective judgement that roll

148

instability will not be as severe for the AV-8A as it is for the VAK-191B. However, the Harrier roll inertia is 1.37 times the VAK-191B roll inertia. Hence, the same value of L_ϕ measured for the VAK-191B (450 ft-lb$_f$/deg) is used for the Harrier, and the larger roll inertia of the AV-8A will reduce its dynamic effect.

The stabilizing pitch stiffness and damping terms observed for the VAK-191B are probably due to the long moment arm of the lift engines. It was judged advisable to reduce the VAK-191B values by 50 per cent for use with the AV-8A. This produces a pitch stiffness (M_θ) due to ground effect of -125 ft-lb$_f$/deg and a pitch damping (M_q) of -250 ft-lb$_f$/(deg/sec). Note that since the pitch inertia of the Harrier is about 50% smaller than that of the VAK-191B, the actual dynamic effects on the two aircraft will be similar. Table C-3 summarizes the aerodynamic changes due to ground effect, as modeled in this study.

TABLE C-3

GROUND EFFECT INCREMENTS

T-3070

Z_h	40 lb$_f$/ft	580 N/m
M_θ	-125 ft-lb$_f$/deg	-170 N · m/deg
$M_{\dot\theta}$	-250 ft-lb$_f$/(deg/sec)	-340 N · m/(deg/s)
L_ϕ	450 ft-lb$_f$/deg	+610 N · m/deg

C.3   AV-8A CONTROL SYSTEM DESCRIPTION

The AV-8A control system consists of the pilot controls, the control linkage, the main actuators, the control surfaces, the propulsion system, the reaction control system (rcs), and the stability augmentation system. Except for the last, these constituents of the control system are discussed in the following paragraphs.

The Pilot Controls - The pilot controls are the lateral and longitudinal stick, the rudder pedals, the throttle and the nozzle angle lever.

The lateral stick controls the ailerons and roll rcs jets, as well as rudder through an aileron-to-rudder interconnect. Lateral stick deflection limits are -4.0 in to + 4.0 in, with positive stick giving positive aileron. For the AV-8A, positive aileron produces positive roll moments. The lateral stick-to-aileron gearing is shown in Fig. C-2.

R-42090
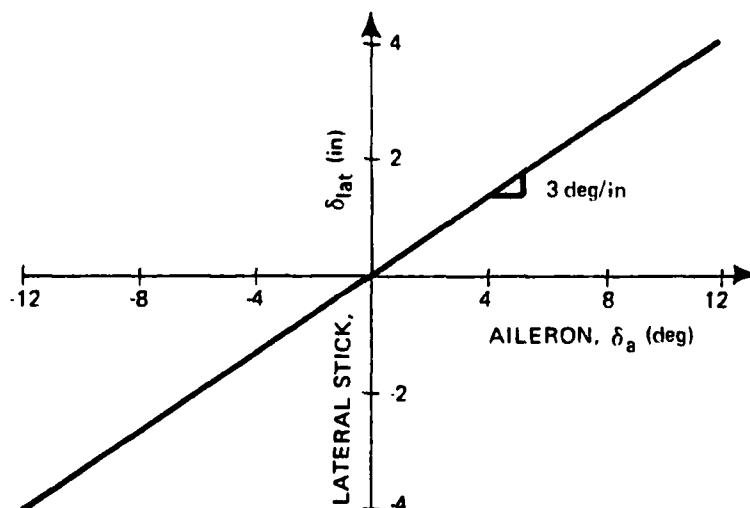
Figure C-2   Lateral Stick-to-Aileron Gearing

The longitudinal stick controls the stabilator and
the pitch rcs jets. Longitudinal stick deflection limits are
+3.7 in to -7.5 in, with positive stick giving positive sta-
bilator. For the AV-8A, positive stabilator produces negative
(nose down) pitch. The longitudinal stick to stabilator gear-
ing is shown in Fig. C-3.

R-42091
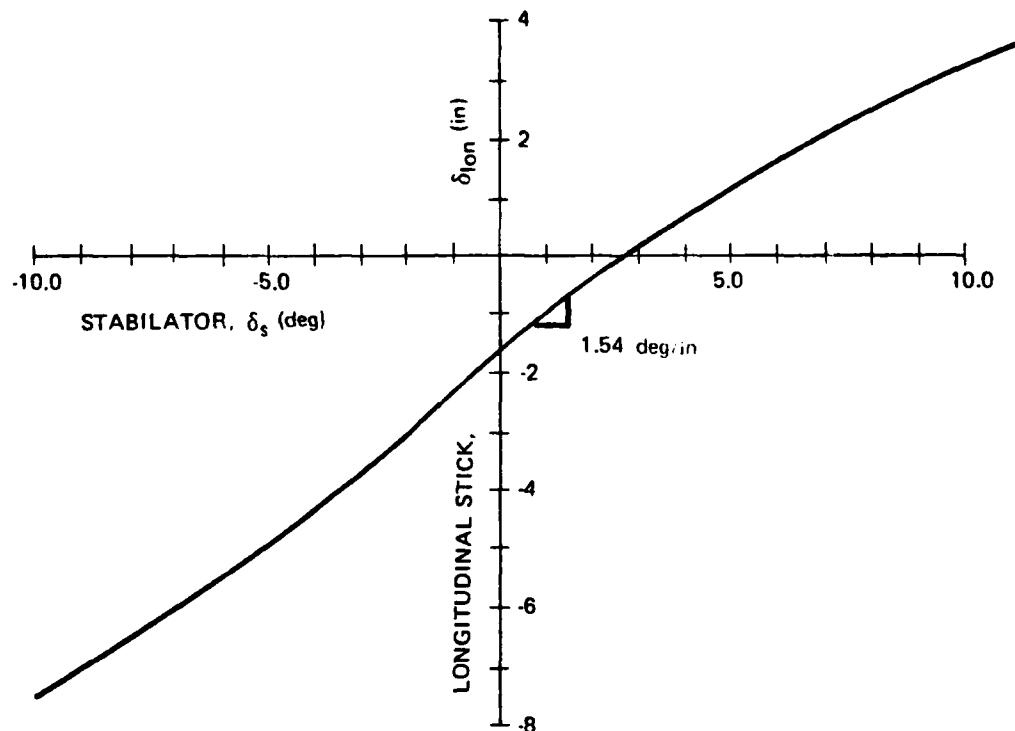
Figure C-3   Longitudinal Stick-to-Stabilator Gearing

The rudder pedals control the rudder deflection and
the yaw rcs jets, with pedal limits of ±2.1 in. Positive
pedal deflection corresponds to positive rudder deflection
(which produces nose left yaw and right wing down roll.
Rudder pedal to rudder gearing is shown in Fig. C-4.

151
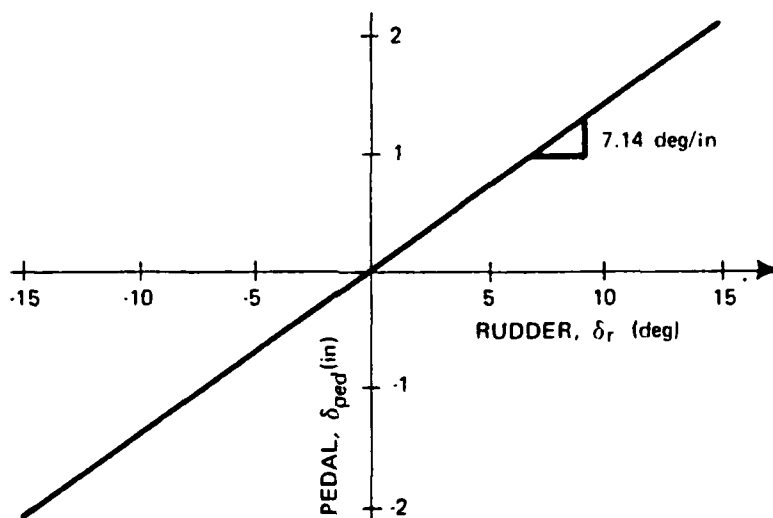
Figure C-4   Rudder Pedal-to-Rudder Gearing

The throttle controls engine thrust level, and is
calibrated directly in percent of fan rpm at normal rated
thrust. In the actual aircraft the idle limit is somewhat
above 0%, while the absolute limit is 105%. There are further
limits (not modeled in this work) of 102% if water injection
is off or nozzle angle is less than 10 deg. There are also
temperature limits which restrict the time that can be spent
above 102%.

The nozzle angle control (physically located next to
the throttle) is calibrated in degrees of nozzle angle. The
limits are zero degrees (nozzles fully rearward) and 98.5 deg,
(nozzles fully down and somewhat forward). These angles are
measured relative to a line which is 1.5 deg down from the
body x-axis. Hence, even at zero nozzle angle, there is some
upward body z-axis force due to thrust.

The Control System Linkage and Main Actuators - The
aileron main actuator is driven by the aileron command from
lateral stick and by the roll sas command. The aileron com-
mand from lateral stick is limited to ±12 deg, while the roll
sas limit is ±2 deg. The main actuator is essentially a first
order lag with a time constant of 0.04 sec (1/25 sec). No
rate limit is given.

The stabilator main actuator is driven by the stabi-
lator command from longitudinal stick (limited to -10 to +11.3
deg) and by the pitch sas command (±1.5 deg limit). The main
actuator time constant is 0.0833 sec (1/12 sec). No rate
limit is given.

The rudder has no actuator, and is driven by rudder
command from rudder pedals (±15 deg) and by a mechanical
aileron-rudder interconnect (0.58 deg rudder/deg aileron)
driven by lateral stick. There is a discrepancy in Ref. 6
between the AV-8A computer simulation and the rudder control
system description; the above description corresponds to the
AV-8A computer simulation.

The engine is modeled as a first-order system with
time constant and rate limits which depend on engine rpm. The
time constant is plotted in Fig. C-5, while the limit on posi-
tive rpm rate is shown in Fig. C-6. There is no limit on
negative rpm rate.

The nozzle angle drive is a constant rate drive that
operates at 150 deg/sec. The front nozzle splay angle is con-
stant at 5.13 deg, while the rear nozzle splay angle varies
with θ_j as shown in Fig. C-7.

R-42093
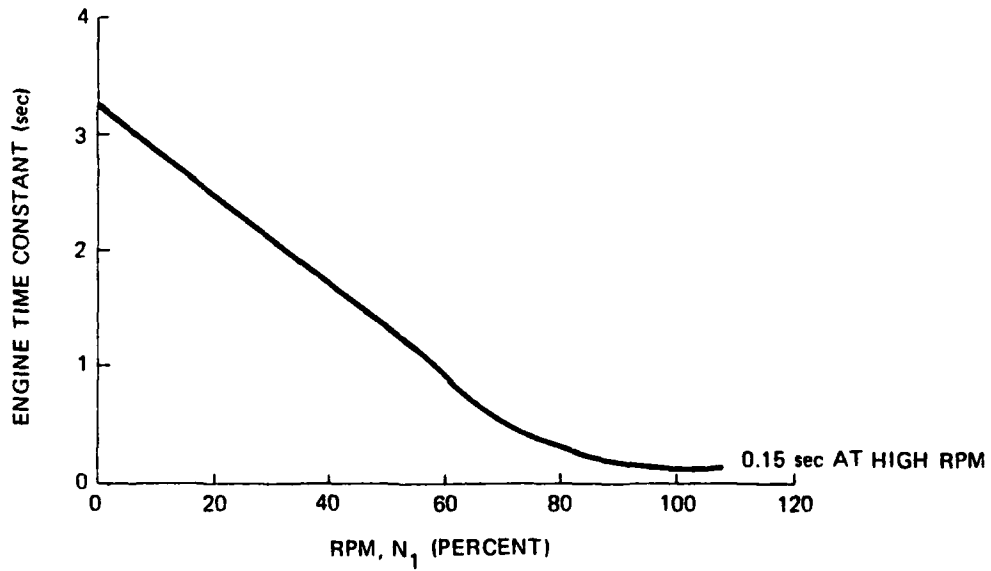
Figure C-5   Engine Time Constant as a Function of RPM

R-42094
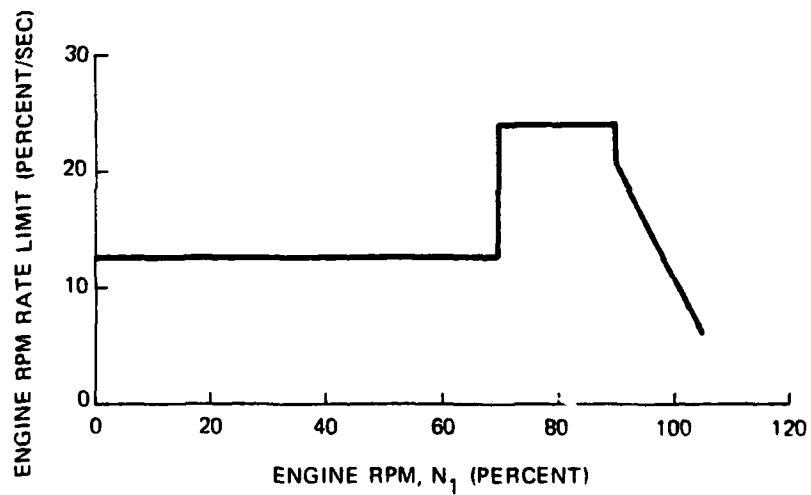
Figure C-6   Engine Rate Limit as a Function of RPM

154
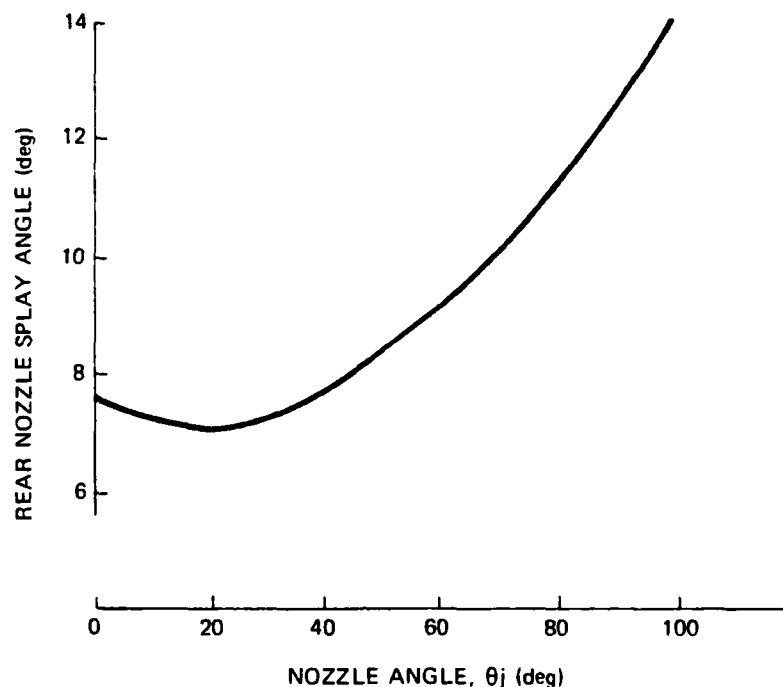
Figure C-7   Rear Nozzle Splay Angle as a Function
             of Nozzle Angle

The Reaction Control System - Jet Effectiveness - The
reaction control system (rcs) consists of front and rear pitch
jets, left and right roll jets and a rear mounted yaw jet.
The locations of these jets are shown in Fig. C-1. Note that
the pitch jets only thrust upwards, while the roll jets exhaust
both up and down. The yaw jets are also bi-directional. The
jets are supplied with air bled from the fan plenum; this bleed
decreases the available thrust from the engine nozzles. The
bleed air connection is fully closed at a nozzle angle of 0
deg, and gradually opens as θ_j increases to 20 deg, as shown
in Fig. C-8. The maximum thrust from each nozzle at 100% N_1
and no duct pressure loss is given in Table C-4, along with
the body axis moments that these thrust values produce.

155
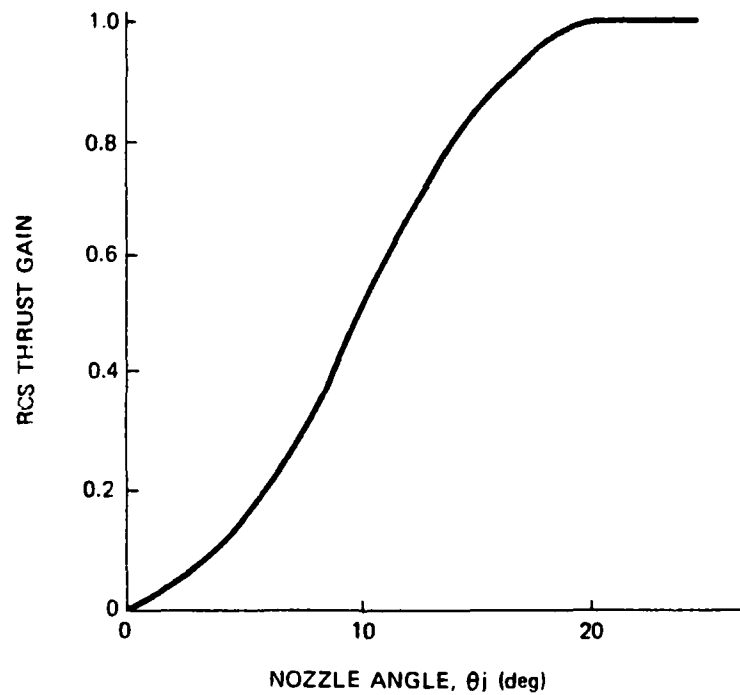
Figure C-8   RCS Thrust Gain at Low Nozzle Angles

TABLE C-4

RCS THRUSTER POWER

T-3071

THRUSTER JET	NOMINAL THRUST	MOMENT
Front Pitch Jet	4230 N 950 lb$_f$	21,960 N · m 16,198 lb$_f$-ft pitch
Rear Pitch Jet	4890 N 1100 lb$_f$	-32,740 N · m -24,145 lb$_f$-ft pitch
Yaw Jet	2890 N 650 lb$_f$	-18,850 N · m -13,904 lb$_f$-ft yaw -1,730 N · m -1,310 lb$_f$-ft roll
Roll Jet (Up Thrust)	2720 N 612 lb$_f$	9,190 N · m 6,781 lb$_f$-ft roll -5,320 N · m -3,926 lb$_f$-ft pitch
Roll Jet (Down Thrust)	1060 N 238 lb$_f$	3,570 N · m 2,632 lb$_f$-ft roll 2,070 N · m 1,524 lb$_f$-ft pitch

To summarize, the nominal thrust is changed by the plenum pressure ratio (which depends on N_1), by main bleed value position (which depends on θ_j and is fully open for θ_j greater than 20 deg), by duct pressure losses (which depend on the open exhaust area of the thrusters) and each individual thruster exhaust area.

These last thrust-to-area relationships are detailed in Figs. C-9 and C-10.
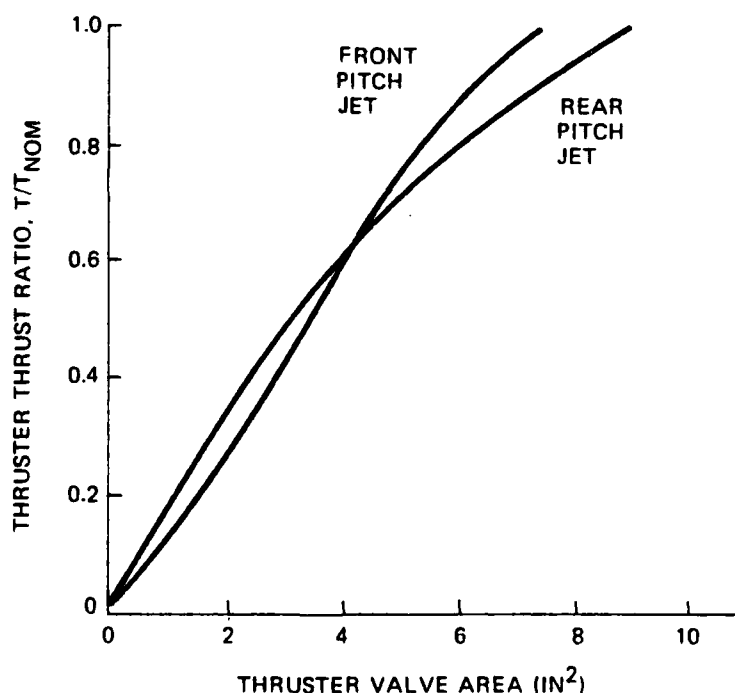
Figure C-9   Pitch Jet Thrust Ratio vs Jet Area

The Reaction Control System - Jet Gearing - The rcs jets are opened and closed by the pilots controls and the stability augmentation system. The front pitch jet is connected
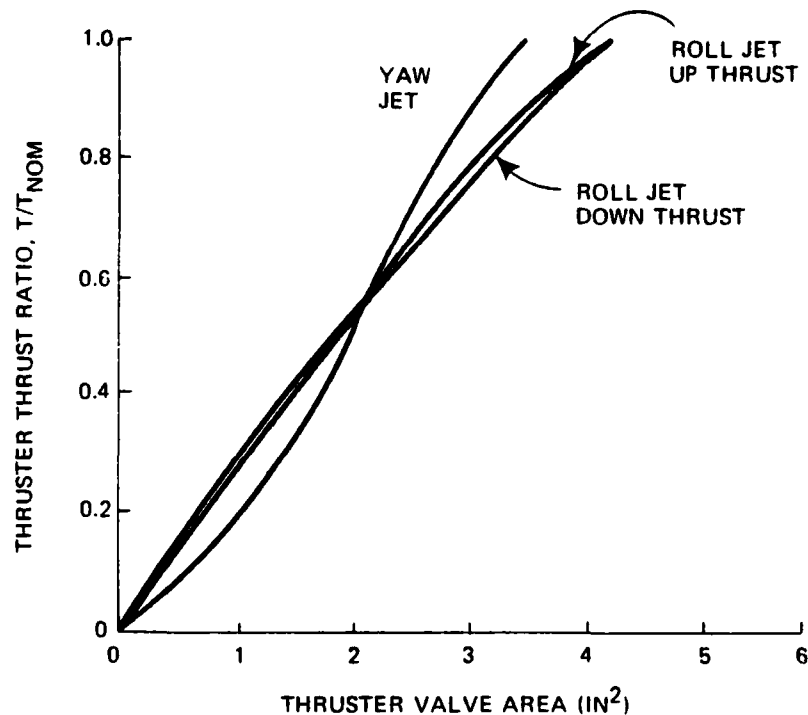
Figure C-10   Roll and Yaw Jet Thrust Ratio vs Jet Area

directly to the longitudinal stick, as described by Fig. C-11.
The rear pitch jet is driven by the actual stabilator deflec-
tion, which itself is a function both of pilot stick and pitch
sas. The rear pitch jet to stabilator gearing is shown in
Fig. C-12.

        The wing-mounted roll jets are connected to their
respective ailerons. Figure C-13 shows the form of this gear-
ing. Note that the ailerons deflect differentially, hence
the net effect is that due to both roll jets. The yaw jets
are driven by both the rudder deflection and the yaw sas out-
put. Interestingly, the yaw sas does not drive rudder at all.
The yaw sas output, expressed in equivalent degrees of rudder,
is limited to ±5 deg. Figure C-14 gives the yaw rcs jet gear-
ing as a function of the rudder and yaw sas commands.

FRONT PITCH JET AREA, δ_{FP} (IN^2)

$-2.125 \dfrac{IN^2 \ JET}{IN \ STICK}$

LONGITUDINAL STICK POSITION, δ_{lon} (IN)
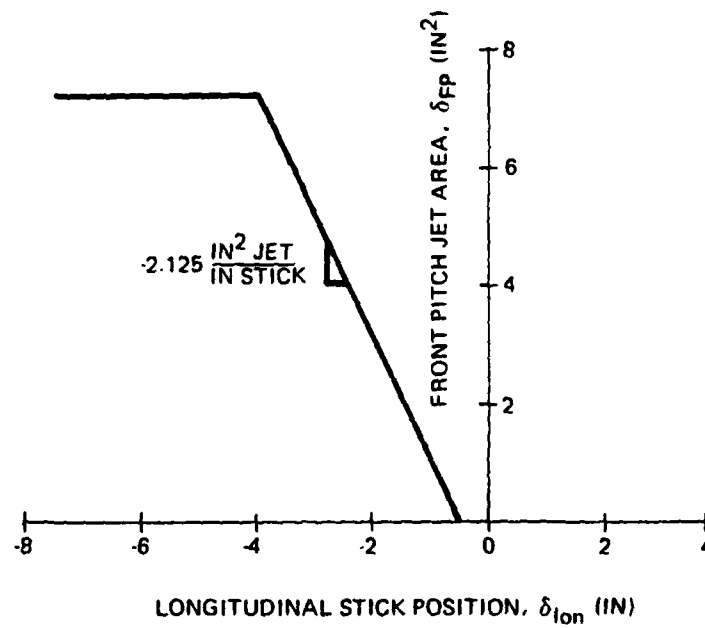
Figure C-11   Front Pitch Jet Gearing

REAR PITCH JET AREA, δ_{RP} (IN^2)

1.09 In^2/deg

STABILATOR POSITION, δ_s (deg)
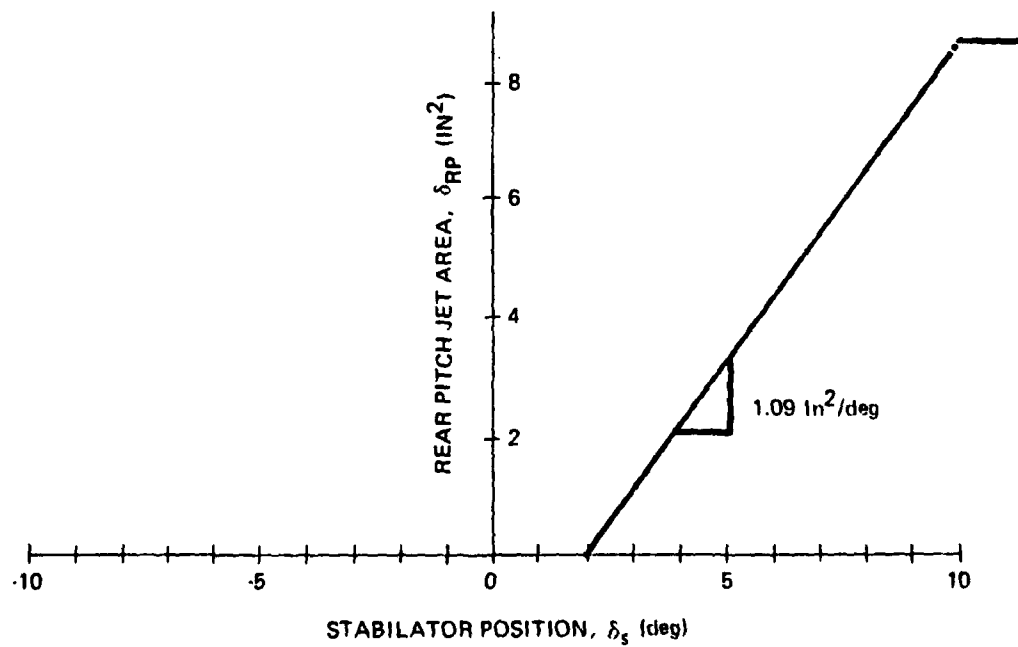
Figure C-12   Rear Pitch Jet Gearing

159
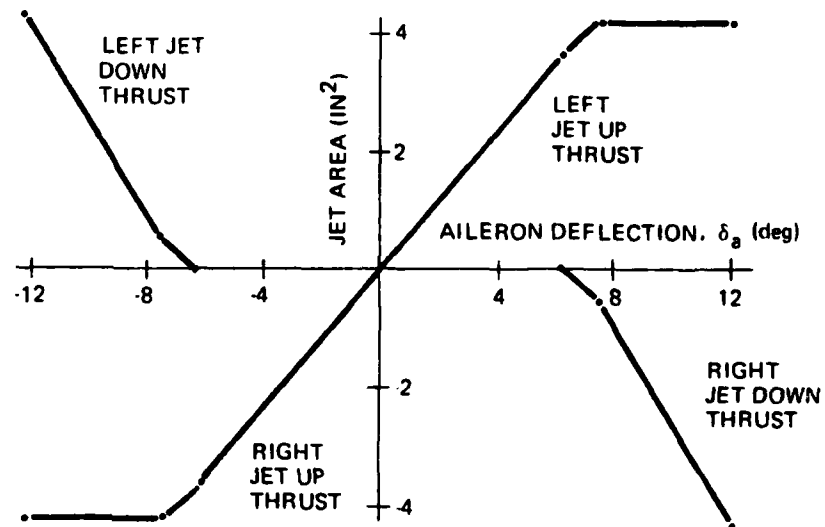
Figure C-13   Roll Jet vs Aileron Gearing
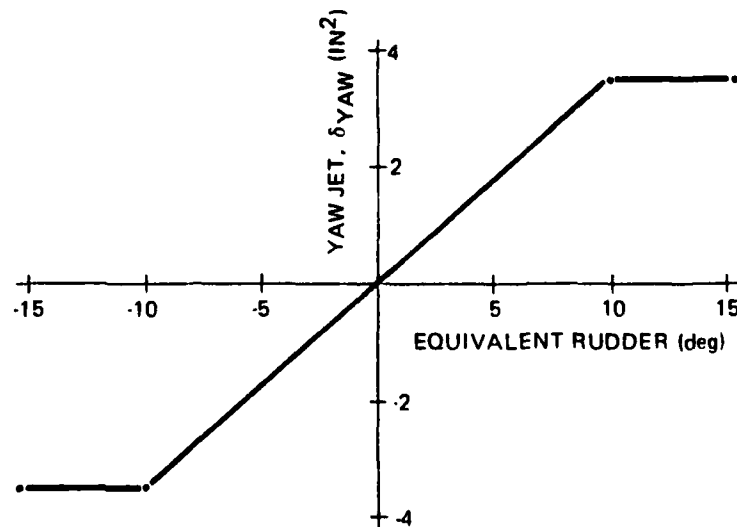
Figure C-14   Yaw Jet vs Equivalent Rudder Gearing

C.4 REACTION JET INTERCONNECTIONS

As listed in Table C-2, the AV-8A model analyzed in this report has ten independent controls. For the purposes of digital flight control system design, however, the number of controls was reduced to eight. This was done by combining front and rear pitch jets and left and right roll jets in much the same way as they are combined in the actual aircraft.

For the pitch jets, a single control variable, δ_{PJ}, is created which directly commands front pitch jet with unity gain when positive. The gearing to the rear pitch jet when δ_{PJ} is negative is chosen so that pitch moment due to δ_{PJ} is linear. From Table C-4, this gain is as follows:

$$K = -0.81 \frac{in^2 \, \delta_{rp}}{in^2 \, \delta_{pj}} \qquad (C-39)$$

The lower limit of δ_{pj} is found from the limit of the rear pitch jet as follows:

$$\delta_{pj,min} = (1/K) \, \delta_{rp,max}$$
$$= -10.78 \, in^2 \qquad (C-40)$$

The roll jet gearing is chosen to be linear from the minimum to the maximum deflection. As one roll jet thrusts upwards, the other thrusts downwards. Note from Fig. C-13 that this is somewhat different from the AV-8A roll jet gearing. The down-thrusting roll jet is much less effective than the up-thrusting one, so the roll moment excited by both jets is only 1.388 times that excited by the up-thrusting jet. Additionally, the vertical forces are not balanced by this gearing. The combined roll jet control is referred to as δ_{rj} in Chapter 3.

161

APPENDIX D
LIST OF SYMBOLS

In general, matrices are represented by capital letters and vectors are underscored; exceptions to these rules are only made when they are contradicted by standard aerodynamic notation.

Variable	Description
A	Discrete time feedforward matrix
a	Acceleration
a_n	Component of the earth-relative acceleration in the aircraft x-z plane normal to the velocity vector
a_y	Component of the earth-relative acceleration normal to the aircraft x-z plane
B	Disturbance observation matrix
b	Wing span
C	State observation matrix Type 1 control law feedback gains
C_{1_2}	Partial derivative of the nondimensional coefficient of force or moment 1 with respect to the nondimensional variable 2 (scalar)
$\bar{c}$	Mean aerodynamic chord
D	Control observation matrix Drag
E	Disturbance input allocation matrix
F	System dynamics matrix
$\underline{F}$	Aerodynamic contact force vector

162

Variable	Description
F_{CL}	Closed-loop aircraft system matrix
$\underline{f}$	Vector-valued nonlinear function
f	Scalar element in system dynamics matrix
G	Control input allocation matrix
g	Magnitude of gravitational acceleration vector
H	Command variable transformation matrix
H_1^2	Euler angle transformation from Frame 1 axes to Frame 2 axes
h	Altitude
I	Identity matrix Moment of inertia
i	Index integer
J	Cost functional matrix
j	$\sqrt{-1}$
K	Type 0 gain matrix
k	Index integer
L	Aerodynamic moment about the x-axis (scalar)
$\ln$	Natural logarithm
ℓ	Number of commands
M	Aerodynamic moment about the y-axis (scalar) Cross weighting matrix between states and controls
m	Mass of the vehicle Number of controls Meters
N	Aerodynamic moment about the z-axis (scalar) Newtons ($kg\ m\ sec^{-2}$)

163

LIST OF SYMBOLS (Continued)

Variable	Description
N_1	Engine speed expressed as a percentage of full speed
n	Number of states
P	Riccati matrix in the optimal regulator problem
p	Rotational rate about the body x-axis
p_W	Stability-axis roll rate
Q	State weighting matrix
q	Rotational rate about the body y-axis
q_∞	Free stream dynamic pressure ($=\frac{1}{2}\rho V_o^2$)
R	Control or control-rate weighting matrix
R^a	A subspace with dimension a
r	Rotational rate about the body z-axis
S	Reference area (usually wing area)
T	State command matrix used in eigenvalue/ eigenvector placement (Diagonalizing matrix) Thrust
t	Time
u	Body x-axis velocity component
$\underline{u}$	Control vector
V	Inertial velocity magnitude
v	Body y-axis velocity component Control difference
w	Body z-axis velocity component
$\underline{w}$	Aircraft disturbance vector
X	Aerodynamic force along the x-axis (scalar)

LIST OF SYMBOLS (Continued)

x	Position along the x-axis
$\underline{x}$	State vector
x_{cg}	Normalized longitudinal distance between actual c.g. location and point used for aerodynamic moment measurements expressed in body axes
Y	Aerodynamic force along the y-axis (scalar)
y	Position along the y-axis
Z	Aerodynamic force along the z-axis (scalar)
z	Position along the z-axis Laplace operator (discrete time)

Variable (Greek)	Description
α	Wind-body pitch Euler angle (angle of attack)
β	Negative of wind-body yaw Euler angle (sideslip angle)
Γ	Discrete time control effect matrix
γ	Inertial-velocity axis pitch Euler angle (flight-path angle)
δ_a	Aileron deflection
δ_{pj}	Pitch jets nozzle area opening
δ_{rj}	Roll jets nozzle area opening
δ_r	Rudder deflection
δ_s	Stabilator deflection
δ_{yj}	Yaw jet area opening
ε	Reaction jet force
ζ	Damping ratio

165

LIST OF SYMBOLS (Continued)

Variable (Greek)	Description
θ	Inertial-body pitch Euler angle
θ_j	Thrust nozzle angle
λ	Eigenvalue
ξ	Inertial-velocity axis yaw Euler angle (heading angle) Eigenvector Integrator state
Π	Matrix in quad partition matrix inverse
ρ	Air density
Σ	Summation
σ	Real part of an eigenvalue in radians/sec
τ	Time constant
Φ	Discrete-time system matrix
ϕ	Inertial-body axis roll Euler angle
χ	Matrix in adjusted quad partition matrix inverse
ψ	Inertial-body axis yaw Euler angle
ω	Frequency in radians/sec Imaginary part of an eigenvalue

Variable (Subscript or Superscript)	Description
A	Eigenvalue/eigenvector placement models
B	Body axes
CL	Closed loop
D	Discrete time

166

LIST OF SYMBOLS (Continued)

Variable (Subscript or Superscript)	Description
DR	Downrange
f	force
I	Inertial axes
ℓ	Aerodynamic moment about the x-axis
m	Aerodynamic moment about the y-axis Model to be followed
N	Nozzle
n	Aerodynamic moment about the z-axis
V	Velocity axes
W	Wind axes (same as stability axes for $\dot{\beta}_0 = \dot{\alpha}_0 = 0$)
w	Disturbance
x	Component along the x-axis
y	Component along the y-axis
z	Component along the z-axis
X	Aerodynamic force along the x-axis
Y	Aerodynamic force along the y-axis
Z	Aerodynamic force along the z-axis

Operator	Definition
$(\dot{})$	Time derivative
$(\tilde{})$	Matrix equivalent to vector cross product. Specifically, if $\underline{x}$ is the three-dimensional vector

Operator   Definition

$$\underline{x} = \begin{bmatrix} x \\ y \\ z \end{bmatrix} \text{, then } \tilde{x} = \begin{bmatrix} 0 & -z & y \\ z & 0 & -x \\ -y & x & 0 \end{bmatrix}$$

and the cross product of $\underline{x}$ and $\underline{f}$ is equal to the product of the matrix $\tilde{x}$ and the vector $\underline{f}$,

$$\underline{x} \times \underline{f} = \tilde{x}\underline{f}$$

Operator	Definition
$(\underline{\tilde{}})$	Difference between a vector and its expected value
$(\ )i$	The ith column of the matrix
$(\ )^T$	Transpose of a vector or matrix
$(\ )^{-1}$	Inverse of a matrix
$(\ )_0$	Reference or nominal value of a variable
$\Delta(\ )$	Perturbation about the nominal value of a variable
$(\ )_{max}$	Maximum value, usually due to displacement limit of an actuator

Acronym	Corresponding Phrase
AV-8A	Harrier jet vertical or short take-off and landing aircraft in operation
AV-8B (YAV-8B)	Harrier jet vertical or short take-off and landing aircraft in development
CCV	Control configured vehicle
cg	Center of gravity
CGT-PI	Command generator tracker-proportional integral controller
DFCS	Digital flight control system

LIST OF SYMBOLS (Continued)

Acronym	Corresponding Phrase
EEP	Eigenvalue/eigenvector placement
IGE	In ground effect
kt	Knots
RPM	Revolutions per minute
rcs	Reaction control system
V/STOL	Vertical or short take-off and landing aircraft
VAK-191B	Jet vertical or short take-off and landing aircraft
X-22A	Fixed-wing variable fan vertical or short take-off and landing aircraft

REFERENCES

1. "Harrier In-Flight Thrust Vectoring Honed," _Aviation Week and Space Technology_, June 10, 1974, pp. 32-35.

2. "Broader Vectored Thrust Uses Sought," _Aviation Week and Space Technology_, June 17, 1974, pp. 39-43.

3. Ringland, R.F., and Craig, S.J., "Survey of Piloting Factors in V/STOL Aircraft With Implications For Flight Control System Design," _Proceedings of the Navy/NASA V/STOL Flying Qualities Symposium_, Naval Postgraduate School, Monterey, California, April 1977.

4. Stengel, R.F., Taylor, J.H., Broussard, J.R., and Berry, P.W., "High Angle-of-Attack Stability and Control," ONR-CR-215-237-1, April 1976.

5. Stengel, R.F., Broussard, J.R., Berry, P.W., and Taylor, J.H., "Modern Methods of Aircraft Stability and Control Analysis," ONR-CR-215-237-2, May 1977.

6. Nave, R.L., "A Computerized V/STOL - Small Platform Landing Dynamics Integration Model," Naval Air Development Center, Report No. NADC-77024-30, undated.

7. Rossetti, A.M., and Iles, J.E., "Shipboard Testing of the AV-8A "Harrier", _Proceedings of the Navy/NASA V/STOL Flying Qualities Symposium_, Naval Postgraduate School, Monterey, California, April 1977.

8. Lacey, R.T., "MIL-F-83300; View From an Aircraft Designer," _Proceedings of the Navy/NASA V/STOL Flying Qualities Symposium_, Naval Postgraduate School, Monterey, California, April 1977.

9. Fozard, J., "Wind, Seapower and Jet V/STOL," _U.S. Naval Institute Proceedings_, September 1977.

10. Broussard, J.R., "Command Generator Tracking," The Analytic Sciences Corporation (TASC), Report No. TIM-612-1, March 1978.

11. Broussard, J.R., "Command Generator Tracking - The Discrete Time Case," The Analytic Sciences Corporation (TASC), Report No. TIM-612-3, June 1978.

REFERENCES (Continued)

12.   O'Brien, M.J., and Broussard, J.R.," Feedforward Control
      to Track the Output of a Forced Model" 17th IEEE Con-
      ference on Decision and Control, San Diego, California,
      January 1979.

13.   Broussard, J.R., Berry, P.W., and Gully, S.W., "Synthesis
      of Digital Controllers for a Fighter Aircraft Using
      Continuous-Time Specifications," Proceedings of the Con-
      trol Systems Criteria Symposium, Naval Postgraduate
      School, Monterey, California, July 1978.

14.   Berry, P.W., and Broussard, J.R., "Verification of
      Fighter Aircraft Command Augmentation Control Laws by
      Nonlinear Simulation," AIAA Flight Mechanics Conference,
      San Francisco, California, August 1978.

15.   Anon., "Flying Qualities of Piloted V/STOL Aircraft,"
      MIL-F-83300, USAF/USN, December 1970.

16.   Anon., "YAV-8B, Primary and Auxiliary Flight Control
      System Analysis," McDonnell-Douglas Corporation,
      Report MDC-A5316, 25 April 1978.

17.   Fortenbaugh, R.L., "Analysis of the Influence of the
      OGE/IGE Transition on VAK-191B Flying Qualities in
      Hover," Paper No. 10, Proceedings of the Navy/NASA
      V/STOL Flying Qualities Symposium, Naval Postgraduate
      School, Monterey, California, April 1977.

18.   Stein, G., Hartmann, G.L., and Hendrick, R.C.,
      "Adaptive Control Laws for F-8 Flight Test" IEEE
      Transactions on Automatic Control, Vol. AC-22, No. 5,
      October 1977, pp. 758-768.

19.   Athans, M., et al, "The Stochastic Control of the F-8C
      Aircraft Using a Multiple Model Adaptive Control (MMAC)
      Method-Part I: Equilibrium Flight," IEEE Transactions
      on Automatic Control, Vol. AC-22, No. 5, October 1977,
      pp. 768-779.

20.   Alag, G., and Haufman, H., "An Implementable Digital
      Adaptive Flight Controller Designed Using Stabilized
      Single-Stage Algorithms," IEEE Transactions on Automatic
      Control, Vol. AC-22, No. 5, October 1977, pp. 780-787.

21.   Stengel, R.F., Broussard, J.R., and Berry, P.W.,
      "Digital Flight Control Design for a Tandem-Rotor
      Helicopter," Automatica, Vol. 14, No. 4, July 1978,
      pp. 301-312.

REFERENCES (Continued)

22.   Gerdes, R.M., "A Piloted Simulation of VTOL Landings
        Aboard a Non-Aviation Ship," Proceedings of the Navy/
        NASA V/STOL Flying Qualities Symposium, Naval Post-
        graduate School, Monterey, California, April 1977.

23.   Merkel, P.A., and Whitmayer, R.A., "Development and
        Evaluation of Precision Control Modes for Fighter
        Aircraft," Proceedings of the AIAA Guidance and
        Control Conference, San Diego, California, 1976.

24.   Erzberger, H., "On the Use of Algebraic Methods in
        the Analysis and Design of Model-Following Control
        Systems," NASA TN D-4663, Ames Research Center,
        July 1968.

25.   Tyler, J.S., Jr., "The Characteristics of Model Follow-
        ing Systems as Synthesized by Optimal Control," IEEE
        Transactions on Automatic Control, Vol. AC-9, No. 4,
        October 1964, pp. 485-498.

26.   Broussard, J.R., Berry, P.W., and Stengel, R.F.,
        "Modern Digital Flight Control System Design for VTOL
        Aircraft," The Analytic Sciences Corporation (TASC),
        TR-804-1, November 1977.

27.   Dorato, P., and Levis, A.H., "Optimal Linear Regulators:
        The Discrete-Time Case," IEEE Transactions on Automatic
        Control, Vol. AC-16, No. 6, December 1971, pp. 613-620.

28.   Davison, E.J., "The Output Control of Linear Time-
        Invariant Multivariable Systems With Unmeasurable
        Arbitrary Disturbances," IEEE Transactions Automatic
        Control, Vol. AC-17, pp. 621-629, 1972.

29.   Lebacqz, J.V., and Aiken, E.W., "A Flight Investigation
        of Control, Display, and Guidance Requirements for De-
        celerating Descending VTOL Instrument Transitions Using
        the X-22A Variable Stability Aircraft," Vols. I and II,
        Calspan Report No. AK-5336-F-1, September 1975.

30.   Franklin, J.A., "VTOL Flight Control For All-Weather
        Shipboard Operations", Proceedings of the Navy/NASA
        V/STOL Flying Qualities Symposium, Naval Postgraduate
        School, Monterey, California, April 1977.

31.   Chan, Y.T., "Perfect Model Following With a Real Model,"
        Proceedings of 1973 Joint Automatic Control Conference,
        Columbus, Ohio, pp. 287-293.

REFERENCES (Continued)

32. Kreindler, E., and Rothschild, "Model-Following in Linear-Quadratic Optimization," *AIAA Journal*, Vol. 14, No. 7, July 1976, pp. 835-842.

33. Gran, R., Berman, H., and Rossi, M., "Optimal Digital Flight Control for Advanced Fighter Aircraft," *Journal of Aircraft*, Vol. 14, No. 1, January 1977, pp. 32-37.

34. Doyle, J.C., "Guaranteed Margins for LQG Regulators," *IEEE Transactions on Automatic Control*, Vol. AC-23, No. 4, August 1978, pp. 756-757.

35. Keskar, D.A., and Slater, G.L., "Load Factor Response of Digitally Controlled Aircraft," *AIAA 1977 Guidance and Control Conference*, Paper No. 77-1080, August 1977.

36. Konsewicz, R.K., "Rationale for Selection of a Flight Control System for Lift Cruise Fan V/STOL Aircraft," *Proceedings of the Navy/NASA V/STOL Flying Qualities Symposium*, Naval Postgraduate School, Monterey, California, April 1977.

37. Stengel, R.F., Broussard, J.R., and Berry, P.W., "Command Augmentation Control Laws for Maneuvering Aircraft," *Proceedings of the AIAA Guidance and Control Conference*, Paper No. 77-1044, Hollywood, Florida, August 1977.

38. Kwatny, H.G., McDonald, J.P., and Kalnitsky, K.C., "A Class of Multivariable Controllers and its Application to Power Plant and Power System Control," *Proceedings of the 3rd IFAC Symposium on Multivariable Technological Systems*, 1974.

39. MacFarlane, A.G.J., "Relationships Between Recent Developments in Linear Control Theory and Classical Design Techniques," *Control System Design by Pole-Zero Assignment* (Edited by F. Fallside), Academic Press, London, 1977.

40. Davison, E.J., and Wang, S.H., "Properties and Calculation of Transmission Zeroes of Linear Multivariable Systems," *Automatica*, Vol. 10, No. 6, 1974, pp. 643-658.

41. Laub, A.J., and Moore, B.C., "Calculation of Transmission Zeroes Using QZ Techniques," *Proceedings of the 1977 IEEE Conference on Decision and Control*, Louisiana, December 7-9, 1977, pp. 789-794.

REFERENCES (Continued)

42. Ben-Israel, A., and Greville, T.N.E., <u>Generalized Inverses: Theory and Applications</u>, Wiley-Interscience, 1974.

43. Smith, W.W., and Erdman, S., "A Note on the Inversion of Complex Matrices," <u>IEEE Transactions on Automatic Control</u>, February 1974.

44. Barraud, A.Y., "A Numerical Algorithm to Solve $A^T XA - X = Q$," IEEE <u>Transactions Automatic Control</u>, Vol. AC-22, No. 3, October 1977, pp. 883 to 885.

45. Trankel, T.L., and Bryson, A.E., "Control Logic to Track The Outputs of a Command Generator or Randomly Forced Target," <u>AIAA Guidance and Control Conference</u>, Hollywood, Florida, Paper No. 77-1041, August 1977.

46. Davison, E.J., "The Robust Control of a Servomechanism Problem for Linear Time-Invariant Multivariable Systems," <u>IEEE Transactions on Automatic Control</u>, Vol. AC-21, No. 1, February 1976, pp. 25 to 44.

47. Kwatny, H.G., and Kalnitsky, K.C., "On Alternative Methodologies for the Design of Robust Linear Multivariable Regulators," <u>IEEE Transactions Automatic Control</u>, Vol. AC-23, No. 5, October 1978.

48. Moore, B.C., "On the Flexibility Offered by State Feedback in Multivariable Systems Beyond Closed-Loop Eigenvalue Assignment," <u>IEEE Transactions on Automatic Control</u>, Vol. AC-21, No. 5, October 1976, pp. 689-692.

DISTRIBUTION LIST

Office of Naval Research
800 N. Quincy St.
Arlington, VA   22217
  R. von Husen, Code 211   4
  S. L. Brodsky, Code 432   1

Office of Naval Research
Eastern/Central Regional Office
495 Summer St.
Boston, MA   02210   1

Office of Naval Research
Western Regional Office
1030 E. Green St.
Pasadena, CA   91106   1

Naval Research Laboratory
Washington, DC   20375
  Code 2627   3

Naval Air Systems Command
Washington, DC   20361
  D. Kirkpatrick, AIR 320D   1
  R. C. A'Harrah, AIR 53011   1

Naval Air Development Center
Warminster, PA   19874
  C. J. Mazza, Code 6053   1
  C. R. Abrams, Code 6072   1

Naval Material Command
Washington, DC   20360
  Code 08T23   1

Naval Weapons Center
China Lake, CA   93555
  B. Hardy, Code 3914   1

Naval Surface Weapons Center
Silver Spring, MD   20910
  J. Wingate, Code R44   1

Naval Air Test Center
Patuxent River, MD   20670
  J. McCue, Code TPS   1

David Taylor Naval Ship R&D Center
Bethesda, MD   20084
  Technical Library   1

Naval Post Graduate School
Monterey, CA   93940
  Technical Reports Library   1
  L. Schmidt   1

Defense Technical Information Center
Building 5
Cameron Station
Alexandria, VA   22314   12

Air Force Office of Scientific Research
Building 410
Bolling Air Force Base
Washington, DC   20332
  G. W. McKemie   1

Air Force Flight Dynamics Laboratory
Wright-Patterson Air Force Base
Dayton, OH   45433
  R. Anderson, Control Dyn. Br.   1
  F. George, Control Dyn. Br.   1

Air Force Institute of Technology
Wright-Patterson Air Force Base
Dayton, OH   45433
  P. Maybeck   1

Army Armament R&D Command
Building #18
Dover, NJ   07801
  N. Coleman, DRDAR-SCFCC   1

NASA Langley Research Center
Hampton, VA   23665
  Technical Library   1

NASA Dryden Research Center
P. O. Box 273
Edwards, CA   93523
  Technical Library   1

National Transportation Safety Board
Bureau of Technology
Laboratory Services Division
800 Independence Ave., SW
Washington, DC   20594
  R. von Husen   1

Systems Technology, Inc.
13766 South Hawthorne Blvd.
Hawthorne, CA   90250
  R. Whitbeck   1

Massachusetts Institute of Technology
Lab. for Information and Decision
 Systems
Cambridge, MA   02139
  M. Athans   1

University of Michigan
Dept. of Naval Architecture & Marine
 Engr.
Ann Arbor, MI   48109
  M. G. Parsons   1

Nielsen Engineering & Research, Inc.
510 Clyde Avenue
Mountain View, CA   94043
  J. N. Nielsen   1

University of Notre Dame
Dept. of Electrical Engineering
Notre Dame, IN   46556
  M. K. Sain   1

The C. S. Draper Laboratory, Inc.
555 Technology Square
Cambridge, MA   02139
  R. V. Ramnath   1

Honeywell, Inc.
Systems and Research Center
2600 Ridgway Parkway
Minneapolis, MN   55413
  C. A. Harvey   1

Alphatech, Inc.
3 New England Executive Park
Burlington, MA   01803
  N. R. Sandell   1

Scientific Systems, Inc.
Suite No. 309-310
186 Alewife Brook Parkway
Cambridge, MA   02138
  R. K. Mehra   1

Calspan Corp.
P. O. Box 400
Buffalo, NY   14225
  E. G. Rynaski
  K. S. Govindaraj   1

Systems Control Inc.
1801 Page Mill Road
Palo Alto, CA   94306
  E. Hall

Flight Research Laboratory
Dept. of Mechanical & Aerospace
 Engineering
Princeton University
Princeton, NJ   08544
  R. F. Stengel

ATE MED